INFORMATION TO USERS

This manuscript has been reproduced from the microfilm master. UMI films the text directly from the original or copy submitted. Thus, some thesis and dissertation copies are in typewriter face, while others may be from any type of computer printer.

The quality of this reproduction is dependent upon the quality of the copy submitted. Broken or indistinct print, colored or poor quality illustrations and photographs, print bleedthrough, substandard margins, and improper alignment can adversely affect reproduction.

In the unlikely event that the author did not send UMI a complete manuscript and there are missing pages, these will be noted. Also, if unauthorized copyright material had to be removed, a note will indicate the deletion.

Oversize materials (e.g., maps, drawings, charts) are reproduced by sectioning the original, beginning at the upper left-hand corner and continuing from left to right in equal sections with small overlaps.

Photographs included in the original manuscript have been reproduced xerographically in this copy. Higher quality 6" x 9" black and white photographic prints are available for any photographs or illustrations appearing in this copy for an additional charge. Contact UMI directly to order.

UMI®

Effect of Temperature and Microstructure on

Tensile and Tensile Creep Properties of Ti$_3$SiC$_2$ in Air

A Thesis

Submitted to the Faculty

of

Drexel University

by

Miladin Radovic

In partial fulfillment of the

requirements for the degree

of

Doctor of Philosophy

June 2001

Copyright 2001 by
Radovic, Miladin

All rights reserved.
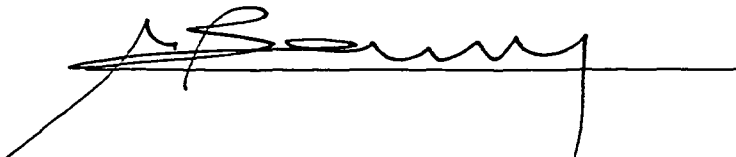
UMI®

Thesis Approval Form

This thesis, entitled __Effect of Temperature and Microstructure on Tensile and Tensile Creep__

__Properties of Ti3SiC2 in Air__
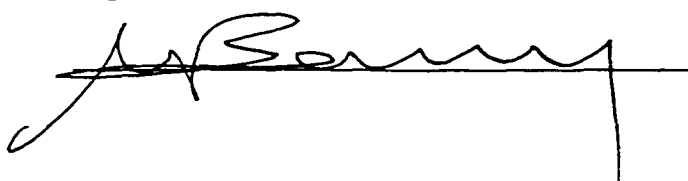
_____, and authored

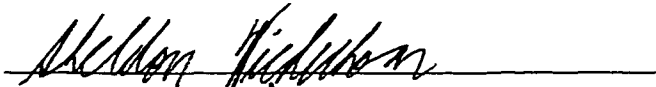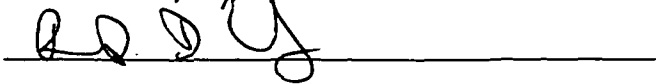by_____Miladin Radovic_____, is hereby accepted and approved.
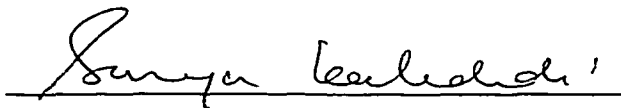
Signatures:
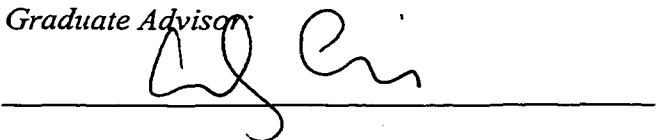
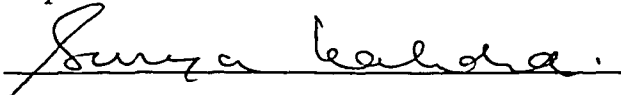Chairman, Examining Committee:

Supervising Professor:

Committee Members:

EDGAR LARA-CURZIO

Graduate Advisor:

Department Head:

Dedication

To my Father who always believed that I could achieve everything I wished for.

You will be always with me.

Acknowledgments

I consider myself lucky and honored for having an opportunity to collaborate with a lot of wonderful people during my work on PhD Thesis. Among all of them, I would like specially to tanks:

- **Dr. Sheldon W. Wiederorn**, National Institute for Standards and Technology, Gaithersburg, MD, for helping me in experimental work, inspiriting discussions and suggestions and for his time and interest in reviewing this thesis and participating in my defense committee;

- **Dr. William E. Luecke**, **Mr. Ralph Kraus Jr** and **Dr. Frantisek Lofaj**, National Institute for Standards and Technology, for unselfish help during my experimental work and precious suggestions;

- **Dr. Tamer El-Raghy**, Drexel University, for his help in specimen' preparation, analyzes of experimental results, valuable discussions and suggestions;

- **Dr. Roger Doherty** and **Dr. Surya Kalidindi**, Drexel University, for helping me to interpretate experimental results, inspiriting discussions, great suggestions and for their time and interest in reviewing this thesis and participating in my defense committee.

- **Dr Edgar Lara-Curzio** from Oak Ridge National laboratory, Oak Ridge, TN for his time and interest in reviewing this thesis and participating in my defense committee;

- **Mr. David Von Rohr** from Drexel University, for his great help with microscopy

- **Mr. Mark Shiber** from Drexel University, for doing the great job in machining the testing samples:

- **Mrs. Judy Trechtman** and **Mrs. Marcie Adams** from Drexel University, for their great help in solving everyday problems, friendly advice and support;

- All **Faculty members of the Materials Engineering Department**, Drexel University, and **all Staff from National Institute of Standards and Technologies**;

- My fellow **graduate students in the Materials Engineering Department** at Drexel University for making this work an enjoyable and unforgettable experience.

It is hard, at this moment, to find appropriate words to express my gratitude to my advisor **Dr. Michel W. Barsoum** for his help, strong support, encouragement, and enthusiasm related to my work, great teaching, friendly advice and his faith in me. Thus, I can simply say: **THANK YOU**.

I would like to thank all professors from University of Belgrade, who taught me. Special thanks are due to my M.S. advisor **Dr. Vera Sijacki-Zeravcic**, University of Belgrade, for introducing me to the wonderful world of Material Science.

Finally, I would like to thank my parents **Milica** and **Nedeljko**, my sister **Gordana**, and my wife **Milica** for their comprehension, help and unselfish support. Without their help, this work would not have been possible.

Philadelphia   Miladin Radovic

May 22, 2001

Table of Contents

List of Tables

List of Figures

Abstract
Effect of Temperature and Microstructure on
Tensile and Tensile Creep Properties of Ti_3SiC_2 in Air
Miladin Radovic
Prof. Michel Barsoum

The ternary carbide, Ti_3SiC_2, combines some of the best attributes of ceramics and metals. It is stable in inert atmospheres to temperatures above 2200 °C, stiff and yet is readily machinable, oxidation, fatigue and thermal shock resistant and damage tolerant. Thus, Ti_3SiC_2 is good candidate material for high temperature structural application. The aim of this work was to characterize its tensile and tensile creep properties.

The mechanical behavior of Ti_3SiC_2 is characterized by a brittle-to-ductile (BTD) transition that is a function of strain rate. Its high strain rate sensitivity (≈ 0.5-0.6) is in the range that is more typical for superplastic materials, although it does not exhibit other attributes of superplasticity. Polycrystalline samples do not exhibit linear elastic behavior in tension even at room temperature. Room temperature loading-unloading tests result in closed hysteresis loops when the stress exceeds ≈ 120 MPa, suggesting that the mechanical response can be described as anelastic (viscoelastic). At high temperatures (1200 °C) intense stress relaxation takes place; cycling loading–unloading tests at high temperature and low strain rates, demonstrate that the samples continue to elongate even during unloading, suggesting that Ti_3SiC_2 deforms viscoplastically.

Tensile creep curves exhibit primary, steady state and tertiary regimes. The minimum creep rate can be represented by power law equation with a stress exponent of 1.5 for fine-grained (3-5 μm) samples, and 2 for coarse-grained (100-300 μm) ones. For both microstructures the activation energy for creep is $\approx$450 kJ/mol. The dependence on grain size is quite weak, implying that diffusion creep and/or creep mechanisms based on grain boundary sliding do not play a central role. Results of strain transient dip tests suggest that large internal stresses are developed during creep. Those internal stresses are believed to result in recoverable (anelastic) strains during unloading. The response on small stress decreases in strain-transient creep tests suggests that the steady state creep is recovery controlled.

Finally, it is important to note that the mechanical response of Ti_3SiC_2 is quite similar to hexagonal ice. Both materials, if loaded rapidly are brittle, but if loaded slowly are quite plastic. This stems from the fact that both are plastically very anisotropic; deformation occurs overwhelmingly by basal slip. In both cases, stress concentrations, and the rate at which they can be relaxed, dictate the nature of the mechanical response.

1. Introduction

Development of the new materials than can be loaded at extremely high temperature has been one of major goals of Materials Science and Engineering over the last century. High fuel-efficiency engines, high efficiency electric power plants, space ships that can stand high temperatures, etc are only some of the more important devices which development is strongly dependent on the development of new high temperature resistance materials. Most metallic materials for high temperature structural applications can be used only up to roughly 1000 °C. Bulling the devices that can work at higher temperatures required another class of materials, namely ceramics. Although there has been great progress in developing temperature resistant structural ceramics over the past 30 years, high brittleness and pure machinability of ceramics limited their wide application. Thus, the need for new high temperature materials that can be easy machinable, tough and highly reliable is still of current interest.

Since Ti_3SiC_2 was for the firs time successfully synthesized as a fully dense, single phase bulk material in 1995 by Dr. M. W. Barsoum and Dr. T. El-Raghy, intensive research on characterization of its properties has been performed. The results shows that Ti_3SiC_2 exhibits good thermal conductivity, structural stability up to 2200 °C in inert atmosphere, high fracture toughness, good damage tolerance and shock resistance, god oxidation properties, etc. All named properties indicate that Ti_3SiC_2 can be considered as potential good candidate material for high temperature

structural application. Bering this in mind, the mechanical properties of Ti_3SiC_2 were studied more systematically as a function of temperature, deformation rate and grain size. The most of results from this work are presented here.

This thesis is a collection of published (chapter 2) [1], accepted for publishing (chapter 3) [2], or submitted for publishing (chapter 4 and 5) [3, 4] papers. The chapters are organized more chronologically than thematically. The author believe that such the order will help reader to learn gradually about the mechanical properties of Ti_3SiC_2 as he did during his work.

In chapter 2 preliminary results on mechanical properties of fine grained Ti_3SiC_2 are reported [1]. This chapter contains the first reported evidence of high strain rate sensitivity of Ti_3SiC_2. Clear evidence that brittle-to ductile transition depends not only on temperature, but on deformation rate too is one of the most important implications of that work. The results obtained from tensile creep tests carried out on fine fine and coarse grained structure are presented and discussed in more details in chapter 2 and 3. Chapter 4 discussed effect of the temperature, strain rate and grain size on brittle-to-ductile transition. In this chapter author tried to interrelate results obtained from creep, tensile, relaxation, strain transient dip and cycling loading-unloading tests and to develop overall picture of mechanical properties of Ti_3SiC_2 in function of temperature, microstructure and strain rate.

2. Tensile Properties of Ti_3SiC_2 in the 25-1300°C Temperature Range

2.1 Introduction

The ternary carbide Ti_3SiC_2 exhibits a unique combination of properties that have been studied intensively for the last several years [5-13]. It is a relatively light (4.5 g/cm³) solid [7, 8] that is oxidation resistant [9] and stable up to at least 1700 °C in inert atmospheres and vacuum. Like metals, it has excellent room temperature electrical (4.5 x 10^{-6} $\Omega^{-1}m^{-1}$) and thermal conductivities (37 W/m K) [7]. It is relatively soft (Vickers hardness $\approx$ 4 GPa), damage tolerant and resistant to thermal shock [6, 7]. Despite it's high stiffness – Young's and shear moduli of 325 GPa and 134 GPa [13] it is a readily machinable solid [7, 8]. The crystal structure is comprised of hexagonal nets of Si atoms separated by three layers of near-close-packed layers of Ti that accommodate C atoms in the octahedral sites between them [14].

Recently, results on the properties of fine and coarse-grained, predominately single phase Ti_3SiC_2 samples in compression and flexure were reported [6]. In both cases, a brittle-to-plastic transition occurs at $\approx$ 1200 °C, at which point large plastic deformation levels (strains >20 %) are obtained prior to failure. Oriented, macro-grained Ti_3SiC_2 (3-4 mm) samples loaded in compression deform plastically even at

room temperature [11]. Transmission electron microscopic work has shown that dislocations are mobile and multiply at room temperature [12]. The dislocations are mostly arranged either in arrays, wherein the dislocations exist on identical slip planes, or in dislocations walls, wherein the same dislocations form a low angle grain boundary normal to the basal planes [12]. A specific micro-mechanism of plastic deformation of Ti_3SiC_2 has been proposed recently [12], according to which re-adjustment of local stress and strain field occurs during high temperature deformation as a result of kink band formation and delamination of individual grains, in addition to regular slip. This plastic behavior is unusual for carbides and is believed to be partially due to its layered nature, and partially due to metallic nature of the bonding.

Although significant progress has been achieved in understanding the mechanical behavior of bulk, polycrystalline Ti_3SiC_2 in compression and flexure, as far as author is aware there are no reports in the literature dealing with its mechanical response under tension. The functional dependence of the tensile response of fine grained (3-5 μm) Ti_3SiC_2 on strain rates in the 25-1300 $^{\circ}$C temperature range is discussed in this chapter.

2.2 Experimental Procedure

The procedure for fabricating fine-grained Ti_3SiC_2 samples are reported in more detail elsewhere [4, 7]. Briefly, the specimens were prepared by mixing (ball

milling) titanium-hydride (-325 mesh, 99.99 %, Timet, AZ), silicon carbide ($d_m = 4$ μm, 99.5 %, Atlantic Engineering Equipment, Bergenfield, NJ) and graphite ($d_m = 1$ μm, 99 %, Aldrich Chemicals, Milwaukee, WI) powders to yield the desired stoichiometry. The mixture was cold-isostatically pressed and then annealed at 900 °C for 4 hours under vacuum to remove the hydrogen. Finally, the samples were hot-isostatically pressed at 1450 °C for 4 hrs., which results in a fine-grained (3-5 μm) microstructure. Scanning electron microscopy (SEM) analyses of HIPed specimens showed that they contained ~ 2 % by volume unreacted SiC.

Standard 2-inch long specimens SR51 [15] for tensile tests were electro-discharge machined and tested with no further surface preparation. Tensile tests were performed in air using a servo-electric Instron testing machine that automatically records force and cross-head displacement as a function of time. All tests were conducted in the 25-1300 °C temperature range at constant cross-head speeds ranging from 0.1 - 0.01 mm/min. Engineering strains were calculated by dividing cross head displacement divided by initial gage length. The presence of an oxide layer that formed during the testing never exceeded 80 μm, and was thus ignored in the stress calculations. Consequently, the stress levels reported here are to be considered lower bounds.

The surfaces that were parallel to the applied load were ground and polished and subjected to both SEM and light optical microscopy (OM) analysis. Fracture surfaces were also examined.

2.3 Results

Typical engineering stress-strain curves measured in tension performed at constant cross head speed of 0.1 mm/min in the 25-1300 °C temperature range are shown in Fig. 1. The room temperature tensile strength is 220 GPa. A change in the mechanical response from brittle to plastic is observed between 1100 °C and 1200 °C. At and below 1100 °C the failure of Ti_3SiC_2 is brittle; above 1100 °C the ultimate tensile stress, UTS[1], rapidly decreases with increasing temperature (Fig. 2). Concomitantly, the strain to failure increases (Fig. 2). Generally, the stress-strain response at temperatures above 1100 °C, exhibits three stages, labeled, respectively, A, B and C in Fig. 1: (a) an elastic regime, (b) a transient apparent "hardening" regime, and, (c) a distinct softening until failure. At higher temperatures the extent of the softening regime is significantly larger than the "hardening" regime. Such behavior suggests strong strain-rate sensitivity and led us to carry out the work described herein.

---

[1] It is important to point out that in contrast to ductile materials, the UTS does not signify the onset of necking.

The response of Ti_3SiC_2 changes from brittle to plastic as the cross head displacement decreases from 0.5 mm/min to 0.05 mm/min (Fig. 3). The strain to failure at 0.05 mm/min is at least 22 %, since this test was aborted before failure. Furthermore, as the strain rate decreases, the softening stage becomes more pronounced (Fig. 3).

The strain rate sensitivity of the stress, m, is defined as:

$$m = \frac{\partial \ln \sigma}{\partial \ln \dot{\varepsilon}}\bigg|_{\varepsilon,T} \approx \frac{\ln(\sigma_1 / \sigma_2)}{\ln(\dot{\varepsilon}_1 / \dot{\varepsilon}_2)}\bigg|_{\varepsilon,T} \quad (1)$$

where $\sigma, \varepsilon, \dot{\varepsilon}$, and T are respectively, the true stress, true strain, strain rate and temperature [16-18]. Indices 1 and 2 correspond to tests at two different cross head displacement rate. Strain rate was calculated as $\dot{\varepsilon} = v_{CHD} / l_{gage}$, where v_{CHD} and l_{gage} are cross head displacement rate and initial gage length, respectively. Re-plotting the results, shown in Fig. 3 as true-stress/true-strain (not shown), the m values were found to range from 0.42 to 0.52 depending on the strain at which it was calculated.

The strain rate sensitivity, m, can also be determined from step increase/decrease in cross head displacement rate during tensile testing [14, 18]. Results of such a test at 1200 °C are shown in Fig. 4. The black curves are the response of samples subjected to various jumps and drops in cross head displacement

rate. Horizontal arrows in Fig. 4 denote the stress at which the jumps and drops were initiated. The gray curves are those obtained from tensile tests at constant cross head displacement rate carried out on different samples. These results show that the response after the rate jump from 0.01mm/min to 0.1 mm/min is comparable to the specimen tested at 0.1 mm/min. The same behavior is observed during the rate drop tests, i.e. the curves after the rate drop follow the curves obtained from constant rate tests to which the drop was done. The calculated values of m from these tests are 0.52 and 0.56. The slight differences in mechanical response in strain-rate jump tests compared to the constant strain rate tensile test are can be attributed to experimental scatter.

To confirm these relatively high values of m, stress-drop tests during creep tests were carried out on the same sample at 1200 °C. Typical strain vs. time curves at 70 MPa are shown in Fig. 5. From these curves, the steady state creep rate was calculated. The test was repeated, after unloading, on the same specimen at different stresses (not shown). A log-log plot of the dependence of true stress on the steady state creep rate is shown in Fig. 6. The m obtained from this curve is 0.55, which is in good agreement with the m values calculated above.

It is necessary to emphasize that there was no visible macroscopic necking; the deformation was quite uniform along the entire gauge length in all tested specimens.

The SEM fractography of specimens that failed in a brittle manner shows a combination of inter- and transgranular fracture (Fig. 7a). A net of secondary cracks (denoted by horizontal arrows) spread over the fracture surfaces, connecting SiC inclusions (denoted by vertical arrows) that, for the most part, had completely separated from the matrix. The fracture surfaces of plastically deformed specimens, shown in Fig. 7b, show that the transgranular fracture mode dominates. Step-like transgranular fractures of some grains is also obvious (denoted by arrows in Fig. 7b). The latter is consequence of the layered structure. Well developed secondary cracks were not observed in a fracture surfaces of the plastically deformed material, although some large cavities (not shown) were observed.

The side surfaces of specimen that failed plastically were examined under the SEM in the near vicinity of the fracture plane. As shown in Fig. 8, the main microstructural feature is the presence of microcracks (denoted by vertical arrows in Fig. 8) parallel to the fracture surface. These microcracks appear to have initiated at SiC inclusions, but only in the narrow band close to the fracture surface; the remainder of the gauge length appears undamaged. In the same area, short microcracks (denoted by horizontal arrows in Fig. 8) that extend at angle of ~45° relative to the loading direction are also observed. These short cracks appear to interconnect cracks that were initiated at SiC.

Typical OM micrographs of a specimen that was loaded to failure at 1300 °C and cross head displacement rate of 0.1 mm/min are shown in Figs. 9a and b. Cavities

and microcracks perpendicular to the direction of applied load appear to be the main features. The cavities preferentially occur around the SiC inclusions. At some locations the microcracks appear to extend from one side of the specimen to the other. The damage zone in this case is much more uniform and extends along the entire gauge length.

2.4 Discussion

The results presented above unequivocally demonstrate the strong dependence of the tensile properties on temperature and strain rate. These results are consistent with previous measurements on the compressive and flexure behavior of Ti_3SiC_2 [6], in that a brittle-to-plastic transition occurs around ≈ 1200 °C. It is important to point out that the stresses at which the non-linearities in stress-strain curves are observed (denoted by arrows in Fig. 3) do not signify yield (i.e. activation of five independent slip systems). Rather it is stress at which enough damages has accumulated in the material to result in the non-linearity. This conclusion is supported by following observations:

i.   there is a significant asymmetry between the "yield" points in tension and compression. For example, for the FG material, the "yield" points in compression and tension at 1200 °C are 820 [26] and 48 MPa, respectively;

ii.   the "yield" points are strong functions of strain rate (Fig. 3); and,

iii.   the high hardening rates observed beyond the "yield" points at the lower temperatures and strain rates (Fig. 3).

These observations confirm that the damage accumulation in Ti_3SiC_2, documented during compression and flexure [6, 10-12] is, for the most part, also manifest in tension at elevated temperatures at elevated temperatures. Kinking of individual grains, however, has not been observed in this work.

One of the more important results obtained in this study is the high strain rate sensitivity, *m*, exhibited by Ti_3SiC_2. The slightly different values of m obtained for the fine-grained structure from the constant tests at constant cross head displacement rate (0.42 to 0.52) and from the creep test (0.55) can be attributed to the different testing methodologies and their underlying assumptions [16-18].

It is important to put these high values of m reported herein in perspective. Such high m values in tension are typically associated with superplastic oxide ceramics, mostly notably partially yttria-stabilized tetragonal zirconia [19-23]. Data reported to date for these materials show that they have m values that range from 0.3 to 0.6. The deformation of fine-grained Ti_3SiC_2 has another aspect in common with superplastic ceramics - larger elongation to failure than are typically observed in ceramics. However, a microstructural observation reveal that the physical process responsible for deformation in Ti_3SiC_2 seems to be different than that which occurs during superplasticity. While superplasticity in ceramics is commonly considered to

result from diffusionally accommodated grain rotation and grain boundary sliding, considerable microcracking and cavities formation occurs during deformation of Ti_3SiC_2 deformation. This indicate that the macroscopic strains result primarily from the formation of cavities and microcracks. Although grain rotation and grain rotation and grain boundary sliding may still occur, high degree of microcracking and cavity formation suggests that the diffusional accommodation process vital to superplasticity play a secondary role in Ti_3SiC_2. This suggests that the limitation on strain achievable in Ti_3SiC_2 is related to the linkage of microcracks and cavities that form during deformation. Another important distinction between superplastic ceramics and Ti_3SiC_2 lies in the grain size tested. Superplasticity is usually only observed when the grains are typically smaller that the ones tested here.

The question remains then, as to the cause of the high values of m observed in the present study. Since it has already been determined that the deformation mechanisms are not the ones occurring during superplasticity, the remaining plausible explanation is that the damage itself is responsible for the strain. This is suggested by observation that there is no decrease in cross-sectional area of the tensile specimen after deformation. Such a mechanism has been proposed by Luecke and Wiederhorn [24] to explain the creep deformation of Si_3N_4 and predicts an exponential relationship between stresses and strain rate at high stresses and a linear relationship at low stresses. The mechanism also suggests an asymmetry between tensile and compressive creep, an asymmetry that is indirectly apparent when the flow stresses, between tension and compression alluded above, are compared. The relationship

between stress and strain rate leads to the strain rate sensitivity of one at very low stresses, which gradually decreases with increasing stress. Over a small enough range of stress, the stress-strain rate curve would appear to fit a power-law dependance with strain rate sensitivity less than one. These speculations notwithstanding, it is hereby acknowledged that more work is needed before better understanding of deformation mechanism can be gained. Along those lines it is worth noting that the possibility of subcritical crack growth contributing to the overall strain to failure cannot be ruled out at this time.

The results of preliminary tests carried out on significantly coarser microstructures indicate that there are no qualitative differences between the fine and the coarser (100-300 μm) microstructures.

The microstructural observations presented above, show that SiC inclusions have a strong influence the nucleation and accumulation of damage and could contribute to failure at lower strain to failure. It is, thus, not unreasonable to assume that higher strains to failure can be attained in purer Ti_3SiC_2 samples.

2.5 Summary and Conclusions

The tensile response of fine-grained Ti_3SiC_2 samples in the 25-1300°C temperature is a strong function of temperature and strain rates. More specifically:

a) At cross head displacement rate of 0.1 mm/min, a brittle to plastic transition occurs somewhere between 1100 °C and 1200 °C in agreement with previously reported values in compression ant flexure.

b) Lower strength is attained in tension than in compression and flexure at same strain rate. At comparable strain rate, the tensile strength of Ti_3SiC_2 at 25 °C and 1200 °C are 220 MPa and 60 MPa, respectively; the compressive strengths are 1050 MPa and 820 MPa.

c) The strain rate sensitivity coefficients m determined from tensile test at constant cross head displacement rate, rate jumps and drop tests and stress-drop creep tests are from 0.42-0.56. These values of m are equal or greater than strain rate sensitivity of all other superplastic ceramics.

d) The large elongations to failure appear to result primarily from a high degree of damage tolerance and not from a structure that remains self-similar throughout deformation as is the case in superplasticity.

3. Tensile Creep of Fine Grained (3-5 μm) Ti_3SiC_2 in the 1000-1200 ^{o}C Temperature Range

3.1 Introduction

Recent results on the fabrication and characterization of the ternary carbide, Ti_3SiC_2, make it evident that this compound exhibits an unusual combination of properties [1, 5-11, 25, 26]. Its density (4.5 g/cm^3) is comparable to Ti, but it is more than twice as stiff with Young's and shear moduli of 325 GPa and 134 GPa, respectively [26]. It is a good electrical (4.5 x 10-6 $\Omega^{-1}m^{-1}$) and thermal conductor (37 W/m K) [7] at room temperatures. Vickers hardness of Ti_3SiC_2 is $\approx$4 GPa [7, 10] and it is highly damage tolerant and thermal shock resistant [6, 7, 25]. Furthermore, Ti_3SiC_2 is easy to machine by conventional high speed tool steels with no lubrication or cooling required (it can be cut by a manual hack saw) [7, 25]. The oxidation kinetics in air are parabolic [9], with parabolic rate constants that increase from 1×10^{-9} to 1×10^{-4} $kg^2m^{-4}s^{-1}$ as the temperature increases from 900 to 1400 ^{o}C. The protective oxide scales that form are layered; the inner layer is composed of silica, SiO_2, and rutile, TiO_2, while the outer layer is pure TiO_2.

It is by now well documented that a brittle-to-plastic transition occurs at temperatures between 1100 ^{o}C and 1200 ^{o}C (at a 10^{-4} s^{-1} cross-head displacement

rate), with large plastic deformation strains (>20 %) obtained prior to failure in compression, flexure [6] and tension [1]. The critical resolved shear stresses of 36 MPa at room temperature and 22 MPa at 1300 °C are estimated from compressive tests carried out on highly oriented large-grained (1-3 mm) samples as a function of the orientation [11].

Transmission electron microscopy (TEM) analysis of deformed and undeformed samples has shown that dislocations are mobile and multiply during deformation, even at room temperature [12, 28, 29]. The dislocations are overwhelmingly arranged either in arrays, wherein the dislocations exist on identical slip planes (basal plains), or in dislocation walls, wherein the same dislocations form a low angle grain boundary normal to the basal planes [12]. A dislocation density of about 10^{10} cm^2 was measured in the regions containing arrays [12], which is more value typical for metals than for ceramic materials. TEM of undeformed and plastically deformed samples revealed that dislocations were perfect, mixed basal plain dislocations with b=$1/3<11\bar{2}0>$ [28]. No other dislocations are observed by TEM suggesting that only two independent slip systems are available for deformation by dislocation glide. Thus, here plastic behavior does not imply that five independent slip systems become operative, but rather plasticity is possible by a combination of delamination and kink band formation of individual grains, as well as shear band formation [1, 6, 11, 12, 25].

Recently, the tensile properties of fine (3- 5 μm) grained Ti_3SiC_2 samples in air were reported in literature [1]. The results unequivocally demonstrated the strong dependence of the tensile response on temperature and strain rates. High plasticity levels were obtained with increasing temperatures and decreasing strain rates. The strain-rate sensitivity of ≈ 0.55 (corresponding to the stress exponent of 1.8) was high; more in the range of super-plastic ceramics. However, in contradistinction to superplastic materials, the large strains to failure seem to result primarily from a high degree of damage; not from a microstructure that remains self-similar throughout the deformation. Another important distinction between superplasticity and the deformation of Ti_3SiC_2 is that in the former the grains are typically smaller than the ones tested in this study [1].

Most recently, it has been shown that the mechanical response of Ti_3SiC_2 and ice are very similar [29]. This result stems from the fact that both are crystalline solids that are plastically very anisotropic; deformation occurs overwhelmingly, if not exclusively, by slip along the basal planes. This anisotropy, in turn, is why the response of both solids is so strain rate sensitive; if loaded rapidly, both are brittle, but if loaded slowly they are quite plastic. In both cases, stress concentrations and the rate at which they are relaxed dictate the nature of the mechanical response. In the brittle regime, microcracks and their linkage play a dominant role. This similarity is further confirmed in this work and is one of the leitmotifs of this chapetr.

This unusual combination of properties suggest that Ti_3SiC_2 is potentially a good candidate material for high temperature applications. Although significant progress has been achieved in understanding the mechanical behavior of Ti_3SiC_2 as a function of temperature and grain sizes, as far as author is aware, there are no reports on its tensile creep response. The purpose of this charpter is to report on the tensile creep properties in air of fine-grained (3-5μm) Ti_3SiC_2 carried out in the 1000 °C to 1200 °C temperature range and the 10 MPa to 100 MPa stress range. Also, the sensitivity of the creep properties to the sources of the starting powders is discussed in this chapter.

3.2 Experimental Procedure

The processing details can be found elsewhere [5]. Briefly, the specimens were prepared by reactive hot isostatic pressing (HIPing) of titanium-hydride or titanium, silicon carbide and graphite at 1450 °C under 40 MPa for 4 hrs. This procedure resulted in a fine-grained (3-5 μm) fully dense microstructure. To explore the sensitivity of the creep to the starting powders, three different Ti sources were used. The following mixtures henceforth denoted by S995, S997, S999, respectively, were used to make the tensile specimens:

S995 - Titanium (-325 mesh, 99.5%, Alfa Caesar, Ward Hill, MA).

S997 - Titanium-hydride (- 325 mesh, 99.7 % thin, Timet, Henderson, AZ).

S999 - (- 325 mesh, 99.9 %, Metamorphic Metals, Cleveland, OH).

In all mixtures the same graphite (dm = 1 μm, 99 %, Aldrich Chemicals, Milwaukee, WI) and SiC (-325 mesh, 99.5 %, Atlantic Engineering Equipment, Bergenfield, NJ) were used. Most of the work was carried out on the S995 series. Some of the creep tests were carried out on S999-series samples which were 21 volume % porous; these are denoted by SP999. These samples were fabricated cold isostatically pressing the powders using a pressure of 300 MPa to form green body, which was than pressureless sintered at 1600 °C for 4 hrs under argone. The pore size was of the order of 10 μm.

Dog-bone specimens SR51 (prismatic gage section: 2 x 2.5 x 12 mm^3) [15] were used for the tensile creep tests. They were electro-discharge machined and tested with no further surface preparation. The creep testing methodology is described in more detail elsewhere [30]. Briefly, a pneumatic cylinder applies the load to the specimen via SiC pull-roads. A pin and clevis arrangement transfers the load from pull rod to specimen. An air-filled furnace totally enclosing each specimen provides a uniform temperature field. The strain was measured by a laser-extensiometry system as a function of time [31].

Samples were heated to the testing temperature in ≈ 1.5 hrs and then soaked for ≈2-4 hrs prior to applying the load in order to insure temperature equilibration. During the heating and soaking a thin oxide layer formed.

Constant load creep tests were performed in the 1000 °C to 1200 °C temperature range using loads that corresponded to stresses that varied from 10 MPa to 100 MPa. Most of the tests were performed at constant temperature and constant load up to fracture. In a few tests, ($\approx$ 15 %), particularly the longer term ones, the stress was increased after enough data were collected for calculation of the minimum strain rate. However, in order to minimize potential problems with damage accumulation influencing the results, the stress was never increased more than once for any one sample.

In addition to the tensile creep tests, stress relaxation tests at 1000 °C and 1200 °C, as well a strain transient dip, STD, tests at 1100 °C were carried out. Both tests were carried out on an Instron 8500 testing machine using procedures suggested in the literature [32-37]. In both, tests the stresses and strains were monitored as a function of time. The strain was measured by a capacitive extensometer with a useful sensitivity to about 10^{-5}.

Briefly, the stress relaxation tests involved sample loading in tension at a constant strain rate up to the desired stress at which time the crosshead motion was abruptly stopped. The stresses and strains were monitored during the relaxation tests at 1200 °C as a function of time [4]. The instantaneous strain rate changes during the relaxation tests were obtained by differentiation of the strain vs. time curves. These values were then matched with the stress levels monitored at the same time that the strains were calculated.

In the STD tests the samples were loaded in tension at constant load σ until quasi-steady state creep was established and then the stress was immediately (< 1 s) decreased. Two STD tests were carried out on two separate samples. The first was at an initial stress, σ, of 40 MPa, followed by stress decreases, $\Delta\sigma$, of 4, 8, 12, 16 and 20 MPa; the second at an initial stress of 60 MPa, followed by $\Delta\sigma$'s of 8, 12, 16, 20, 28 and 32 MPa. After each stress decrease, the sample was reloaded to the original stress and the drop repeated at a larger $\Delta\sigma$. When the quasi-steady state was re-established at the reduced stress, the stress was increased immediately to its initial value σ. In both cases, the last load drop, which reduced the applied stress to almost zero (more precisely to 4 MPa which is the minimum stress required to keep the sample well aligned in the testing machine) was the most severe.

After the completion of the creep tests, the surfaces that were parallel to the applied load, were ground and polished for optical microscopy (OM) and scanning electron microscopy (SEM) analysis. To expose the grains, the polished samples were etched using 1:1:1 by volume $HF:HNO_3:H_2O$ solution and observed under OM and SEM.

The contribution of the cavities and cracks to the overall strain to failure was measured by a line intercept method using an image analysis system attached to the OM. The contribution of the cavities and cracks to overall strain to failure was

calculated as $\varepsilon = \Sigma l_i / L$ where l_i is a length of intersect of line with a cavity or crack, and L is overall length of the indentation line. The lines were chosen to be in the direction of the applied stress and extended from fracture surface to the end of the gauge area. For every sample the measurements were carried out on 5 lines. Microcracks and cavities smaller than 0.8 μm (the limits of resolution of the OM) were ignored; this decision is justified by subsequent results.

3.3 Results

Selected, but typical, strain, ε, vs. time, t, curves are plotted in Fig. 10a as a function of the applied stress, σ. The strain rate, $\dot{\varepsilon}$, vs. t curves for the same set of data are plotted in Fig 10b. Most of the creep curves exhibited three regimes:

i.   A transient regime in which the creep rate, $\dot{\varepsilon}$, gradually decreases with time (see inset in Fig. 10b); \

ii.   A quasi-steady state creep regime in which $\dot{\varepsilon}$ is more or less constant with time. This region is obviously present in all samples, except those tested at 100 MPa. Since this region corresponds to the minimum creep rate, $\dot{\varepsilon}_{min}$, it will sometimes be referred to as the minimum creep rate region. The values of $\dot{\varepsilon}_{min}$ were calculated from the slope of the best fitting straight line to the creep curves at the beginning of the quasi-steady state creep regime;

iii.   A tertiary creep regime in which $\dot{\varepsilon}$ is no longer linear with time, but gradually increases until failure.

The temperature and stress dependencies of $\dot{\varepsilon}_{min}$ are plotted in Figs. 11 and 12 as black open, closed, and hatched symbols. Bilinear regression of these results was carried out, assuming a power law relation between $\dot{\varepsilon}_{min}$, temperature and stress, [18, 38], i.e. assuming:

$$\dot{\varepsilon} = A\left(\frac{\sigma}{\sigma_0}\right)^n \exp\left(-\frac{Q}{RT}\right) \qquad (2)$$

A, n and Q in Eq. (2) are a stress independent constant, stress exponent, and activation energy for creep, respectively. The bilinear regression analyses, carried out on the logarithmic form of .Eq. 2, results in the following values: $A(s^{-1}) = \exp(19\pm1)$ s^{-1} , $n = 1.5\pm0.07$ and $Q = 445\pm10$ kJ/mol. Given the small values of the standard errors (95 % probability) and the high value for the coefficient of determination, $R^2=0.982$, suggest that the measured data are well represented by Eq. 2. It thus follows that $\dot{\varepsilon}_{min}$ can be best described by:

$$\dot{\varepsilon}_{min}(s^{-1}) = \exp(19 \pm 1)(\sigma/\sigma_0)^{1.5\pm0.07} \exp\left(\frac{-445 \pm 10 kJ/mol}{RT}\right) \qquad (3)$$

A plot of the mean values of this equation, shown as a solid black line in Fig. 13, appears to fit all the data reasonably well. A perusal of Figs. 11-13 also makes it clear that the creep results can be described by the same power law, with high confidence, irrespective of the purities of the starting titanium (S995, S997 and S999).

In an earlier study, specimens of the same shape and size as those used here were loaded in tension at a constant cross-head displacement rate at 1200 °C until they fractured [4]. The maximum (plateau) stresses reached during these tensile tests are plotted as a function of strain rate in Fig. 11, as gray down-triangles. These stresses represent the lower creep boundary, i.e. the lowest stress required to produce creep at the imposed rate and thus not surprisingly, lie slightly below the former. The gray dashed line (upper right) obtained by least square fitting of the tensile data has a slope of 1.7, which is a slightly higher than the slope obtained from creep. It is important to note that tensile test results at temperatures below 1200 °C do not match the results obtained from creep, the reason being that in the tensile tests at T< 1200 °C, a stress plateau was never reached, i.e. the samples fractured before the plateau was observed [4]. This is an important observation; its full implications is discussed in more detail below.

The data obtained from the stress relaxation tests at 1200 °C are plotted in Fig 11 as gray open down triangles. These results are also in excellent agreement with the data obtained from creep tests at the same temperature.

Selected, but typical, curves obtained from strain transient dip tests at 1100 °C are plotted in Fig. 14. Typical behavior after small stress reductions is shown in Figs. 14a and 14c. Small stress drops cause instantaneous contraction, followed by a period of zero creep rate. After an incubation time, creep resumes and the creep rate increases to a new steady value (inset in Figs. 14a and c). Large stress reductions, Figs. 14b and 14d, cause negative creep after the instantaneous specimen contraction. During negative creep, the rate decreases gradually to zero, and after some time increases again to a new steady state value. The negative creep regime is especially well pronounced for the last, and largest load drop, (shown on the right hand side of each of the panels shown in Fig. 14) which reduces the applied stress to almost zero.

As noted above, in all tests the stress was increased to its initial value (40 or 60 MPa), once a steady creep rate was reached at the lower stress level. During those stress increases, the creep curves exhibit a primary regime, followed by a quasi-steady state regime. The strain rates obtained from the STD tests at 1100 °C, at initial and reduced stresses are plotted in Fig. 11 as closed gray-up triangles. In general, and up to 40 MPa, these results are in excellent agreement with the data obtained from the creep tests. This is especially true when it is noted that each STD test was carried out on a single sample. The agreement for stresses at above 60 MPa (not shown) is not as good probably for the same reason, vis. the use of one sample for the entire test.

It is possible to use the results of the STD tests to calculate the recovery rate, $r = (\partial \sigma_i / \partial t)_\varepsilon$ and strain hardening coefficient, $h = (\partial \sigma_i / \partial \varepsilon)_t$, using the procedure

described by Lloyd and McElroy [34]. The ratio $\Delta\sigma/\Delta t$ gives the recovery rate (Δt is duration of the incubation period of zero creep rate) during small stress decreases. With small stress increases the ratio $\Delta\sigma/\Delta\varepsilon$ (where $\Delta\varepsilon$ is instantaneous strain increase upon load increase) gives the strain-hardening coefficient. The steady state creep rate is then given by the Bailey-Orowan equation as: $\dot{\varepsilon} = r/h$. The steady state strain rates calculated from the STD tests using this approach are in good agreement with the steady state rate measured during creep. For instance, the calculated steady state creep rates for the STD tests shown in Figs. 14a and 14c are: 1.0×10^{-6} s^{-1} and 1.82×10^{-6} s^{-1}, respectively; the steady state creep rates measured at 40 and 60 MPa are 8.1×10^{-7} s^{-1} and 2.1×10^{-6} s^{-1}, respectively.

The time to failure or lifetime, t_f, is a strong function of testing temperature and stress (Fig. 15a). Re-plotting this data on a log-log plot yields a series of parallel straight lines for each testing temperature (Fig. 15b). This suggests that the data can be fitted to a Monkman-Grant expression [39].

$$t_f = K_{MG}(\dot{\varepsilon}_{\min})^{-m} \tag{4}$$

where K_{MG} and m are the Monkman-Grant constant and exponent, respectively. A least squares fit of the results shown in Fig. 16, yields a slope, or an m value, of 0.9 ± 0.1 and a value of exp (-2 ± 1) for K_{MG}, if t_f is given in seconds. A perusal of these

results also indicate that the strains to failure of the purer samples (S999) are, for the most part but especially at lower stresses, higher.

The functional dependencies of the strains to failure on stresses and temperatures are shown in Fig. 17. At high stresses the strains to failure are ≈ 1-3% for all testing temperatures. As the stresses decrease both strains to failure (up to ≈ 8%) and scatter increase.

In addition, the creep tests of porous samples (SP999) were carried out. The test results presented in Figs. 18 and 19. The open symbols represent the results for the applied stress calculated by dividing the load by the nominal cross sectional area. The closed symbols represent the same results after correcting for the presence of the porosity. The corrected stress was calculated as the load divided by the effective cross section area, which is smaller than nominal one by ≈ 21%. The solid lines shown in Figs. 18 and 19 are the same ones shown in Figs. 11 and 15, respectively. A comparison of the two sets of results makes it amply clear that when corrected, the creep behavior of the porous samples is comparable to the dense ones.

Selected, but typical, low-magnification micrographs of the gage area in the vicinity of the fracture surface are shown in Fig. 20. Those micrographs clearly show — as in the case in tension [1, 4] - that deformation occurs without necking. Gage areas of specimens tested at high stresses (strains to failure ≤ 3%) are usually free of large cracks or any other visible damage (Fig. 20a). If some microcracks are present

they are few and typically only in the near vicinity of the fracture surfaces (Fig. 20b). With decreasing stresses and increasing failure strains (> 3%) more microcracks that spread over the gage area are observed (Fig. 20c). This is particularly obvious on the compositional OM micrograph of a polished and etched gage area shown in Fig. 21. Cracks (some of them denoted by vertical arrows) spread across almost the entire gauge area in a direction more or less perpendicular to the applied load (Fig. 21).

In all cases an oxide layer, the morphology of which is identical to the one reported on earlier (in that two layers form - an inner oxide layer of SiO_2 and TiO_2, and an outer layer of pure TiO_2 [9])- formed on the surface of the crept samples. At this juncture it is important to point out that the effect of oxidation on $\dot{\varepsilon}_{min}$ can be safely neglected. In one of the longest creep runs, viz. the sample held at 1000 °C under a stress of 40 MPa that failed after 375 hrs. The thickness of the oxide layer in this sample was in the range of 175 μm, which reduces the initial cross-sectional area by $\approx$ 30 %. If it were assumed, quite conservatively, that the entire oxide layer formed at the very beginning of the run and that its load bearing capability was negligible, that would increase the applied stress from 40 MPa to 56 MPa. According to Eq. 3, such an increase would increase $\dot{\varepsilon}_{min}$ by a factor of 1.6. This relatively small change is comparable to the noise level in the results. It thus follows that the influence on oxide formation can be neglected, especially in the early stages of creep when $\dot{\varepsilon}_{min}$ is measured.

If we consider the more severe oxidation conditions at 1200 °C, the thickness of the oxide layer measured for a specimen heated and soaked for ≈5 h and tested at 1200 °C and 40 MPa for 0.7 hrs is ≈100 μm. This oxide layer thickness reduces the initial cross sectional area by ≈15%, and increases the initial stress by ≈17%. Such a change would have a negligible effect on $\dot{\varepsilon}_{min}$. Thus, all results presented in this chapter are calculated based on the initial cross sectional area of the samples. Based on the data for the parabolic oxidation kinetics of Ti_3SiC_2 published in the literature [9], the oxide layer thickness after the 375 hrs. at 1000 °C, should be ≈ 105 μm, which is roughly half the value measured here. The reason for the discrepancy is not clear at this time and more detailed study on the oxidation kinetics is necessary in order to address this question.

The oxidation of the porous samples is more severe than the dense ones. For example, the thickness of oxide layer measured for a porous specimen heated and soaked at 1200 °C for ≈5 h and subsequently tested at and 40 MPa for 0.3 hrs is ≈160 μm. This thickness is significantly larger than the oxide layer thickness formed on fully dense material (≈ 100 μm) tested under similar conditions and estimated based on the results presented in the literature [9]. This oxide layer, formed mostly during heating and soaking, decreases the initial cross section area of samples by ≈30%. If we conservatively assume that the load bearing capability of oxide layer is negligible, the decrease in cross section area increases the nominal stress by ≈ 37%. Therefore

when both porosity and oxidation is taken into account, the increase in stress is closer to $\approx 80\%$, which is not negligible.

The results of the linear intercept method used to estimate the contribution of microcracks and voids to the overall strain to failure in the direction of the applied stress are presented in Table 1. Since the fine-grained microstructure is susceptible to pull-outs (especially small TiC particles) during polishing, it is sometimes difficult to distinguish such polishing artifacts from the damage formed during creep. Thus, the values listed in Table 1 represent an upper limit; the error is small however.

Higher magnification SEM micrographs of polished and etched samples are shown in Fig. 22. The deformation of grains by bending (denoted by arrows) is obvious in Fig. 22a, as well as, the delamination of some grains. Typical triple-point voids from which microcracks spread into adjacent grain boundaries are shown in Fig. 22b.

In order to monitor the damage evolution during creep, three tests were performed at 1000 °C and 60 MPa. The first two were interrupted after 17 and 45 h, while the third one was run until the specimen broke after 81.3 h. The creep results are shown in the central panel of Fig. 23. The reproducibility between the three sets of curves in noteworthy. Polished and etched SEM micrographs of gage and grip sections are compared in Figs. 23a to f, from which it is obvious that there is little microstructural differences between them after 17 and 45 hrs. (compare Figs. 23a

with 23d and 23b with 23e). In contradistinction, the well-developed network of intergranular cracks and delamination of some grains is quite noticeable in the gage area (Fig 23c), but absent in the grip area (Fig. 23f) for the sample that was crept till failure. The micrograph of the gage section (Fig. 23c) was taken in the vicinity of a big crack such as shown in Figs. 20 and 21. The voids that appear in both grip and gauge sections are pullouts.

3.4 Discussion

The following discussion is divided into two parts; the first deals with $\dot{\varepsilon}_{min}$ and possible dominant deformation mechanisms, the second addresses the mechanisms of rupture.

3.4.1 Deformation mechanism

A crucial question that needs to be answered before the creep mechanism can be understood is what fraction of the overall strain (if any) is caused by volume-conserving deformation (plastic deformation), and what fraction is caused by the volume-creating ones (i.e. voids, microcracks, etc.). The results shown in Table 1 indicate that a maximum of 50-80% of the overall strain to failure can be accounted for by voids and cavities. The balance must thus be due to volume-conserving

deformation and/or volume-creating deformation provided the size of the latter is below ≈ 0.8 μm. The presence of small triple void cavities is confirmed in high resolution SEM (Fig. 22b). It is important to note, however, that because of their very fine scale their density, or concentration would have to be quite large to seriously alter the results shown in Table 1. For example, if we assume, conservatively, that a 0.8 μm void is associated with every grain, and that the grains are of the smallest size (≈ 3 μm), the resulting change in volume due to these small voids is less than 0.3 vol. %. It is therefore reasonable to conclude that a sizable (> 20-50%) fraction of the tensile strain is accommodated by plastic deformation.

Since the great majority of cavities and microcracks are formed during the tertiary stage (Fig. 23), it follows that most of the strain produced during the primary and secondary creep regimes must be due to plastic deformation. This conclusion is probably not valid at the higher applied stresses, where steady state creep was probably never reached (Fig. 11 and see below).

As noted above, $\dot{\varepsilon}_{min}$ can be described by a power law expression over the entire range of testing temperatures and stresses (Fig. 13). Furthermore, since there are no changes in n and Q over the entire range of testing conditions, it is reasonable to conclude that one rate-controlling deformation mechanism is operative. The value of n obtained in this work, ≈ 1.5, is slightly lower than the values determined in our previous work (viz. 1.8) [1].

The interpretation of the rate controlling mechanism during creep is usually based on the magnitude of the activation energy for creep and the dependence of creep rate on stress. More work, especially, as a function of grain size, is required to better understand the creep mechanism(s). However, results on the creep of coarse (100-300 μm) grained samples (see Chapter 4) indicate that increasing the grain size by an order of magnitude decreases $\dot{\varepsilon}_{min}$, by a factor of 2 to 5 at best, under the same testing conditions [3]. This weak grain size dependence implies that diffusional creep and/or creep mechanisms in which grain boundaries or phases,-such as grain boundary sliding, etc. [40-44] - cannot play a central role. This is true despite the low stress exponent that would suggest otherwise. This is not to suggest that they do not play a role; simply that is cannot be the major role.

In the remainder of this section a compelling case is made for dislocation creep. Before doing so, it is important to reemphasize the close relationships between the deformation of ice and Ti_3SiC_2. Since both materials are anisotropic plastically, very quickly upon loading, large non-uniform states of stress are developed as the soft systems shear and transfer their stresses to the hard systems [23, 47]. The response of the material is then given by a competition between the accumulation of these internal stresses due to dislocation pileups, and their dissipation. If the rate of dissipation is high, both solids can exhibit considerable ductility; if not, fast fracture occurs. In other words, "recovery" processes control the creep behavior during steady state creep. Evidence for this conclusion includes:

i. The best and most direct evidence for the presence of large internal stresses is provided by the STD tests. Despite the sometimes quite different interpretations of the STD tests reported in the literature [32-37], there is no doubt that this test can provide information about the internal stresses. The occurrence of negative creep upon high stress unloadings (Fig. 14) is significant, and is usually interpreted to be a direct consequence of reducing the applied stress below the level of the internal stresses [35, 36]. The strain recovered during negative creep is usually referred as "anelastic" deformation [35, 36].

The occurrence of a period of zero creep during small stress reductions suggests that the creep is controlled by recovery processes. The good agreement between the steady state creep rates measured during the creep tests and those calculated from the Bailey-Orowan equation - derived assuming recovery-controlled creep - strongly suggests that the steady state creep in Ti_3SiC_2 is recovery controlled.

In addition to the STD results, indirect proof for the development of the large internal stresses during creep can be found in the shape of the creep curves (Fig. 10). The hardening occurring during primary creep, especially at the higher stresses, indicates a redistribution of the stresses as the softer systems relax and, as in ice [47], the stresses are transferred to the harder systems. If these internal stresses are high enough they could lead to the nucleation of

small cracks, which in turn would lead to tertiary creep, before a steady state creep regime is established; in agreement with our observations.

Finally direct evidence for sizable anelastic strains have been obtained during tensile tests at high temperatures as well. These results are discussed in chapter 5.

ii.   An added advantage of this interpretation is that it can now explain the strong strain rate dependence of the tensile tests [1, 4]. At high strain rates, large internal stresses would initiate microcracks, that in turn would lead to fast fracture before a plateau is reached. This is particularly the case at the higher strain rates when the time is insufficient for the relaxation of the internal stresses to occur. Conversely, if a plateau is reached this must imply that the hardening and recovery rates are balanced. The excellent agreement between the tensile and creep data shown in Fig. 11 (top right) is strong evidence for this interpretation.

On the other hand, the responses of the samples at high strain rates in both creep and tension are similar; failure occurs before quasi-steady state conditions can be established.

iii.   The excellent agreement between the creep rates calculated from the stress relaxation experiments and those derived from creep implies that their natures are similar.

The one problem, whose solution at this juncture is unclear, is how can plastic deformation of a random polycrystalline material occur with only two independent slip systems. As noted above. non-basal dislocations have never been observed in deformed Ti_3SiC_2 samples [12, 27, 28], which is not too surprising since their Burgers vector would have to be of the order of 17 Å. The same problem is encountered in ice [48]. The solution has been to postulate that dislocations climb normal to the basal planes, which provides four independent systems that are "self-consistent" enough to provide non-uniform plastic deformation [45, 46]. And while climb can certainly be a factor here, the negligible grain growth kinetics at the highest temperatures tested here [5], and the strength of the Ti-C bonds is problematic. Another distinct and more likely possibility for the dissipation of the internal stresses could be grain boundary decohesion at a very fine scale. This together with the propensity of Ti_3SiC_2 to delaminate and form kink bands (Fig. 22) maybe all that is required to account for the plastic deformations observed.

Finally and despite the fact that this is the first study of the creep Ti_3SiC_2 it is fair at this juncture to conclude that plastic anisotropy plays a important role during its deformation. Author believes the anisotropy leads to the development of large internal stresses and "recovery" processes control its creep behavior during the steady state. In other words, Ti_3SiC_2 and hexagonal ice [47] have much in common.

3.4.2 Creep damage accumulation and the rupture mechanism

Post-failure analysis of the crept samples provide important indirect evidence for the idea that the mechanical response of Ti_3SiC_2 at high temperatures is determined by the relative rates of stress accumulation and dissipation. For example, the strains to failure (Fig. 17) depend only on the testing stresses and increase rapidly with decreasing applied stresses. At higher stresses there is no quasi-steady state creep (Fig. 10) indicating that the damage occurs before the balance between hardening and recovery processes take place. Consistent with this interpretation is the fact that the samples that failed at high stresses contained significantly less damage (Fig. 20a), and, as importantly, the damage present was adjacent to the area surrounding the fracture surface (Fig. 20b), compared to the damage seen in the samples tested at lower stresses (Fig. 20c). In other words, the high internal stresses developed create intergranular cracks whose growth or coalescence occurs rapidly and locally, leaving the rest of the sample undamaged.

Conversely, samples tested at low stresses (strains to failure up to 8%) contain a large number of cracks over the entire gauge area (Figs. 20c and 21). In those samples, presumably, the slow deformation rates associated with the lower stresses allow for crack tip plasticity, delaminations and kink band formation. Direct evidence for these mechanisms at room and elevated temperatures has been shown elsewhere [48, 50]. Additional indirect evidence for crack tip plasticity is the fact that 21 vol. % porosity has little effect on the creep rate at the lowest temperatures (Fig. 17) and

even more astonishingly on the time to failure (Fig. 18). Without such crack tip plasticity, the stress intensification due to such a large volume fraction of interconnected porosity would have led to catastrophic failure at much lower strains and time than the ones observed. At the higher temperatures and stresses, oxygen appears to have a deleterious effect on $\dot{\varepsilon}_{min}$ (Fig. 17) even after correcting for the reduction in cross-sectional area due to pores. Oxidation of these samples during heating and soaking must also play a role, since it results in a significant reduction in the cross-sectional area of the porous samples.

It was repeatedly shown that Ti_3SiC_2 is damage tolerant at room and elevated temperatures [6, 10, 25, 29, 48, 50]. This work unambiguously shows that such damage tolerance also extends to tensile creep at lower stresses. This is corroborated by the micrographs shown in Figs. 20c and 21. Figure 21, which is a composite OM micrograph of the entire cross-section of a sample, is particularly noteworthy. In this micrograph a large network of cracks extends across the entire gage length. This sample was sustaining a stress of at least 40 MPa at 1000 °C when it failed after 375 h. This micrograph and others, present direct evidence for crack bridging and deflection, and indirect evidence for crack tip plasticity. For example, some of the cracks shown in Fig. 20c are ≈ 1mm long and extend almost half way across the gage length. It is not the presence of a few large cracks that is noteworthy, but rather the large network and density of these of cracks in general. From this and other micrographs, and in agreement with our earlier work [48, 50], it is obvious that crack

bridging (denoted by horizontal arrow in Fig. 21) and crack deflection are not only taking place, but that they are also potent toughening mechanisms.

Finally, it is important to underscore the practical implications of the results presented here. Based on the response of Ti_3SiC_2 to tensile stresses and strain rates [1, 4], its use, in most high temperature applications, will be creep limited. The damage tolerance and crack tip plasticity of this material can thus not be overemphasized. The results presented herein make it amply clear that Ti_3SiC_2 will not fail rapidly or catastrophically, especially at low stresses. This material can sustain considerable damage, both in extent and size, and still maintain its shape and load bearing capability, even in oxidizing atmospheres. This attribute in turn will allow for the timely detection of damage during routine maintenance of parts. This is especially true when it is appreciated that the size and extent of the damage observed here should be easily detectable using standard non-destructive techniques such as acoustic emission.

3.5 Conclusions

The tensile creep of fine-grained Ti_3SiC_2 samples over a range of testing temperatures (1000-1200 °C) and stresses (10-100 MPa) occurs by a combination of plastic deformation and cavitation. Plastic deformation appears to be dominant deformation mechanism over the quasi-steady state creep regime. In that regime the

minimum creep rate obeys power law creep with a stress exponent of 1.5 ± 0.07 and an activation energy of 445 ± 10 kJ/mol. The results obtained from the creep tests are in good agreement with the strain rates plotted as a function of maximum stresses obtained from simple tensile tests. Also, excellent agreement between the creep results and results obtained from stress relaxation tests suggests that the same atomistic processes are responsible for stress relaxation and creep during steady state.

Furthermore, the results of the STD tests suggest that the large internal stresses are developed during creep. Those internal stresses result in recoverable (anelastic) strains upon unloading. The development of internal stresses is not unexpected given the huge plastic anisotropy of Ti_3SiC_2. Development of these internal stresses is responsible for the initiation of the intergranular cracking and acceleration of the creep rate during the steady state creep. Interrupted creep tests have shown that most of the damage occurs during the tertiary stage suggesting that cavitation and internal cracking is responsible for the increase in creep rate during that stage. At high testing stresses, tertiary creep occurs before the steady state creep is established suggesting that the internal stresses developed during the primary creep have a important role in the initiation internal cracks.

4. Tensile Creep of Coarse-Grained (100-300 μm) Ti$_3$SiC$_2$ in the 1000-1200 °C Temperature Range

4.1 Introduction

This chapter is a continuation of our work to understand the mechanical response of Ti$_3$SiC$_2$ in general, and its high temperature tensile creep [2] and tensile [1] behavior in particular. Based on our results to date the mechanical response of Ti$_3$SiC$_2$, and by extension the other MAX phases, is characterized by high fatigue resistance [48, 50] and damage tolerance [5, 7] and a relatively high fracture toughness (8-12 MPa m$^{1/2}$) with R-curve behavior in which the fracture toughness can reach 16 MPa m$^{1/2}$. Furthermore, a brittle-to-ductile transition, BDT, occurs between 1100 and 1200 °C. The strain rate sensitivity of ≈ 0.55 (i.e. a stress exponent of 1.8) is relatively high for crystalline solids [1]. When loaded slowly, the stress-strain curves in tension reach a broad maximum in stress. The plateau stress is a function of strain rate and is lower for lower strain rates [1, 4]. Conversely, if loaded rapidly, the stress does not peak, but instead the material fails on the rising part of the stress-strain curves, i.e. the response is more brittle [1, 4].

In the same temperature and stress ranges reported on here, the tensile creep of 3-5 μm Ti$_3$SiC$_2$ samples [2], occurs in three stages; a primary, where strain rate decreases with time, a quasi-steady state and a tertiary stage. In general, creep occurs

by a combination of plastic deformation and damage accumulation. Plastic deformation is the dominant mechanism over the quasi-steady state creep regime, and the rate at which it occur can be well represented by a power law expression (see Eq. 3) with a stress exponent of 1.5 ± 0.07 and an activation energy of 445 ± 10 kJ/mol. Good agreement was also found between the creep results and those obtained from tensile tests and stress relaxation tests suggesting that the same atomistic mechanism(s) is responsible for the plastic deformation observed in all those tests [2]. Furthermore, the results of strain-transient dip tests [2] make it evident that internal stresses developed during creep are responsible for recoverable (anelastic) strains upon unloading. The development of these internal stresses is not surprising given the huge plastic anisotropy of Ti_3SiC_2. The development of internal stresses is also believed to be responsible for initiation of the intergranular microcracking and the acceleration of creep during the tertiary regime.

In these respects and in many others, it was very recently shown that Ti_3SiC_2, and hexagonal ice are quite comparable, both at the atomic and macroscopic levels, when deformation is concerned [29]. Since both are very plastically anisotropic, with only two independent slip systems, homogenous plastic deformation is not possible; instead large internal stresses develop. If these stresses are not dissipated, the behavior is quite brittle. However, if they can be dissipated, the response is much more ductile. This interpretation explains, in large part, the strong strain rate dependencies of the mechanical response.

And while ice remains brittle even at 0.95 of its melting point, as noted above, Ti_3SiC_2 goes through a BTD at temperatures between 1100 °C and 1200 °C (at a 10^{-4} s^{-1} cross-head displacement rate). This BTD is well documented for compression, flexure [5, 51] and tension [1]. In most metals, the DBT is associated with the thermal activation of additional slip systems, which in turn result in an increase in fracture toughness. In Ti_3SiC_2 the fracture toughness drops from around 8 MPam$^{-1/2}$ to about 4 MPam$^{-1/2}$ above the BDT temperature [50]. And while the exact nature of the DBT is not understood at this time, the lack of any evidence for the presence of other than basal dislocations even after high temperature deformation, leads us to eliminate the activation of other slip systems as a cause.

Tensile creep of coarse-grained, CG, Ti_3SiC_2 samples, in the 1000 °C-1200 °C temperature range and the 10 MPa to 100 MPa stress range is discussed in this chapter. Whenever, possible the results are compared with our previous work on creep of fine-grained, FG, Ti_3SiC_2 samples [2].

4.2 Experimental Procedure

The processing details are described elsewhere [5]. Briefly, the CG samples, were prepared by reactive hot isostatic pressing (HIPing) of titanium (-325 mesh, 99.5%, Alfa Caesar, Ward Hill, MA), silicon carbide (-325 mesh, 99.5 %, Atlantic Engineering Equipment, Bergenfield, NJ) and graphite (d_m = 1 μm, 99 %, Aldrich

Chemicals, Milwaukee, WI) at 1600 °C under 40 MPa for 6 hrs. The resulting samples are fully dense, predominantly single-phase, with plate-like grains of the order of 100-300 μm.

In addition a duplex microstructure was produced from the same initial powders by HIPing at 1400 °C under 40 MPa for 6 hours in order to get a FG structure and an additional HIPing cycle at 1600 °C and 40 MPa for 4 hours in order to allow only a few grains to grow. The resulting duplex microstructure, DS, consists of long plates, that in some cases exceed 1 mm in length, with large pockets of fine grains (up to ≈10 μm) between them.

The details of the creep measurements can be found in Ref. 2. In short, electro-discharge machined dog-bone specimens SR51 (prismatic gage section: 2 x 2.5 x 12 mm^3) [52] were tested with no further surface preparation. The creep test methodology is described in more detail elsewhere [30]. The strain was monitored by a laser-extensometry system as a function of time [31]. All samples were heated to the testing temperature in ≈ 1.5 hour and held at test temperature for anywhere from 2 to 4 hrs. before the load was applied.

Most creep tests were performed at constant temperature and constant load up to fracture, or until the tests was aborted. In a few cases, the load was increased after enough data were collected for the calculation of the minimum creep rate. However, in

order to minimize potential problems with damage accumulation influencing the results, the stress was never increased more than once for any one sample.

In addition to tensile creep, stress relaxation tests at 1200 °C and strain transient dip, STD, tests at 1150 °C were carried out on an Instron 8500 testing machine, using procedures described in more detail in the literature [32-37]. In both, the strain was monitored as a function of time by a capacitive extensometer with a useful sensitivity to about 10^{-5}. In the relaxation tests, the samples were loaded at a constant strain rate up to the desired stress, at which time the crosshead motion was abruptly stopped, and the stresses and strains were monitored as a function of time [4].

For the STD tests, a sample was loaded and held at a stress, σ, until the strain increased more or less linearly with time at which point the load was immediately (< 1 s) decreased by $\Delta\sigma$. Three sets of STD tests were carried out on two separate samples. The first was at an initial σ of 40 MPa, followed by $\Delta\sigma$'s, of 4, 8, 12, 16, 20 and 24 MPa; the second at initial stress of 60 MPa followed by $\Delta\sigma$'s, of 4, 8, 16, 24 and 26 MPa; and third at an initial stress of 80 MPa, followed by $\Delta\sigma$'s of 4, 8 and 16 MPa. When steady state was re-established at the lower stresses, the stress was again increased to the initial σ and the test repeated. In the end of all STD tests the stress was reduced to 4 MPa, which was the minimum stress required to keep the sample well aligned in the testing machine.

Fracture surfaces of most samples tested were examined by scanning electron microscopy (SEM). In addition, the surfaces of selected creep samples that were parallel to the applied load were ground and polished for optical microscopy (OM) and SEM analysis. Some of the polished samples were additionally etched using 1:1:1 by volume $HF:HNO_3:H_2O$ solution [6] in order to better expose the grains

As in our previous work [2], the contribution of cavities and cracks to the overall strain to failure was measured by OM using the line intercept method. The contribution of polishing artifacts such as pullouts, was taken into account by subtracting the values measured in the grip area from those measured in the gauge area for any given sample. Microcracks and cavities smaller than 0.8 μm (the limits of resolution of the OM) were ignored; a simplification that has even less bearing on the conclusions reached here than when it was used in the FG case [2].

4.3 Results

The effects of time, t, and σ on the tensile strain, ε, at 1100 °C are plotted in Fig. 24a. The strain rate, $\dot{\varepsilon}$, vs. t curves for the same set of data are plotted in Fig. 24b. As in the case of the FG structure [1], three regimes are distinguishable:

i. An initial transient regime, where $\dot{\varepsilon}$ gradually decreases with t (inset in Fig. 24b).

ii.   A secondary or quasi-steady state creep regime in which $\dot{\varepsilon}$ is more or less constant with time. This region is not present in samples tested at stresses of 60 MPa or higher. In this regime the deformation rate shows a minimum, and this is henceforth referred to as the minimum creep rate, $\dot{\varepsilon}_{min}$.

iii.   A tertiary creep regime, in which $\dot{\varepsilon}$ increases until failure.

A ln-ln plot of $\dot{\varepsilon}_{min}$, vs. σ as a function of temperature, T, is shown in Fig. 25; an Arrhenius plot of $\dot{\varepsilon}_{min}$ in shown in Fig. 26. The $\dot{\varepsilon}_{min}$ values for the DS are plotted in Fig. 25 by dashed lines. Not surprisingly, the creep rates of the latter fall between those of the FG [2] and CG microstructures. Preliminary results on $\dot{\varepsilon}_{min}$ in compression creep of the CG structure at 1200 °C are also plotted as hatched symbols in Fig. 25. The values of $\dot{\varepsilon}_{min}$ in compression are lower by a factor of ≈ 3, compared to those in tension at the same testing temperature.

Bilinear regression analysis (95 % probability) of the results was carried out, assuming the power law relation between $\dot{\varepsilon}_{min}$, T and σ to be [38, 18]:

$$\dot{\varepsilon}_{min} = A\sigma^n \exp\left(-\frac{Q}{RT}\right) \tag{6}$$

where A, n and Q are, respectively, a stress independent constant, stress exponent and activation energy for creep. The regression analysis, on the logarithmic form of Eq. 6,

yields: $A(s^{-1}) = exp(17.3\pm1)$ s^{-1}, $n = 2.0\pm0.1$ and $Q = 458\pm12$ kJ/mol. The small values of the standard error, and the high value for the coefficient of determination ($R^2=0.974$), indicate that the $\dot{\varepsilon}_{min}$ can be well represented by Eq. 6, over the entire range of testing temperatures and stresses, viz.:

$$\dot{\varepsilon}_{min}(s^{-1}) = \exp(17\pm1)\sigma^{2.0\pm0.1} \exp\left(\frac{-458\pm12kJ/mol}{RT}\right) \qquad (2)$$

The goodness of the fit is obvious in the ln-ln plot of $\dot{\varepsilon}_{min}$ vs. σ (Fig. 27). Also included in this plot are the results for the FG microstructure [2]. Figure 28 is a plot of $\dot{\varepsilon}_{min}$ vs. reciprocal temperature, using $n=1.5$ for the FG structure [2], and $n=2.0$ for CG one; confirming once more that Q is not a function of microstructure, and that, at all temperatures and stresses $\dot{\varepsilon}_{min}$ of the CG samples is lower than their FG counterparts.

Since n is a function of grain size, it is not possible to calculate the grain size exponents, p, directly from the power law equations. Instead, the grain size effect was quantified assuming $\dot{\varepsilon}_{min} \propto d^{-p}$, where d is the average grain size. The results are presented in Table 2, assuming average grain sizes of 5 µm and 150 µm for the FG and CG microstructures, respectively. The differences in $\dot{\varepsilon}_{min}$ between the two microstructures increase as σ decreases; i.e. p increases as σ decreases.

Coarse-grained specimens of the same shape and size as those used in this study were tested in tension at a constant cross-head displacement rate at 1200 °C [4]. The gray down triangles (Fig. 25) represent the maximum (plateau) stresses reached during these tests as a function of strain rate. These stresses represent a lower creep boundary, i.e. the lowest stress required to produce creep at the imposed rate, which is why they lie slightly below the former. As in the case of the FG samples [2], the results of the tension and creep tests are only comparable when a stress plateau is reached in the former.

Data points obtained from the stress relaxation tests at 1200 °C [4], represented in Fig. 25 by small open circles, are in excellent agreement with the data obtained from creep tests at the same temperature.

Moreover, results from the STD test carried out at 1150 °C, (black solid squares in Fig. 25) are in good agreement with those obtained from creep tests at the same temperature. Select, but typical, curves obtained from STD tests at 1150 °C are plotted in Fig. 29. Small stress drops cause instantaneous contractions, followed by a period of zero creep rate, (Figs. 29a and 29b), after which creep resumes and the creep rate increases to a new steady value. Large stress reductions (Figs. 29b and 29d) are followed by regions of negative creep after the instantaneous contractions. The creep rate eventually goes to zero before it ultimately increases to a new steady state value. The negative creep regime is especially well pronounced for the last, and largest load drop (Fig. 29a) which reduces the σ to almost zero.

As in our previous work [2], the recovery rate, r, and strain hardening coefficient, h, were calculated from the STD tests using the procedure described by Lloyd and McElroy [32]. The steady state creep rate was then calculated using the Bailey-Orowan equation as $\dot{\varepsilon} = r/h$. The strain rates calculated using this approach are in good agreement with the $\dot{\varepsilon}_{min}$ values measured during creep. For instance, the calculated steady state creep rates for the STD tests shown in Figs. 29a and 29c are: 8.64×10^{-7} s^{-1} and 1.83×10^{-6} s^{-1}, respectively; the $\dot{\varepsilon}_{min}$ rates measured at 40 and 60 MPa are 8.1×10^{-7} and 1.8×10^{-6} s^{-1}, respectively.

The time to failure or lifetime, t_f, vs. stress plot for different temperatures is shown in Fig. 30a. Re-plotting this data on a log-log plot yields a series of parallel straight lines for each testing temperature (Fig. 40b). Also included in Fig. 5 are the lifetimes of the FG samples, which are significantly shorter than the CG samples. The results plotted in Fig. 5b suggest that the data can be fitted to a Monkman-Grant type expression [22]:

$$t_f(s) = K_{MG} \dot{\varepsilon}_{min}^{-m} \qquad (7)$$

where K_{MG}, and m, is a constant and the Monkman-Grant exponent, respectively. A least squares fit of the results, (Fig. 31), yields an $m = 1 \pm 0.06$ and $K_{MG} = \exp(-2 \pm 0.3)$.

The functional dependencies of the strains to failure on stresses and temperatures are shown in Fig. 32. At high stresses the strains to failure are ≈ 1-3% and thus close to strains to failure of the FG microstructure [2]. As the stresses decrease, the strains to failure increase.

Pictures of some of the specimens tested in creep are presented in Fig. 33, together with an initial specimen. Plastic deformation of the tested samples is clearly observable. The change in color is due to the formation of oxide layers.

Typical, low-magnification micrographs of the gage area in the vicinity of the fracture surface, Fig. 34, shows that – as in the case in FG samples in creep [2] or tension [1] - the deformation occurs without necking. Specimens deformed in creep up to ≈3% are usually free of large cracks, or any other visible damage, within the gage area (Fig. 9a). If some microcracks are present they are few, and typically only in the near vicinity of the fracture surfaces (Fig. 34b). With increasing failure strains (> 3%) more microcracks that spread over the gage area are observed (Figs. 34c and 34d). The network of cracks is obvious on the compositional OM micrograph of a polished and etched gage area shown in Fig. 35. Cracks spread across almost the entire gauge area in a direction more or less perpendicular to the applied load. Encircled detail is an example of a bridging grain.

Clear evidence of slip can be seen in the OM micrograph of a large grain in a duplex microstructure tested at 1000 °C and 40 MPa, Fig. 36. Steps at the grain

boundary are presumably formed by the slip along the basal planes, whose orientation is clear in the figure. Such a feature has never been observed in undeformed samples. Typical OM micrographs of delamination process and deformed lamina are shown in Figs. 37-39.

SEM micrographs of polished and etched samples are presented in Figs. 40-42. The bent grain shown in Fig. 40 is clear evidence of plastic deformation. Here again, such features have been never observed in non-deformed samples. Delamination and kinking are shown in Fig. 41. Crack bridge is shown in Fig. 42.

Selected, but typical SEM micrographs of the fracture surfaces are presented in Figs. 43-46. The kinked lamina "sticking out" from the fracture surface is shown in Fig. 43. Such a grain must have served as a crack bridge before rupture. Figure 44 demonstrates a typical transgranular fracture (on the left) and intergranular fracture (on the right). Another "bridging" grain sticking out from the fracture surfaces is shown in Fig. 45, while the "pullout" of a bridging grain is shown in Fig. 46.

From the results presented in Table 3 it is obvious that the fraction of the strain due to cavities and microcracks increases as the testing stress decreases. Also, comparing the results from the tests carried out at 1050 °C and 60 MPa for different times (denoted by asterix in Table 2), it is possible to conclude that the fraction of strain from cavities and crack increases with the time.

In order to monitor more precisely damage evolution during creep, three tests were performed at 1050 °C and 60 MPa. The first two were interrupted after 21 and 49 hrs., while the third one was run until the specimen broke after 94.5 hrs. The samples were polished very carefully using 3 and 1 μm diamond and a 0.05 μm suspensions of colloidal silica using low load in order to avoid pullouts. The creep results, shown in the central panel of Fig. 47, demonstrate good reproducibility. SEM micrographs of gage and grip sections are compared in Figs. 47a to f. The gage area of the sample tested for 21 hrs. is free of damage (compare, Figs. 47a and d). Some grain boundary decohesions are observed in the samples tested for 49 hrs. at higher magnifications, (inset in Fig. 47b). Microcracks and/or grain boundary decohesions (denoted by arrows) are obvious in the sample tested until fracture. In contrast microphotographs of the grip area in all three cases are free of damages, confirming that the damage observed in the gage area occurs during testing.

In all tested samples an oxide layer formed during the creep tests. Its morphology is identical to the one reported on earlier, in that two layers form - an inner oxide layer of SiO_2 and TiO_2, and an outer layer of pure TiO_2. Since the effect of loading on the oxidation processes will be discussed in a separate study it is not considered here. It is worth noting, however, that the oxide layers that form in the beginning of the test do not influence the measured values of the minimum strain rate for the same reasons discussed in Ref. [2].

4.4 Discussion

Based on the totality of our work to date on the mechanical behavior of Ti$_3$SiC$_2$ there is little doubt that: a) dislocations play a dominant role, b) large internal stresses develop due to the paucity of operative slip systems. c) the mechanical response of Ti$_3$SiC$_2$ is essentially dictated by a competition between the rates of generation and dissipation of these internal stresses. d) At higher temperatures and/or lower strain rates these internal stresses can dissipate. The exact mechanisms for how that occurs are not totally understood at this time, but most probably include, grain delaminations and kinking, and grain boundary and decohesion, among others. The results presented here are not only in complete agreement with these conclusions, but more important supply further strong evidence to their validity.

4.4.1 Phenomenological Observations

Since $\dot{\varepsilon}_{min}$ can be described by a single power law (Eq. 6; Figs. 25-28) it is fair to assume that the same thermally activated rate-controlling mechanism(s) is operative over the entire range of testing temperatures and stresses. Furthermore, since the activation energies for the CG and FG samples [2] are almost identical, it is again fair to assume that the same thermally activated rate controlling mechanism(s) is operative in both microstructures.

The results shown in Table 3 indicate that 20-70% of overall strain to failure can be accounted for by voids and cavities that are larger than 0.8 μm. As discussed previously [2], small cavities (< 0.8 μm) usually present at triple points, can not significantly alter the results shown in Table 3. This is especially true for CG structure wherein the number of triple points per unit volume is even smaller than in the FG samples. The micrographs provide unambiguous evidence that plastic deformation by basal slip (Fig. 31), grain bending (Fig. 40) and kinking (Fig. 41) occur in creep. The interrupted creep tests (Fig. 47) also demonstrate that the majority of microcracks and cavities form during the tertiary creep stage. Thus, most of the strain produced during the quasi-steady state creep has to be due to plastic deformation. It is important to note that this conclusion is not valid at higher stresses where steady state creep was probably never reached (Fig. 24).

The creep rate of duplex microstructure is slightly higher than the creep rate of CG samples at same conditions (Fig. 25), which is not surprising since the duplex structure consist of extremely large grains separated by regions with of fine grains. The overall creep behavior is thus mostly controlled by creep of the pockets of fine grains.

4.4.2 Evidence for Internal Stresses and Stress Relaxations

As in the case of the FG structure [2], the STD tests provide clear evidence for the generation of large internal stresses during creep (Fig. 29). Negative creep upon high stress unloading is usually considered evidence for the presence of internal stresses whose value is higher than those corresponding to the new lower stress to which the system is subjected [35, 37]. The reversible strain, recovered during the negative creep is usually termed "anelastic" deformation. The period of zero creep upon small σ reductions is usually interpreted as direct evidence for recovery processes [35, 36]. The creep rate calculated from SDT tests using Bailey-Orowan equation (derived assuming recovery controlled creep) are in good agreement with those measured in the creep test. This fact indicates that creep of CG Ti_3SiC_2, like its FG counterpart [2], and ice [47], is most probably recovery controlled.

Comparing the shapes of the creep and tensile curves at different strain rates and/or stresses sheds more light on the problem. When the stresses used in creep, or the strain rates used in tension are both low, good agreement is obtained between the two-sets of data (Fig. 25). Conversely, at stresses that are much higher than 50 MPa steady state creep is never reached (Fig. 24) and the stress-strain curves in tension do not exhibit a maximum or plateau. The simplest explanation for both observations is that the response of the material is determined by the relative rates at which the internal stresses accrue and dissipate.

The excellent agreement between the results obtained from creep and stress relaxation tests (Fig. 25) implies that the same mechanisms are operative in both. It is worth noting that the stress relaxation abilities of Ti_3SiC_2 are limited; after several stress relaxation tests are repeated on the same sample, the agreement is less good. This suggests that after several stress relaxation tests, not all the internal stresses are relaxed during each cycle, which in turn leads to the microcracking,

4.4.3 Creep Mechanisms

Determining the rate controlling atomistic mechanism in creep, especially when the values of n and p do not agree with those predicted by classic creep models, is not a trivial exercise. Even in a material as well studied as ice, the situation is still not entirely clear. These caveats notwithstanding, the results presented herein make some major strides in understanding creep in Ti_3SiC_2. The most compelling evidence that diffusion and/or grain boundary creep are not the dominant creep mechanisms can be found in the low values of p (Table 2). The classic models for diffusion and/GB controlled creep have p values of 2 to 3 [40, 42, 53, 54]; the highest value of p measured here is ≈ 0.5. That is not to say that grain boundaries do not play a role - they clearly must since ε_{min} for the FG samples are higher than those of the CG samples (Fig. 28) - but simply that they do not play a dominant role.

Further evidence for the importance of dislocation creep is the mild asymmetry in $\dot{\varepsilon}_{min}$ in compression and tension (the former is lower by factor of ≈ 3, Fig. 27). Such mild asymmetries are exhibited even some by ductile metals. For example, in the dislocation controlled creep region, the tensile creep rate of polycrystalline aluminum is higher than its compressive creep rate by factor of ≈ 2 [35]. In contradistinction, the asymmetries in structural ceramic such as Si_3N_4, Al_2O_3, SiC, etc, are much stronger [55]. The creep rates in tension is 10 to 100 times faster than that in compression; an asymmetry that is attributed to the presence of viscous grain boundary phases.

Creep mechanisms based on grain boundary sliding accommodated by dislocation motion ($n=3$, $p=1$) [53] or ($n=2$, $p=2$) [53, 54] are also not in good agreement with the results obtained here. In other words, there is no single creep mechanism that predicts the low values of n and p measured here. A possible explanation could be in activation of two deformation mechanisms such as grain boundary sliding and deformation by dislocation creep, with the latter dominating. Such combinations of mechanisms could explain differences in the n values between the FG and CG microstructures as well as the increase in grain size exponent with decreasing strain rates. Furthermore, the role of the internal stresses cannot be neglected; their presence must affect the values of n. These comments notwithstanding, it is hereby acknowledged that more work is required to better understand creep in Ti_3SiC_2.

4.4.4 Lifetime and Rupture

Not only is ε_{min} in the CG structure lower than in the FG one (Fig. 28), but t_f of the former is considerably longer (Fig. 30); an enhancement that increases with decreasing testing stresses (Fig. 30). The main reason for this observation must be the higher damage tolerance of the CG structure [5-7, 29, 48, 50]. In other words the coarse grains, as a direct result of their size, can sustain much higher bridging stresses than the fine ones. In the remainder of this chapter, some compelling microstructural evidence in support of this notion are presented. The large concentration and size of the microcracks is obvious in Figs. 34 and 35, especially at lower stresses. Comparing these micrographs with those of the FG samples [2], it is obvious that the size of the microcracks scale with grain size.

The microstructural evidence suggests the presence of two different crack bridging mechanisms. The first is shown in the encircled areas in Fig. 35 and in Figs. 42, 45 and 46. Here grains perpendicular to the direction of crack propagation serve as classic crack bridges. These grains can absorb energy either by plastic deformation (kinking) (Fig. 42) or by pulling out (encircled area in Fig. 35). More direct evidence for this mechanism is also present when the fracture surfaces are examined (Figs. 45 and 46).

The second mechanism is more unusual. It begins with delaminations that are initiated on opposite sides of a single grain but on different basal planes (Fig. 37).

These lamella can also be formed from only one side of a grain, if they are in the vicinity of a void at the grain boundary (Fig. 38). With further deformation, the separated lamina can deform significantly by bending before rupturing (Fig. 39 and 43). This bending occurs by the formation of kink bands, the boundaries of which must clearly impede further delamination. For example, had the bending shown in Figs. 38 and 39, not occurred by dislocation motion, the delamination would have quickly run across the grain. The fact that it does not is significant and indirectly confirms our kink band model for toughening in these materials [48, 50].

Samples deformed at high stresses, i.e. low strains to failure, fail with significantly less damage (Figs. 34a and 34b) and, the damage present is in the vicinity of the fracture surface. This observation is consistent with the fact that samples tested at higher stresses do not exhibit steady state creep but fail before the balance between hardening and recovery process take place.

4.5 Conclusions

The tensile creep of coarse-grained T_3SiC_2 samples over a range of testing temperatures (1000-1200°C) and stresses (10-100 MPa) is characterized by a combination of plastic deformation that is dominant during the quasi-steady state, and cavition that predominantly takes place during the tertiary creep. Minimum creep rate obeys power law creep with a stress exponent of 2.0±0.1 and an activation energy of

458±12 kJ/mol. Almost identical activation energies for FG [2] and CG samples suggest that the same thermally activated rate controlling mechanisam(s) is operative in both microstructure. The relatively small grain size exponent (<0.5) implies that grain boundary sliding cannot be the dominant creep mechanism.

As in the case of fine grained structure the results obtained from the creep tests are in good agreement with the results obtained from simple tensile tests at low strain rates and stress relaxation tests. This suggests that the same atomistic processes are responsible for stress relaxation, plastic behavior in tension and creep during steady state. STD tests suggest that the large internal stresses are developed during creep. Those stresses are recoverable (anelastic) strains upon unloading. Thus, creep during the steady state is controlled by the balanced rates of generation and dissipation of internal stresses. Internal stresses developed during the creep are responsible for the initiation of the microcracks and thus, acceleration of the creep rate during the tertiary creep.

The CG microstructure exhibits better creep properties that the FG counterpart [2]; the minimum creep rate in CG structure is lower and the lifetime is longer that in the FG one. The significant damage tolerance of CG microstructure in creep can be attributed to the two different crack bridging mechanism. One of them is based on delamnination of the grains followed by intensive plastic deformation (bending) of the lamina that serves as a crack bridge. In the other, large grains perpendicular to the direction of crack propagation serve as a crack bridge.

5. Effect of Temperature, Strain Rate and Grain Size on

Mechanical Response of Ti$_3$SiC$_2$ in Tension

5.1 Introduction

Since Ti$_3$SiC$_2$ was successfully synthesized as a fully dense, single phase bulk material at Drexel University in 1996, many of its properties have been characterized. Ti$_3$SiC$_2$ combines some of the best attributes of ceramics and metals. Its thermal properties are comparable to those of stoichiometric TiC. It has the same density as Ti [7, 10], but is roughly three times as stiff (325 GPa) [56] and yet is readily machinable [7, 25]. It is stable in inert atmospheres to temperatures above 2200 °C. In air it is oxidation [9], fatigue [50, 50], and thermal shock resistant [6, 7, 25], as well as, damage tolerant (K$_{IC}$= 8-16 MPam$^{1/2}$) [50, 50]. It is twice as conductive as Ti metal, both electrically and thermally [9, 25].

Unlike most ceramic materials, edge cracks do not emanate from the corners of indentation tests [10]. The intensive kinking, buckling and bending of the grains observed in the vicinity of the indentation indicated that Ti$_3$SiC$_2$ exhibits pseudo-plastic behavior. A brittle-to-ductile (BTD) transition occurs at $\approx$ 1100 °C in compressive and flexure tests [6, 51]. Above the BTD temperature Ti$_3$SiC$_2$ deforms plastically with deformations that can exceed 25%. Also, compressive testing of

highly oriented very coarse-grained (2-3 mm) samples showed that the mechanical response of Ti_3SiC_2 is highly anisotropic and depends on grain orientation relative to the loading direction [17]. Favorably oriented microstructures exhibit high plasticity even at room temperature. The basal plane resolved shear stress was $\approx$ 32 MPa at room temperature and $\approx$ 22 MPa at 1300 ^{o}C. TEM study of the deformed samples [12, 27, 28] confirmed only the presence of basal plane dislocations. They are arranged in arrays or walls and their density increases during the deformation. A dislocation of about 10^{10} cm^2 is usually measured in areas containing dislocation walls and arrays [12].

More intensive and systematic research on mechanical properties of Ti_3SiC_2, as a function of temperature, strain rate and grain size has been performed recently. Tensile tests at different deformation rates and temperatures showed that the BTD transition depends not only on temperature but also on deformation rate [1]. The high strain rate sensitivity of $\approx$0.6 for the fine (3-5 μm) grained-structure is more in the range that is typical of superplastic materials, although Ti_3SiC_2 does not exhibit other attributes of superplasticity. The microstructural observations indicated that SiC inclusions ($\approx$10 μm) have an influence on the nucleation and accumulation of damage and that they could contribute to premature failure [1].

Tensile creep tests performed on coarse [3] and fine [2] grained microstructures, in the 1000-1200 ^{o}C temperature range and 10 to 100 MPa stress range, exhibit

primary, steady state and tertiary creep regimes. Analysis of the results showed that the same deformation mechanism(s) control the tensile creep over the entire range of testing temperature and stresses. In that range, the minimum creep rate can be represented by a power law equation with a stress exponent of 1.5 for the fine-grained structure and 2 for the coarse-grained one. For both microstructures the activation energy for creep was ≈450 kJ/mol. A weak grain size dependence of the minimum creep rate implied that diffusion creep and/or creep mechanisms based on grain boundary sliding cannot play a central role. Interrupted creep test showed that volume-conserving plastic deformation is the dominant source of strain during the secondary creep regime, while cavities and cracks are responsible for the acceleration of the creep rate during the tertiary creep. The results of strain transient dip tests suggested that large internal stresses are developed during creep and that these internal stresses result in recoverable (anelastic) strains during unloading.

The mechanical response of Ti_3SiC_2 is similar to that of hexagonal ice [29] in that both materials, if loaded rapidly are brittle, but if loaded slowly can be quite plastic. This stems from the fact that both are plastically very anisotropic; deformation occurs overwhelmingly by basal slip. In both cases, stress concentrations and the rate at which they can be relaxed dictate the nature of mechanical response. In the brittle regime, microcracks and their linkage play a dominant role in both cases.

The effect of temperature, grain size and strain rate on the mechanical response of Ti_3SiC_2 in tension is considered in this chapter. Tensile tests were carried out as a

function of cross head displacement (CHD) rates that ranged from 0.2 mm/min. to 0.01 mm/min. and temperature (25-1200 °C). The tests were carried out on both, fine (3-5 μm) and coarse (100-300 μm) grained microstructures. In contrast to our previous study on the tensile properties of the fine-grained, FG, structure [1] in which the strain was calculated from the CHD, the strains here were measured with higher accuracy using a capacitance extensometer. Whenever possible the results are compared with our previous work on the mechanical behavior of Ti_3SiC_2 in tension [1] and tensile creep [2, 3]

5.2 Experimental Procedure

The processing details can be found elsewhere [5]. The specimens were produced by reactive hot isostatic pressing (HIPing) of titanium (-325 mesh, 99.5 %, Alfa Aesar, Ward Hill, MA), silicon carbide (-400 mesh, 99.5 %, Atlantic Engineering Equipment, Bergenfield, NJ) and graphite (d_m=1μm, 99 %, Aldrich Chemicals, Milwaukee, WI) stoichiometric mixture. HIPing at 1450 °C under 40 MPa for 4 hrs resulted in a FG microstructure; HIPing at 1600 °C under 40 MPa fro 6 hrs results in a coarse-grained (100-300 μm) microstructure, further denoted by CG. Both, the FG and CG samples contained $\approx$ 2 vol. % SiC and TiC spherical inclusions that were homogeneously distributed and whose size did not exceed $\approx$ 2 μm in diameter.

A few CG samples containing large (≈10 μm) SiC inclusions (henceforth referred to as CG-CSiC) were also tested. Those samples were produced using the same procedure used to fabricate the CG samples. The starting powders were a coarser SiC (-325 mesh, 99.5 %, Atlantic Engineering Equipment, Bergenfield, NJ) and titanium-hydride (-325 mesh, 99.99 %, Timet, Henderson, AZ.) It is worth noting here that previously reported tensile test results [1] carried out on the FG structure contained coarse SiC inclusions. These samples will henceforth be referred to as FG-CSiC.

Tests were performed using dog-bone specimens SR51 with rectangular cross sections (2x2.5 mm) and a gauge length of 12 mm [52]. They were electro-discharge machined and tested with no further surface preparation. Tensile, stress relaxation and cycling loading-unloading tests were performed in air using a servo-electric Instron 8500 testing machine, supplied with a digital controller that allows tests to be run in strain or load control mode. In all tests, the load is applied on the sample via SiC pull-rods. A pin and clevis arrangement transfers the load from pull rod to specimen. Strains were measured by a capacitance high-temperature Instron extensometer. The extensometer was periodically calibrated during the testing. The accuracy of the strain measurements in loading and unloading was checked using a Si_3N_4 sample. The Young's modulus of Si_3N_4 obtained from the stress-strain curve was in good agreement with the expected one. The curves obtained during loading and unloading of Si_3N_4 did not exhibit any hysteresis loops.

The stress relaxation tests, SRT, involved sample loading in tension at 1200 °C and at a constant CHD rate (0.1 mm/min) up to the desired stress, at which time the crosshead motion was abruptly stopped. The stresses and strains were monitored during the relaxation tests as a function of time.

Cyclic loading-unloading, CLU, tests were carried out on FG samples at room temperature. Those tests involved cyclic loading up to a certain stress (stress amplitude) at a constant stress rate of 0.67 MPa/s, and unloading at the same rate. In order to maintain sample alignment, the minimum stress, $\sigma_{min,}$ in all cycles was 25 MPa. The CLU tests are performed to different levels of amplitude stress. The maximum amplitude stress was 260 MPa, i.e. $\approx$ 87 % of the fracture strength at room temperature. CLU tests were also carried out on both FG and CG microstructures at 1200 °C.

5.3 Results and Discussion

5.3.1 Tensile Tests

Select, but typical, engineering stress-strain curves carried out at a constant CHD in tension are shown in Fig. 48. All the curves in Fig. 48 are plotted on the same scale to make comparisons between them easier.

The first two sets of tensile tests, performed at a constant CHD rate of 0.1 mm/min. were carried out in order to explore the effect of temperature on both the FG (Fig. 48a) and CG (Fig. 48b) samples. The maximum stresses, σ_{max}, and strains to failure, ε_f, are plotted as a function of testing temperature in Figs. 49 and 50, respectively. From these results it is clear that:

i.   A BDT occurs in both microstructures at temperature of ≈ 1100 °C, as was previously well documented [6, 1, 51]. The BDT is accompanied by pronounced decrease in σ_{max} and a concomitant increase in ε_f.

ii.   The FG structure exhibits the higher σ_{max} over the entire range of testing temperatures. Furthermore, the FG structure is more "ductile" (ε_f is higher) than the CG at temperatures above the BDT. The differences in ε_f measured in the brittle mode can be attributed to the higher elastic strains in the FG (due to higher σ_{max}).

iii.   The samples containing the coarse SiC inclusions (FG-CSiC and CG-CSiC) are weaker than those containing the finer SiC inclusions, which confirms our previous assumption [1] that the SiC inclusions promote crack nucleation in the brittle mode. This difference in mechanical response, however, decreases as the testing temperature increases, presumably because the response at higher temperatures is more plastic.

It has to be emphasized that the results shown in Figs. 48a, 48b, 49 and 50 do not only reflect the influence of temperature. Since the machine and sample compliances (see Fig. 53.) change with testing temperature; i.e. performing the tests at a constant CHD rate do *not* mean that the strain rate is the same in all tests. The initial strain rate was estimated from the slope of the initial part of the strain (measured by extensometer) vs. time curves for all tests. The results show that the initial strain rate changes by a factor of ≈ 5 over the entire temperature range in both FC and CG samples.

The effect of the CHD rate on the stress-strain curves is shown in Figs. 48c and 48d for FG and CG samples at 1100 °C, respectively; the respective data at 1200 °C, are shown in Figs. 48e and 48f. In these figures the actual strain rate was calculated from the slope of tangent to the strain (measured by extensometer) vs. time curve at the point at which σ_{max} is reached during the tests (real strain rate is not constant during the tests, it increases as plastic deformation take place as expected). The effect of strain rate, $\dot{\varepsilon}$, and temperature, T, on σ_{max} and ε_f are plotted in Figs. 51 and 52 for the FG and CG samples, respectively. The results presented in Figs. 48c to 48f, 51 and 52, unequivocally demonstrate:

i. The mechanical response is a strong function of $\dot{\varepsilon}$; as $\dot{\varepsilon}$ decreases the samples become more plastic for a constant T.

ii. At low $\dot{\varepsilon}$ the stress reaches a plateau, after which it slowly decrease up to final fracture. Conversely, at high $\dot{\varepsilon}$ fracture occurs before the plateau stress

is reached. It follows that at high $\dot{\varepsilon}$ the stresses plotted in Fig. 51 are fracture stresses, while at low $\dot{\varepsilon}$ they are more representative of an ultimate tensile stresses or σ_{UTS}.

iii.   The $\dot{\varepsilon}$ at which the BDT occurs decreases as T increases. Also, the BDT is shifted towards lower $\dot{\varepsilon}$ for the CG samples.

The slopes of the initial parts of the tensile stress-strain curves (Fig. 48) are plotted in Fig. 53 as a function of T. The slope of $\approx$300 GPa measured at room temperature is in good agreement with the Young's modulus of 325 GPa reported in the literature [25, 56]. Up to 900 °C the decrease modulus is also in good agreement with the predicted one (solid line in Fig. 53) [56]. Above 900 °C, the measured modulus decreases sharply with temperature. This decrease in modulus is coupled with a large scatter in the measured values; a scatter that can be related to the: a) measurement error, since at high temperatures the extent of the initial part of the stress-strain curves is small, which makes it difficult to fit precisely; b) the slope of the initial part of stress-strain curves depends on strain rate and decreases with decreasing strain rate. Such behavior is typical of viscoelastic materials [57, 58]. Although the nature of this decrease is still not understood, it is clearly related to the BDT.

5.3.2 Stress Relaxation Tests

The SRT results for the CG and FG microstructures are shown in Fig. 54 and 55, respectively. The gray and black lines represent the measured strain and stress changes, respectively. These curves are unambiguous evidence for intense stress relaxation; after the instantaneous elastic shrinkage of the pull-rods, the samples (plastic) extend irreversibly. It is worth noting that these results were obtained from one sample for each microstructure, which implies that even after several SRT cycles the response remains qualitatively the same.

The instantaneous strain rate change during the relaxation tests were obtained by differentiation of the strain vs. time curves. Those values were then matched with the stress level monitored at the same time and plotted in Fig. 62.

5.3.3 Cycling Loading-unloading Tests at Room Temperature

Typical stress-strain curves measured in the CLU tests are shown in Figs. 56 and 57. These results clearly demonstrate that:

i.   The mechanical response carried out with decreasing (Fig. 56) and increasing (Fig. 57) amplitudes is linear elastic up to the ≈120 MPa. Below this stress the loading and unloading curves coincide.

ii.   Between 120 and 200 MPa, the hysteresis loops are closed, which implies the presence of an anelastic, recoverable deformation [57-61].

iii.   Above $\approx$200 MPa, the hysteresis loops are open suggesting that part of the deformation can be considered as plastic, i.e. irreversible.

iv.   It is not possible to measure any significant changes in the slope of the initial parts of the curves even after 26 cycles (Fig. 57).

v.   After 26 loading-unloading cycles, Fig. 57, the sample was loaded till failure at 250 MPa, which is lower than the average strength of $\approx$ 300 MPa measured at room temperature for this microstructure (Fig. 48a).

The area within each hysteresis loop, in each loading-unloading cycle, represents the amount of irreversible work, W_{irr}, associated with the anelastic and/or plastic deformations [59-61]. This work is plotted vs. stress bias (σ- σ_{min}, where σ_{min}= 25 MPa) in Fig. 58. The gray symbols represent W_{irr} as a function of ε_p, where ε_p is the difference between the elastic and measured strains at the maximum amplitude stress. These results suggest that:

i. W_{irr} measured in the CLU tests with increasing (closed symbols) and decreasing (open symbols) stress amplitudes are in good agreement with each other which in turn implies that sample misalignment can be ruled out as a source of the hysteresis loops. It follows that the anelastic behavior is an intrinsic material characteristic. The good reproducibility during increasing

and decreasing stress amplitudes is additional evidence for anelastic behavior [61].

ii.　W_{irr} can be fitted by the straight line up to ≈ 200 MPa (σ- $\sigma_{min} \approx 175$ MPa) and ε_p of $\approx 0.0075\%$. Such linear dependence is typical of anelastic, reversible deformation [59]. The W_{irr} vs. (σ- σ_{min}) curves intercept the x-axis at ≈ 88 MPa, i.e. at an amplitude stresses of 113 MPa. This is in good agreement with the observation that the first hysteresis loops occur at ≈ 120 MPa. Thus, this stress can be considered as the threshold for anelastic deformation.

iii.　The scatter in W_{irr} from different cycles carried out up to the same amplitude stress is low below $\sigma \approx 200$ MPa. This evidence once again confirms that closed hysteresis loops can be attributed to anelastic bahavior, which is in general independent on loading history.

iv.　Once the open loops are formed above $\varepsilon_p = 0.0075\%$, W_{irr} increases nonlinearly. The hysteresis loops become open suggesting that part of the deformation can be considered as plastic. Furthermore, the differences between the results obtained from the increasing and decreasing amplitude stresses becomes evident. This difference can be explained by a dependence of the plastic deformation on the state of the sample, i.e. on previous loading history [59].

v.　W_{irr} decreases during successive loading-unloading tests carried out up to the same amplitude stress (first three cycles in Fig. 56 and last two cycles in Fig. 57). This decreases in W_{irr} is followed by a decrease in ε_p, and thus the results

in W_{irr} vs. ε_p plot do not exhibit much scatter. Such behavior is usually referred to as cyclic hardening [58].

Several different mechanisms are usually invoked to explain anelastic (viscoelastic) strains [36]. In all cases, for dissipation of energy to occur a friction mechanism must exist. Although, more work is needed in order to understand the source of anelastic, recoverable strain in Ti_3SiC_2, here author can speculate that viscous glide of dislocations into the pileups during loading and their run back during unloading is a the likely mechanism. This is not surprising, since the glide of basal planed dislocations and the formation of pile-ups and dislocation arrays is well documented in Ti_3SiC_2, even at room temperature [11].

The source of the plastic, irreversible deformation observed in the CLU tests is unclear at this time. On one hand, the cycling hardening and the unchanged modulus suggest that the irreversible deformation can be attributed to volume-conserving plastic deformation. On the other hand, the decrease in fracture stress upon cycling loading and lack of the 5 independent slip systems, suggest that the irreversible strain can be attributed microcrack formation. The answer is probably a combination of both.

5.3.4 Cycling loading-unloading Tests at 1200 °C

The stress-strain curves obtained at 1200 °C for the FG and CG microstructures are shown in Figs. 59a and 59b, respectively. Typical stress and strain changes during one loading-unloading cycle are shown in Fig. 60. W_{irr} is plotted in the function of ε_p (dashed curves) and σ-σ_{min} (solid curves) for FG (black symbols) and CG (gray symbols) samples in Fig. 61. Those results show that:

i.   Hysteresis loops at stresses above ≈ 20 MPa are open for both microstructures (Figs. 59a and 59b), indicating that at 1200 °C, reversible plastic deformation occurs at stresses as low as ≈20-30 MPa.

ii. The samples elongate even upon unloading up to certain stress level, after which they shrink (Fig. 59). This response, clearly observable in Fig. 60, is usually referred to as viscoplastic [58].

iii. Part of the strain is recoverable even after complete unloading (Fig. 60). Such behavior is in good agreement with the anelastic strain recovery observed in the strain-transient dip, STD, tests [2, 3].

iv. Above 20 MPa, where the deformation can be considered plastic, W_{irr} is higher for the CG microstructure, than for the FG (Fig. 61). At the same time, ε_p is smaller in the CG than in the FG samples. The full implications of these observations are not clear at this time.

v.   The W_{irr} increases with successive loadings to the same amplitude stress. This is followed by an increase in ε_p and a decrease in the load at which the onset on non-linearity in the stress-strain curve is observed (last four cycles in Fig 59a). Such behavior is usually referred to as cycling softening.

The clear evidence for viscoplastic deformation obtained in the CLU tests at 1200 °C is of the great importance for better understanding of the mechanical response of Ti_3SiC_2. Viscoplastic behavior is usually related to a time dependent response in the material [58], which is in total accord with the high strain rate sensitivity previously reported [1]. Also, the results from the stress relaxation and strain transient dip tests [2, 3] are in good agreement with rheological models of viscoplastic materials. Total strain in viscoplastic deformation can be additively decomposed into elastic, anelastic (viscous) and plastic parts. It is hereby acknowledged that the atomistic nature of the plastic and anelastic parts of the deformation are not clear at this time. More work is needed to better understand these mechanisms.

5.4 Summary and Conclusions

The results of the tensile tests at constant CHD rate, relaxation, cycling loading-unloading, creep [2, 3] and strain transient creep tests clearly demonstrate

that the tensile response of Ti_3SiC_2 strongly depends on strain rate, temperature and grain size. Results from all tests carried out at 1100 °C and 1200 °C are summarized in Fig. 62. These results clearly demonstrate that the BTD transition is a function of temperature and strain rate. At high strain rates and lower temperatures the stress is almost insensitive to strain rate (especially in the case of the CG samples). Conversely, at low strain rates and high temperatures Ti_3SiC_2 exhibits a high strain rate sensitivity. Thus, the mechanical response can be divided in three regimes:

1.   Brittle regime- represented by dotted and dashed lines in Fig. 62 - at low temperatures and high strain rates. In this regime the deformation is elastic and anelastic in nature. Upon loading, samples first deform elastically up to certain stress level above which anelastic deformation takes place. This anelastic deformation can be related to the easy glide of basal plan dislocations into pileups, and their runback during unloading. Dislocation pileups form in the favorably oriented grains (in which the critical resolved shear stress is reached). Since Ti_3SiC_2 does not posses five independent slip systems, deformation of the grains in which glide occurs cannot be compensated by the deformation of adjacent grains. Thus, the large internal stresses are generated that ultimately lead to brittle catastrophic failure.

2.   Ductile regime – represented by solid and dashed lines in Fig. 62- at high temperatures and low strain rates. The result from the SRT, STD creep and tensile tests at low strain rates are in good agreement with each other suggesting

that the same atomistic mechanisms are operative in all tests. In this region the mechanical response of Ti_3SiC_2 exhibit all the attributes usually related to viscoplastic deformation; the creep curves exhibit transients and steady state creep regimes [2, 3], substantial stress relaxation takes place, strain rate sensitivity is high (0.5-0.6), samples continue to elongate upon unloading in the CLU tests, anelastic strain recovery takes place upon unloading below the internal stresses in STD tests, etc. All those results clearly demonstrate that some mechanism, responsible for the relaxation of the internal stresses, has to be activated at higher temperatures and low strain rates the nature of which is not well understood at this time.

3.   <u>Transition regime</u> - at intermediate temperatures and strain rates. This regime can be related to the tensile tests at which relatively high strains are obtained followed by a pronounced nonlinear part in the stress strain curves, but at which the failure still occurs before the maximum or plateau stress is reached. The transition behavior can also be observed in creep tests at high stresses [2, 3], in which the tertiary creep onsets before steady state creep has been established. In this regime, the mechanical response of the material is controlled by simultaneous damage formation (microcracking) and localized plastic deformation.

The results presented in this chapter and in our previous studies on the mechanical behavior of Ti_3SiC_2 clearly demonstrate that its mechanical response is

strong function of temperature, strain rate and grain size. At low temperatures and high strain rates the response can be categorized as a brittle. In that regime Ti_3SiC_2 does not exhibit linear elastic behavior even at room temperature. The presence of hystersis loops in cyclic loading-unloading provides unambiguous evidence for anelastic behavior. At higher temperatures, intense stress relaxation is evident, and the mechanical response can be considered viscoplastic. The evidence of viscoplastic behavior can be found in the cyclic loading-unloading tests, creep and strain transient creep tests.

List of References

1. Radovic M, Barsoum MW, El-Raghy T, Seidensticker J, Wiederhorn s. Tensile properties of Ti_3SiC_2 in the 25-1300 °C temperature range. Acta Mater. 2000;48:453-59.

2. Radovic M, Barsoum MW, El-Raghy T, Wiederhorn S. Tensile creep of fine grained (3-5 μm) Ti_3SiC_2 in the 1000-1200 °C temperature range. Acta Mater. 2001; in press.

3. Radovic M, Barsoum MW, El-Raghy T, Wiederhorn S. Tensile creep of coarse grained (100-300 μm) Ti_3SiC_2 in the 1000-1200 °C temperature range. Acta Mater.; submitted for publishing.

4. Radovic M, Barsoum MW, El-Raghy T, Wiederhorn S, Luecke WE. Effect of temperature, strain rate and grain size on mechanical response of Ti_3SiC_2 in tension. Acta Mater.; submitted for publishing.

5. El-Raghy T, Barsoum MW. Processing and mechanical properties of Ti_3SiC_2, Part I: Reaction path and microstructure evaluation. J. Am. Ceram. Soc. 1999;82: 2849-55.

6. El-Raghy T, Barsoum MW, Zavaliangos A, Kalidindi SR. Processing and mechanical properties of Ti_3SiC_2, Part II: Effect of grain size and deformation on temperature. J. Am. Ceram. Soc. 1999;82: 2855-62.

7. Barsoum MW, El-Raghy T. Synthesis and characterization of remarkable ceramic: Ti_3SiC_2. J. Am. Ceram. Soc. 1996;79:1953-56.

8. Barsoum MW, El-Raghy T. A progress report on Ti_3SiC_2, Ti_3GeC_2 and H-phases, M_2BX", J. Mater. Synth. Process. 1997;5:197-216.

9. Barsoum MW, El-Raghy T, Ogbuji L. Oxidation of Ti_3SiC_2 in air. J. Electrochem. Soc. 1997;144:2508-16.

10. El-Raghy T, Zavaliangos A, Barsoum MW, Kalidindi SR. Damage mechanism around hardness indentation in Ti_3SiC_2. J. Am. Ceram. Soc. 1997;80:513-16.

11. Barsoum MW, El-Raghy T. Room temperature ductile carbides. Metall. Mater. Trans. 1999;30A:363-69.

12. Barsoum MW, Faber L, El-Raghy T. Dislocation, kink bands and room temperature plasticity of Ti_3SiC_2", Metall. Mater. Trans. 1999;30A:1727-32.

13. Finkel P, Barsoum MW, El-Raghy T. Low temperature dependence of elastic properties of Ti_3SiC_2. J. Appl. Phys. 1999;85:7123-29.

14. Jeitschko W, Nowotny H. Die kristallstructur von Ti_3SiC_2 – Ein neuer komplxcarbid-typ", Monatasch fur Chem. 1967;98:329-37.

15. French D, Wiederhorn SM. Tensile specimens for ceramic componenets. J. Am. Ceram. Soc. 1996;79:550-52.

16. Courtney TH. Mechanical behavior of materials. McGraw-Hill, New York 1990.

17. Wagoner RH, Chenot JL. Fundamentals of metal forming. John Wiley and Sons Inc., New York 1997.

18. Poirier JP. Creep of crystals. Cambridge University Press, Cambridge 1985.

19. Chokshi AH, Mukherjee AK, Langdon TG. Superplasticity in advanced materials. Mater. Sci. and Engng. 1993;R10:237-69.

20. Langdon TG. Superplastic ceramics - An overview. Superplasticity in Aerospace II, Edited by McNelly TR and Heikkenen HC, The Minerals, Metals and Materials Society 1990.

21. Wakai F, Kodoma Y, Nagano T. Superplasticity of ZrO_2 polycrystals. Japan. J. Appl. Phys. 1989;2:57-68.

22. Xue LA, Chen IW. Superplastic alumina at temperatures below 1300 °C using charge-compensating dopants", J. Am. Ceram. Soc. 1996;79:233-38.

23. Nieh TG, McNally CM, Wadsworth J. Superplastic properties of a fine grained yttria-stabilized tetragonal polycrystal of Zirconia, Scripta Metall. 1988;22:1297-1300.

24. Wiederhorn SM, Luecke WE. Creep of silicon nitride, Computer-aided design of high-temperature materials, Edited by Pechenik A, Kalia RK, Vashishta P, Oxford University Press, Oxford 1998.

25. Barsoum MW. The $M_{N+1}AX_N$ phases: A new class of solids: Thermodynamically stable nanolaminates. Prog. Solid State Chem. 2000;28:201-81.

26. Pampuch R, Lis J, Stobierski L, Tymkiewicz M. Solid combustion synthesis of Ti_3SiC_2", J. Eur. Ceram. Soc.1989;5;283-91.

27. Farber L, Barsoum MW, Zavaliangos A, El-Raghy T. Dislocations and stacking faults in Ti_3SiC_2. J. Am. Ceram. Soc. 1998;8: 1677-81.

28. Farber L, Levin I, Barsoum MW. HRTEM study of a low angle boundary in plastically deformed Ti_3SiC_2. Phil. Mag. Lett. 1999;79:163-69.

29. Barsoum MW, Radovic M, Finkel P, El-Raghy T. Ti_3SiC_2 and Ice Appl. Phy, Lett. 2001;in press.

30. Carroll DF, Wiederhorn SM, Roberts DE. Technique for tensile creep tesing of ceramics. J. Am. Ceram. Soc. 1989;72:1610-24.

31. Luecke WE, French JD. Sources of strain measurement error in flag-based extensometry. J. Am. Ceram. Soc. 1996;79:1617-26.

32. Lloyd GJ, McElroy RJ. A model for quantitative interpretation of high-temperature stress relaxation phenomena: The effect of anelasticity. Phil. Mag. 1975;32:231-44.

33. Ahlquist CN, Nix WD. The measurement of internal stress during creep of Al and Al-Mg alloys. Acta Metall. 1971;19:373-85.

34. Lloyd GJ, McElroy RJ. On Aanelastic contribution to creep. Acta Metall. 1974;22:339-48.

35. Parker JD, Wilshire B. Rate-controling processes during creep of super-purity Al. Phil. Mag. A 1980;41:665-80.

36. Poirier JP. Microscopic creep models and the interpretation of stress-drop tests during creep. Acta Metall 1977;25:913-17.

37. Takeuchi S, Argon AS. Steady-state creep of single-phase crystalline matter at high temperature. J. Mat. Sci. 1976;11:1542-66.

38. Frost HJ, Ashby MF. Deformation-mechanism maps. Pergamon Press, London 1982.

39. Monkman FC, Grant NJ. An empirical relationship between rupture life and minimum creep rate in creep-rupture tests. Proc. Am. Soc. Test. Mater. 1956;56: 593-620.

40. Nabarro FRN. Deformation of crystals by the motion of single ions. Report of a Conference on Strength of Solids - Bristol, The Physical Soc. 1948:75-90.

41. Coble RL. A model for boundary diffusion controlled creep in ceramic materials. J. Appl. Phys.1963;34:1679-82.

42. Wakai F. Step model of solution-precipitation creep. Acta. Metall. Mater. 1994;42:1163-72.

43. Raj R, Chyumg CK. Solution-precipitation creep in glass-ceramics. Acta Metall. 1981;29:159-66.

44. Jimenez-Melendo M, Dominguez-Rodriguez A, Bravo-Leon A. Superplastic flow fine grained yttria-stabilized zirconia polycrystals: Constitutive equation and deformation mechanism. J. Am. Ceram. Soc. 1998;81:2761-76.

45. Hutchinson JW. Bounds and self-consistent estimates for creep of polycrystalline materials. Proc. R. Soc. Lond. A 1976;348:101-27.

46. Hutchinson JW. Creep and plasticity of hexagonal polycrystals as related to single crystal slip. Metal. Trans. A 1977;8A:1465-69.

47. Duval P, Ashby MF, Anderman I. Rate controlling processes in creep of polycrystalline ice. J. Phys. Chem. 1983;8:4066-74.

48. Gilbert CJ, Boyer DR, Barsoum MW, El-Raghy T, Tomsia AP, Ritchie RO. Fatique-crack growth and fracture properties of coarse and fine-grained Ti_3SiC_2. Scripta Mater. 2000;42:761-67.

49. Wiederhorn SM, Hockey BJ, Chung TJ. Creep and creep rupture of structural seramics. Toughening mechanism in quasi-brittle materials, edited by Shah SP, Kluwer Academics Publisher, Amsterdam 1991:555-76.

50. Shirato K, Chen D, Barsoum BW, El-Raghy T. Ritchie RO. High-temperature cyclic fatigue-crack growth in monolithic Ti_3SiC_2 ceramics. submitted for publishing.

51. Li JF, Pan F, Sato f, Watanabe R. Mechanical properties of polycrystalline Ti_3SiC_2 at ambient and elevated temperatures. Acta Mat. 2001;49:937-348.

52. French JD, Wiederhorn SM. Tensile specimen for ceramic components. J. Am. Ceram. Soc. 1996;79:550-52.

53. Langdon TG. A unified approach to grain boundary sliding in creep and superpalsticity. Acta Metall. Mater. 1994;42:2437-43.

54. Mukherjee AK. Rate controlling mechanism in superplasticity. Mate. Sci. eng 1971;8:83-9.

55. Lueske WE, Wiederhorn SM. A new model for tensile creep of silicon nitride. J. Am. Ceram. Soc 1999;82:2769-78.

56. Finkel P, Barsoum MW, El-Raghy T. Low temperature dependencies of the elastic Properties of $Ti_3Al_{1.1}C_{1.8}$, Ti_4AlN_3 and Ti_3SiC_2 . J. Appl. Phys. 2000;87;1701-3.

57. Dowling NE. Mechanical behavior of metals. 2nd edition, Prentice Hall, Upper Saddle River NJ 1998.

58. Skrzypel JJ, Hetnarski RB. Plasticity and creep: Theory, examples, and problems, CRC Press, Boca Raton FL, 2000.

59. Roberts JM, Brown N. Microstrain in zinc single crystal. Trans. of AIME 1960;218: 456-63.

60. Brown N. Ekvall RA. Temperature dependence of the yield points in iron. Acta. Metall. 1962;10:1101-07.

61. Roberts JM, Brown N. Low frequency friction in zinc single crystals, Acta. Metall. 1962;10:430-41.

Appendix A
Tables

Table 1. Contribution of microcracks and cavities to the overall measured strain at failure for fine grained structure.

Testing temperature, °C	Testing stress, MPa	Time to failure, h	Measured strain to failure, %	Strain due to voids and microcracks, (Quant. OM), %	Fraction of the strain from cavities and cracks
1000	60	81	1.7	1.2±0.17	0.70±0.10
1050	60	32.6	2.3	1.8±0.5	0.80±0.20
1000	40	373	4.7	3.1±0.8	0.65±0.15
1200	20	5.16	6.8	4.2±1.3	0.60±0.20
1200	10	26	8.5	4.4±1.1	0.70±0.10
1100	20	70	8.6	4.4±1.1	0.50±0.15

Table 2. Effect of grain size on minimum strain rate. FG-fine grained structure [2]; CG – coarse grained structure.

Stress, MPa	Temperature, °C	$\dfrac{(\dot{\varepsilon}_{min})_{FG}}{(\dot{\varepsilon}_{min})_{CG}}$	Grain size exponent, p	Temperature, °C	$\dfrac{(\dot{\varepsilon}_{min})_{FG}}{(\dot{\varepsilon}_{min})_{CG}}$	Grain size exponent, p
10		-	-		5.3	0.49
20	1000	4.1	0.41	1200	3.8	0.39
40		2.8	0.30		2.6	0.28
100		1.8	0.17		-	-

Table 3. Contribution of damages to the overall measured strain for coarse grained structure

Testing temperature, °C	Testing stress, MPa	Time to failure, h	Measured strain to failure, %	Strain due to voids and microcracks, (Quant. OMI), %	Fraction of the strain from cavities and cracks
1000	100	44.5	0.89	0.51±0.16	0.57±0.18
1000	60	230	5.60	3.65 ±1.26	0.65±0.22
1050*	60	aborted after 21	0.78	0.22±0.15	0.28±0.19
1050*	60	aborted after 49	1.81	0.54±0.22	0.30±0.12
1050*	60	94.5	3.63	1.45 ±0.55	0.40±0.15
1050	40	252	7.30	2.42 ±0.82	0.33 ±0.11
1100	80	9.4	2.00	0.41±0.27	0.21±0.13
1100	40	20.3	3.90	2.07 ±0.40	0.53 ±0.10
1200	40	0.91	2.20	1.11±0.24	0.50±0.11
1200	20	32.9	5.80	4.26±0.67	0.73±0.11

* creep curves of those specimens are presented in Fig 46

Appendix B

Figures
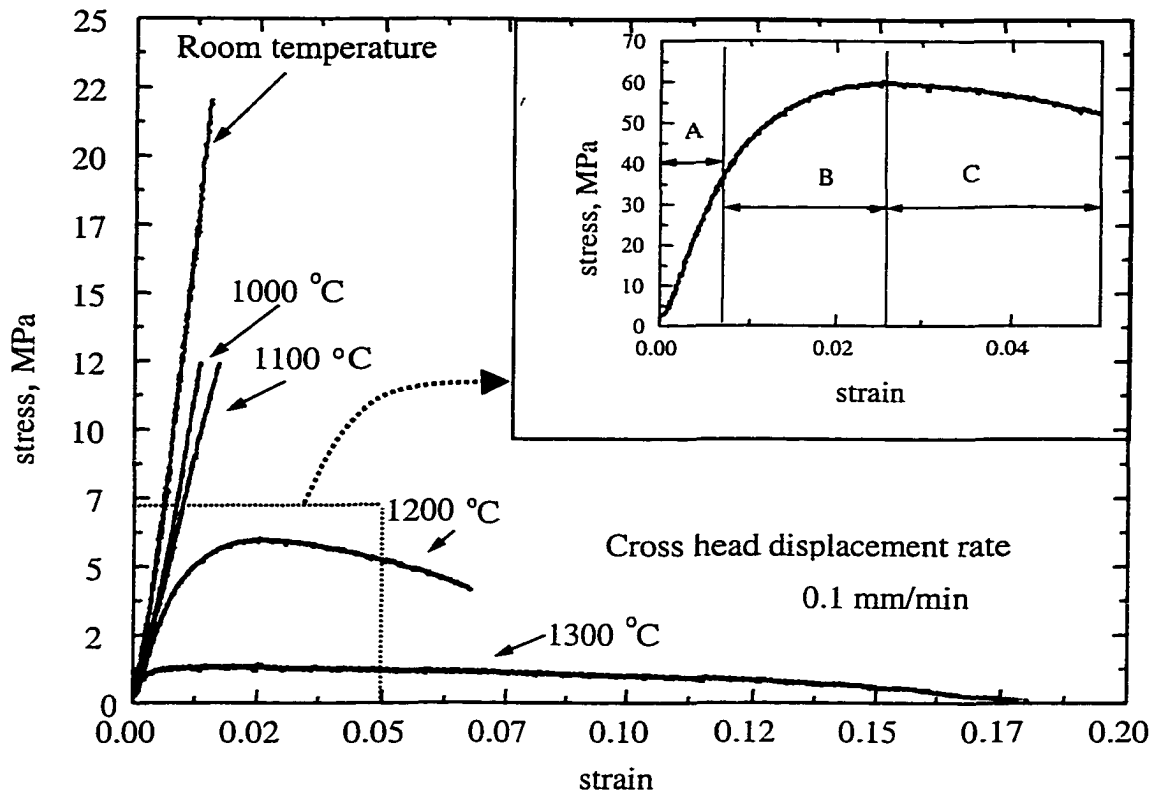
Fig 1. Typical engineering stress-strain curves of fine-grained Ti_3SiC_2 samples using cross head displacement rate of 0.1 mm/min. Inset is magnification of boxed area in right bottom corner. Three stages are discernible: elastic (A), a transient apparent "hardening" (B) and softening (C).
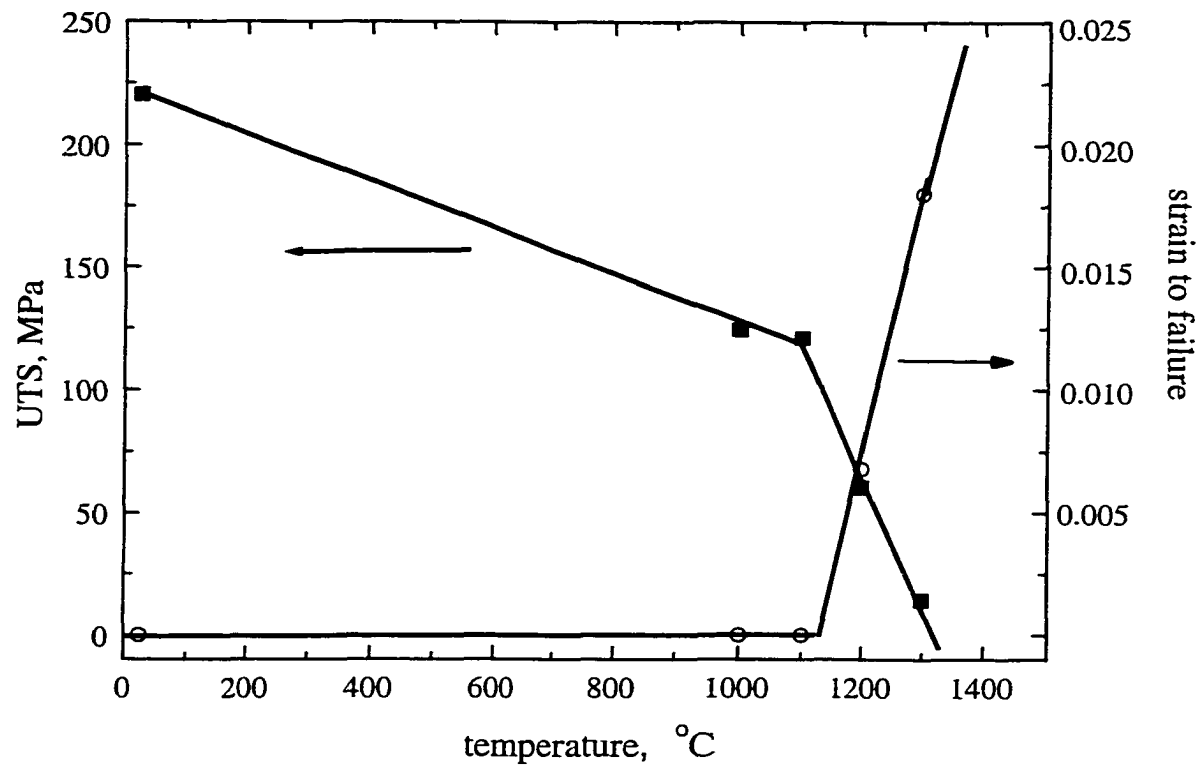
Fig. 2. The effect of temperature on strength (UTS) and strain to failure.
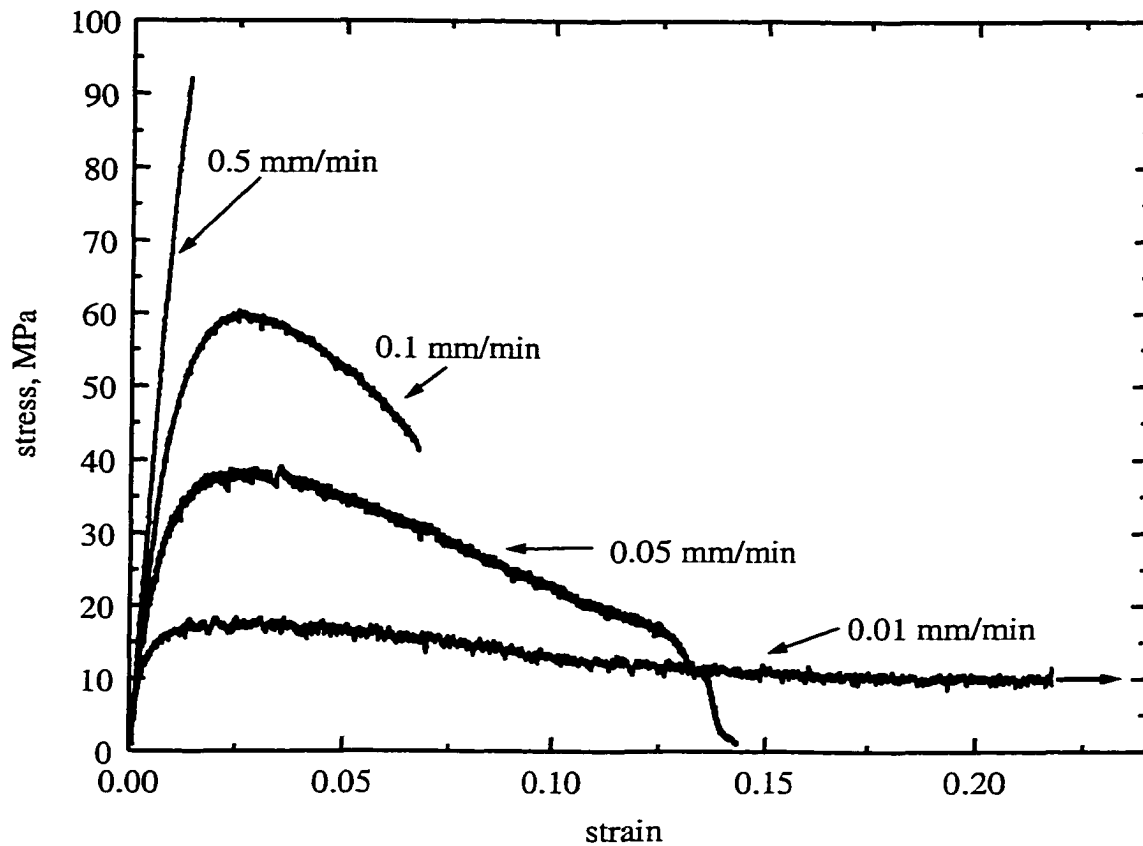
Fig.3. Effect of strain rates on engineering stress-strain curves tested in tension at 1200 °C. Short horizontal arrows denote deviation from linearity or "yield" points.
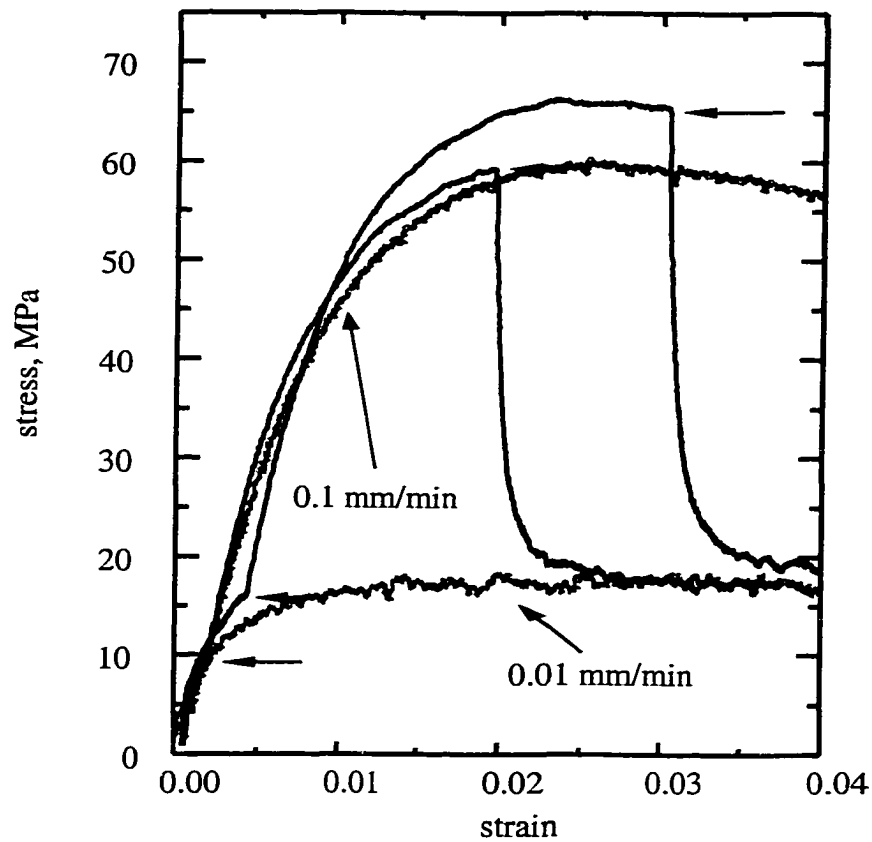
Fig. 4. Strain rate tensile tests for: a) strain-rate jump and drop tests. The cross head displacement rate was increased from 0.01 mm/min to 0.1 mm/min and dropped back again. Horizontal arrows point to stress at which the cross head displacement increased and decreased. Gray thick lines are results of tensile tests at constant cross head displacement rate.
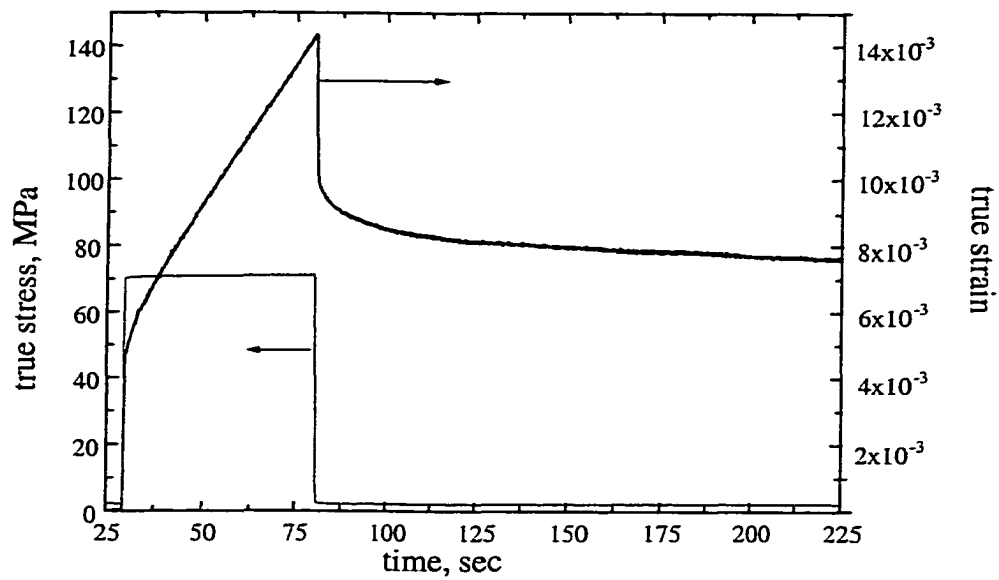
Fig. 5. Creep test at 1200 °C and 70 MPa. The left axis represents the true stress and the right axis the true strain
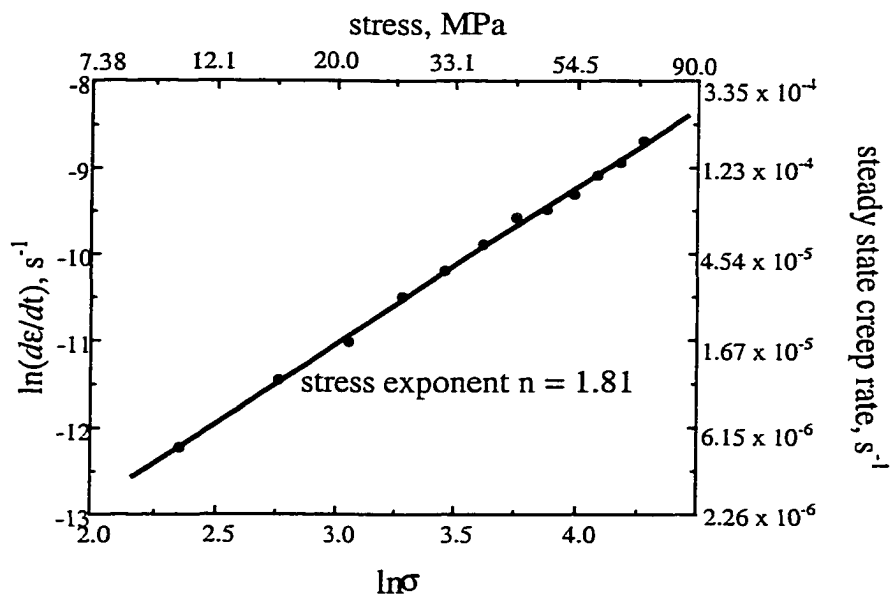
Fig. 6. The log-log plot of steady state creep rate vs. flow stress obtained from data shown in Fig. 5.
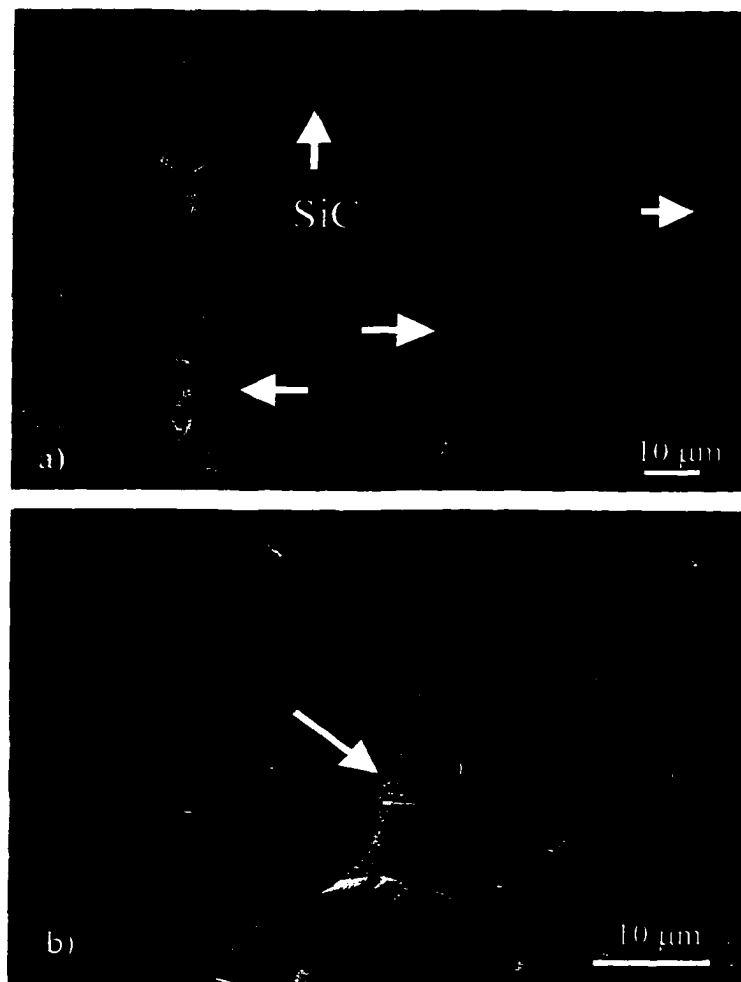
Fig. 7. SEM of fracture surface of fine grained Ti₃SiC₂. a) Specimen tested at room temperature. Horizontal arrows denote location of microcracks, while vertical arrows denote SiC inclusions. b) Specimen tested at 1300°C using a cross head displacement rate of 0.1 mm/min. Arrows points to location of transgranular fracture. Applied load is in vertical direction.
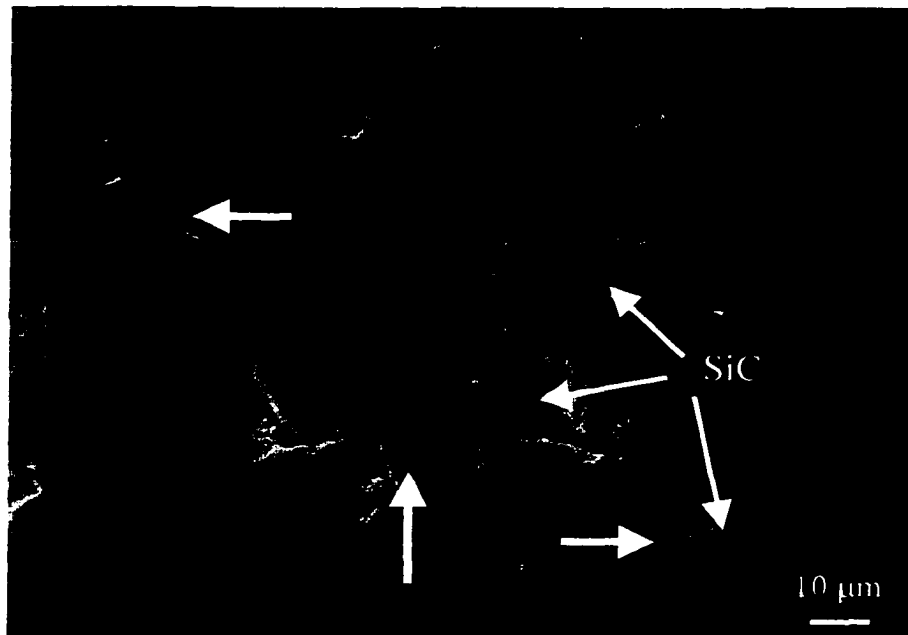
Fig. 8. SEM micrograph of sample tested at room temperature and a cross head displacement rate of 0.1 mm/min adjacent to the fracture plane. Applied load is in vertical direction. Microcracks (denoted by vertical arrows) are parallel to the fracture surface that is at the top of the micrograph and out of the field of view. Horizontal arrows point to microcracks at $\approx 45°$ to the fracture plane. Remaining arrows point to the SiC inclusions.

a)   b)
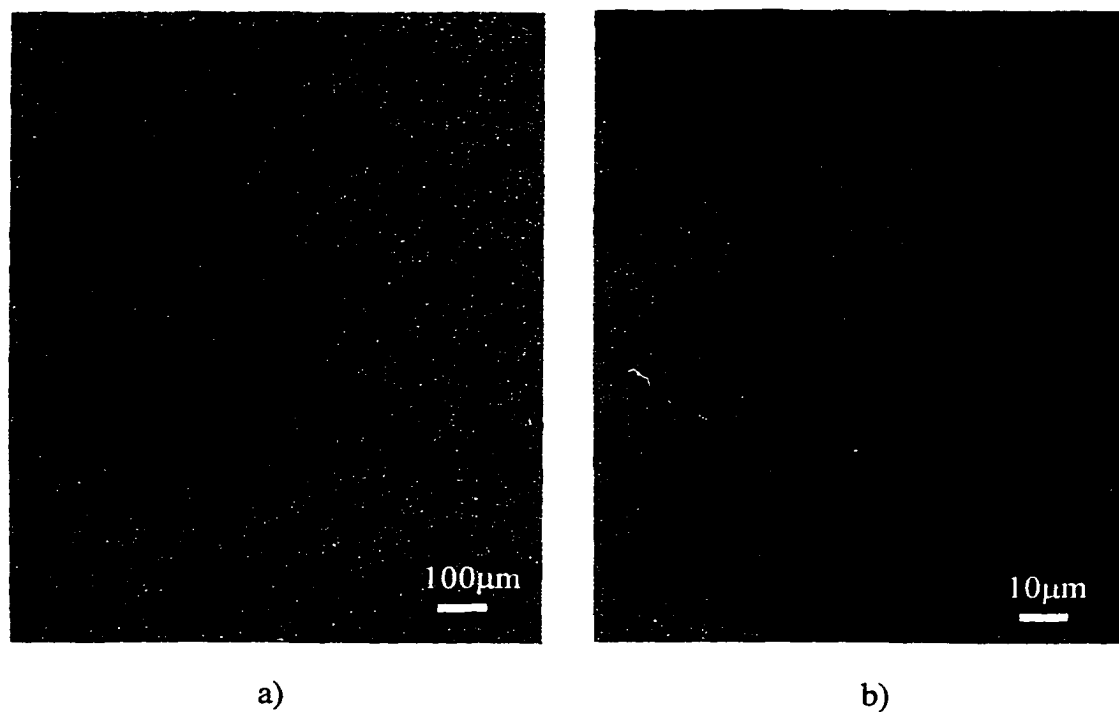
Fig. 9.   Optical micrographs of surface perpendicular to fracture surface of material

tested at 1300°C and a cross head displacement rate of 0.1 mm/min. a)

Lower magnification showing cavities and microcracks extending almost

from one side of the sample to other. b) Higher magnification showing

microcracks joining SiC inclusions. Applied load is in vertical direction.
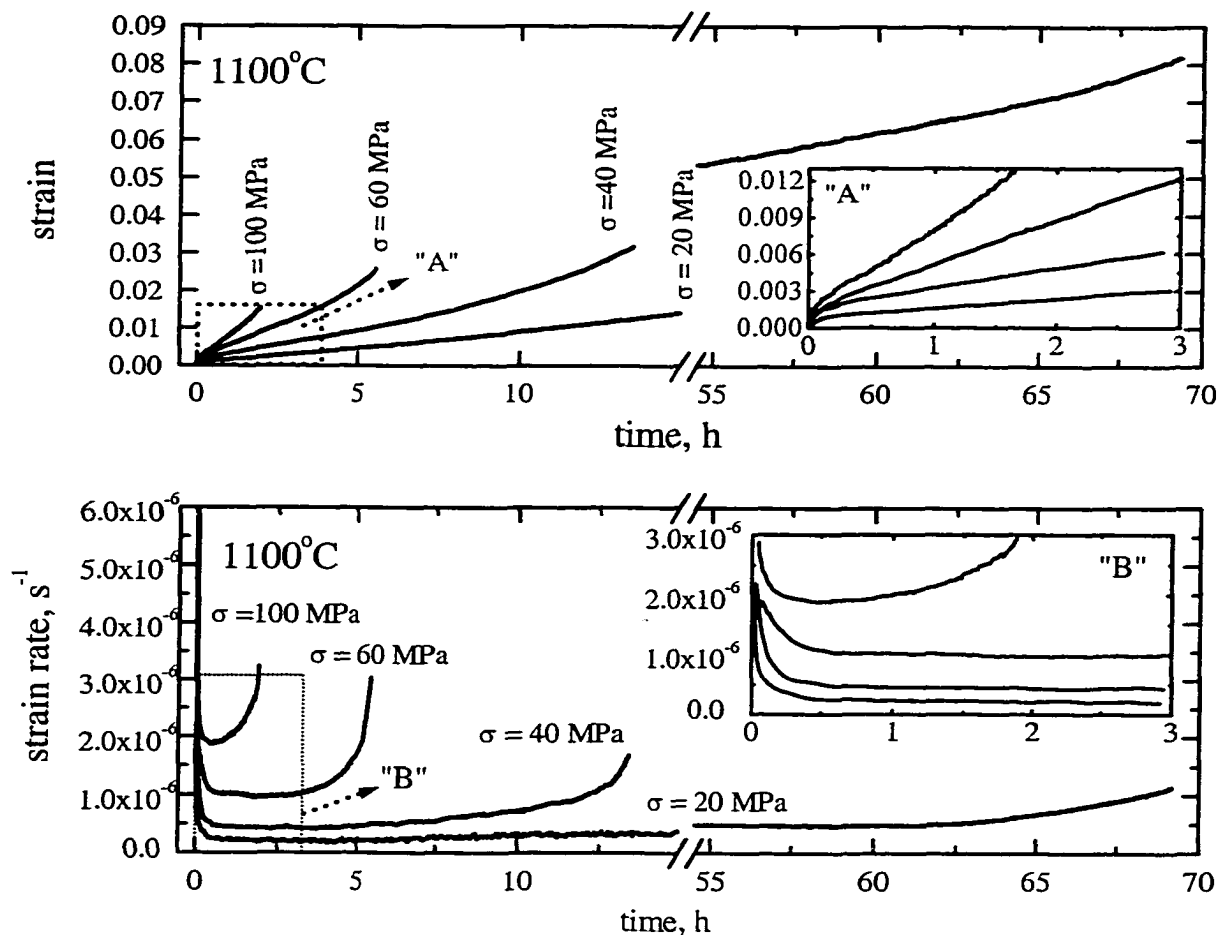
Fig. 10. Time dependence of a) tensile strain and b) strain rate of Ti_3SiC_2 samples tested at 1100 °C subjected to loads corresponding to stresses of 20, 40, 60 and 100 MPa. Strain rate vs. time plot (b) is obtained by differentiation of strain-time curves (a). Inserts "A" and "B" are enlargements of the initial parts of the plots shown in a and b.
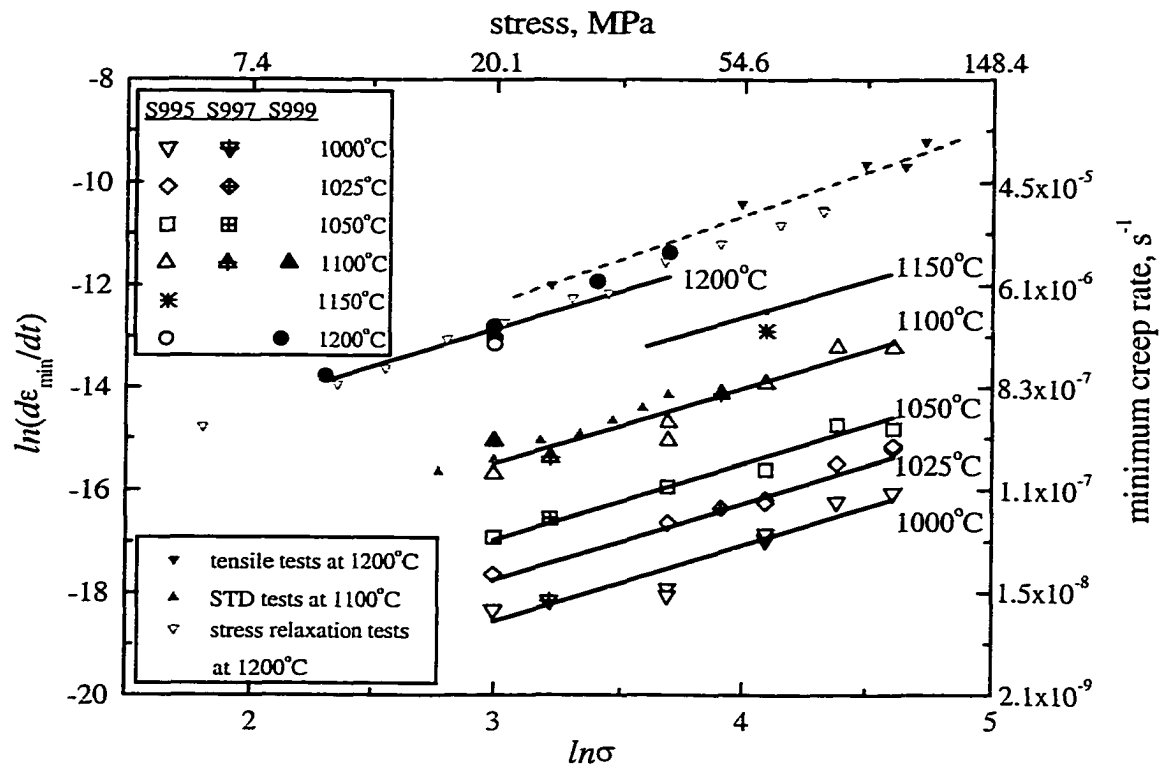
Fig. 11. Ln-ln plot of $\dot{\varepsilon}_{min}$, vs. stress, σ as a function of temperature. The black open, close and hatched symbols represent data from creep tests carried out on all three series of samples. The straight lines represents results of a bilinear regression of $\dot{\varepsilon}_{min}$ as a function of σ and temperatures. Closed gray down-triangles in represent the maximum (plateau) σ as a function of strain rate obtained from tensile tests at 1200 °C [4]. Dashed gray line represent the least squares fit of these results. Open gray down triangles represents results obtained from stress relaxation tests [4]. Closed gray up-triangles are the data obtained from STD tests at 1100 °C (see Fig. 14).
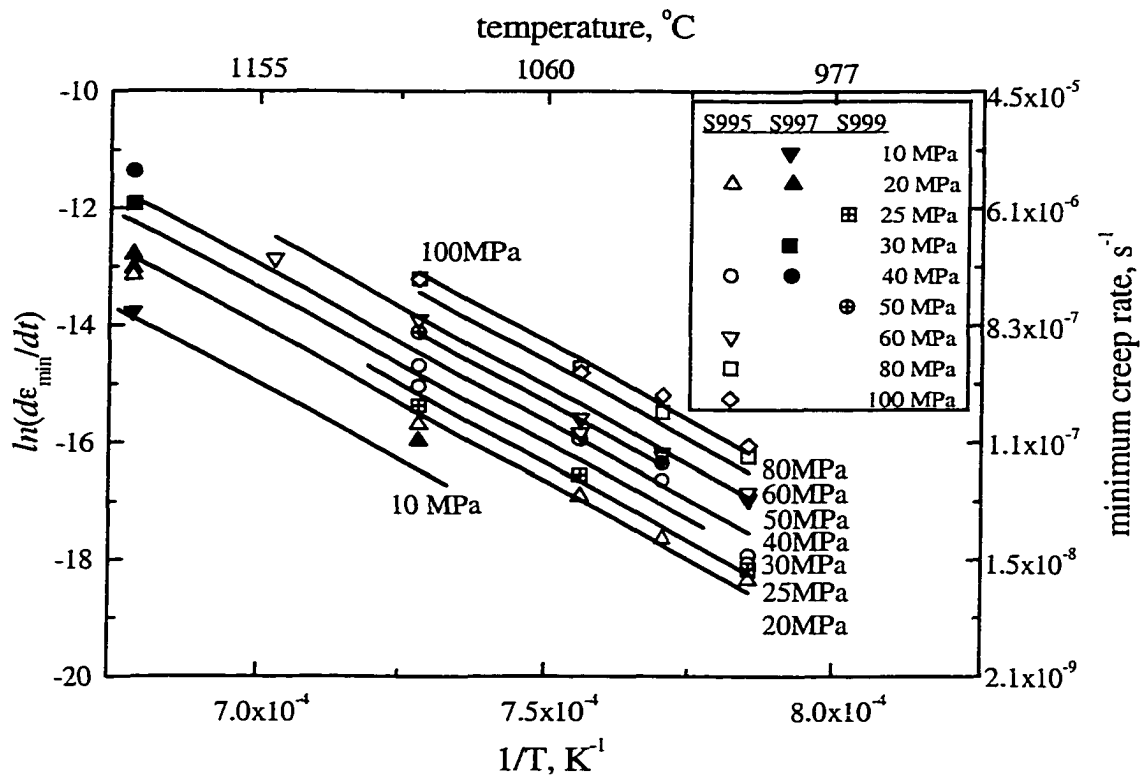
Fig. 12. Arrhenius plot of minimum creep rate, $\dot{\varepsilon}_{min}$, as a function of σ. The black open, close and hatched symbols represent data from creep tests carried out on all three series of samples. The straight lines on all curves represents results of a bilinear regression of $\dot{\varepsilon}_{min}$ as a function of σ and temperatures
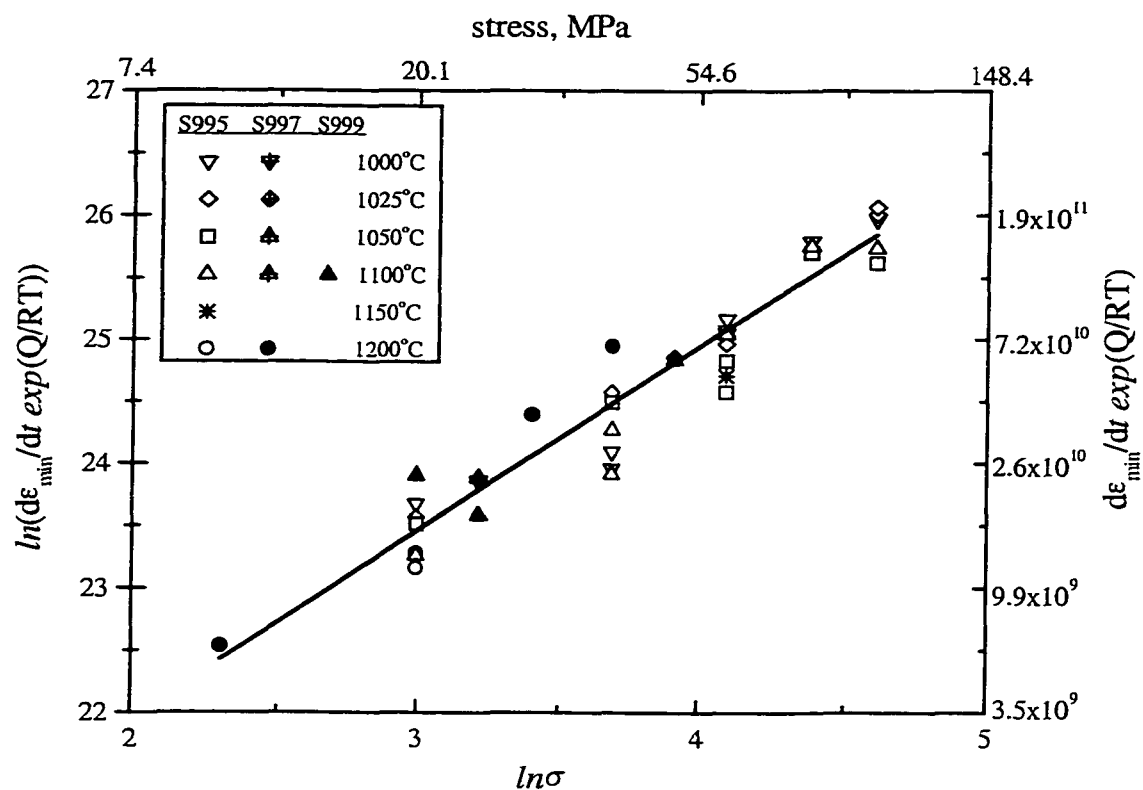
Fig.13. Ln-ln plot of $\dot{\varepsilon}_{min} \bullet \exp(Q/kT)$ vs. σ for Q of 445 kJ/mol. The black open, close and hatched symbols represent data from creep tests carried out on all three series of samples. The straight line represents results of a bilinear regression.
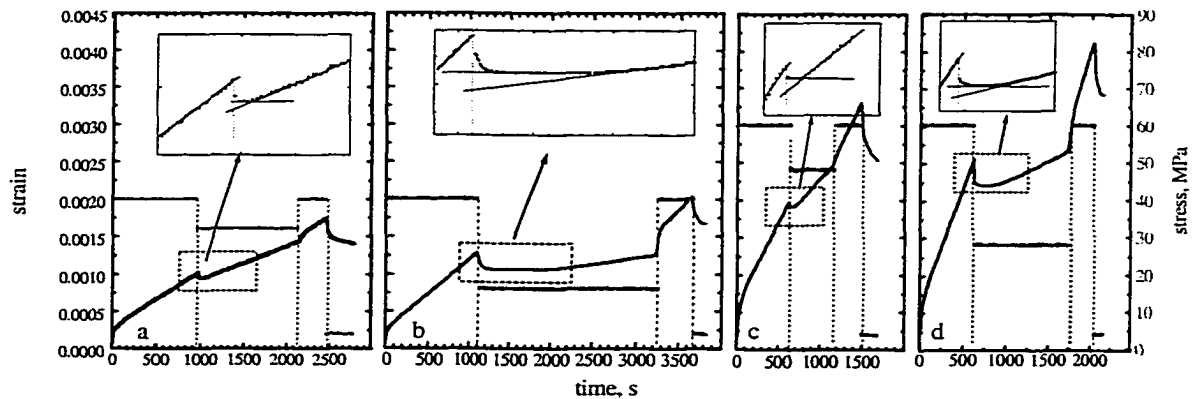
Fig. 14. Results of STD tests at 1100 °C. The black solid lines represents the measured strain as a function of time, while gray solid lines are stress changes during the time. In all tests initial stress σ was reduced by $\Delta\sigma$ and then increased again up to σ. At the end of the all tests samples were unloaded down to 4 MPa. (a) σ=40 MPa, $\Delta\sigma$= 8 MPa; (b) σ=40 MPa, $\Delta\sigma$= 24 MPa; (c) σ=60 MPa, $\Delta\sigma$= 12 MPa; (a) σ=60 MPa, $\Delta\sigma$= 32 MPa.
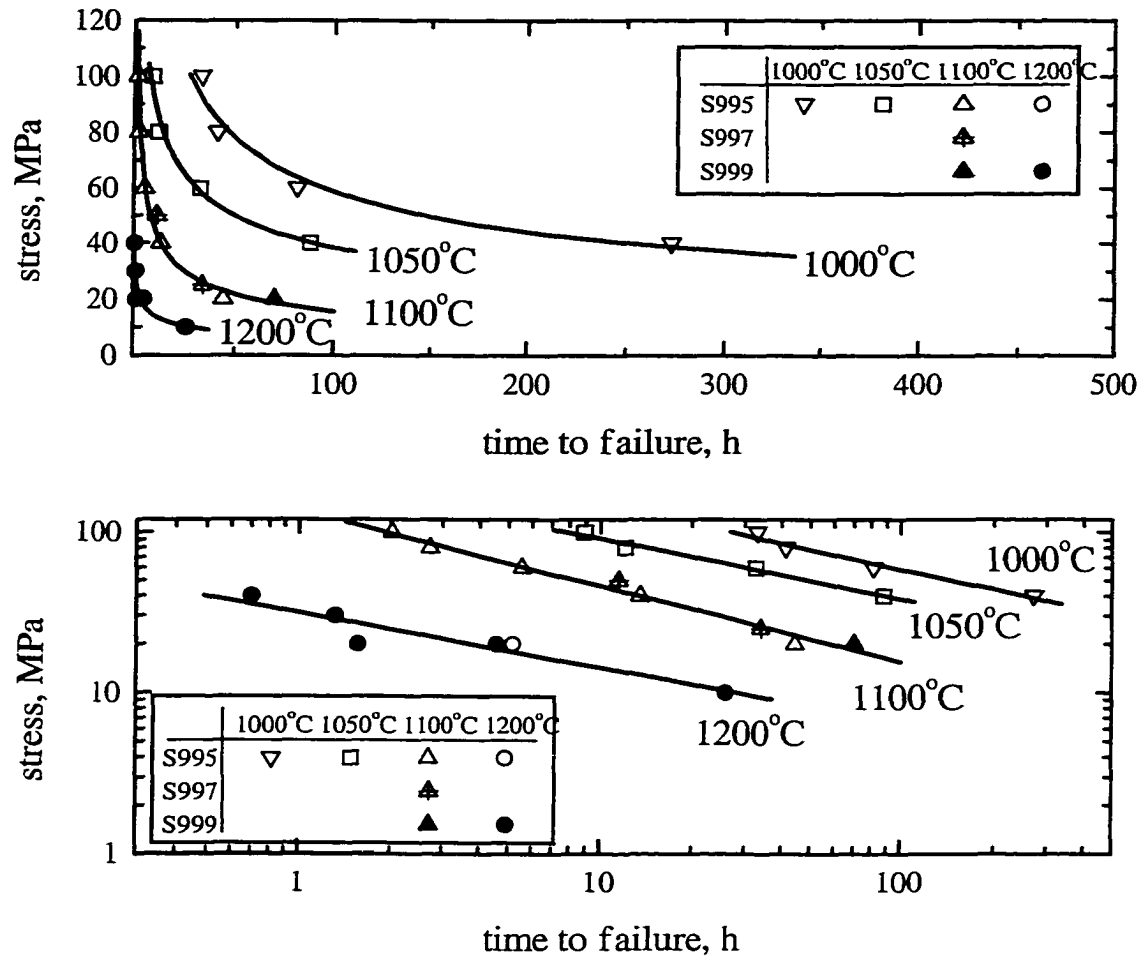
Fig. 15. Functional dependence of the time to failure, t_f, on σ and temperature, T. a) linear plot shows dramatic decrease in t_f on T and σ. b) log-log plot of same data in a.
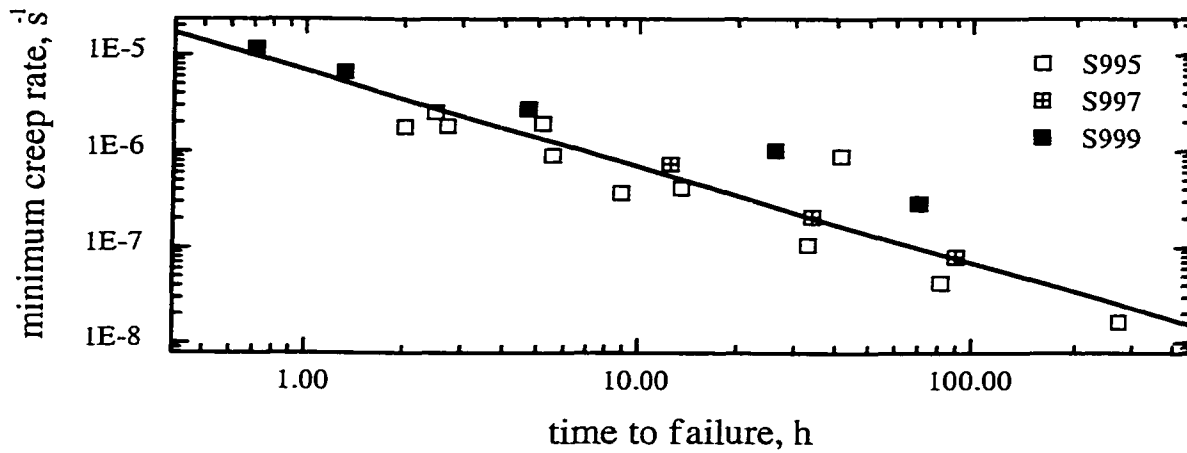
Fig. 16. Log-log plot of $\dot{\varepsilon}_{min}$ versus t_f. Straight line is obtained by least squares fitting. (see Eq. 4).
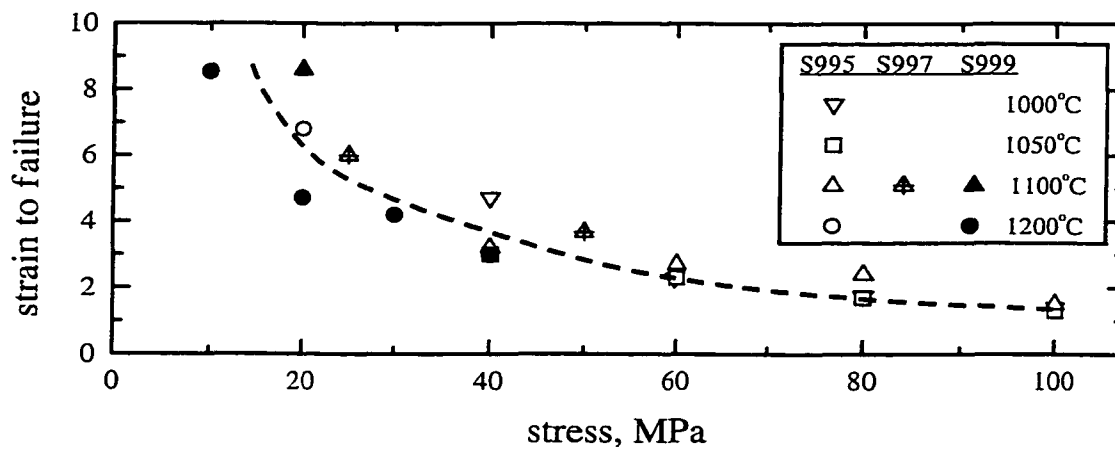
Fig. 17. Strain to failure vs. stress as a function of testing temperatures. Dotted line is guide to the eyes.
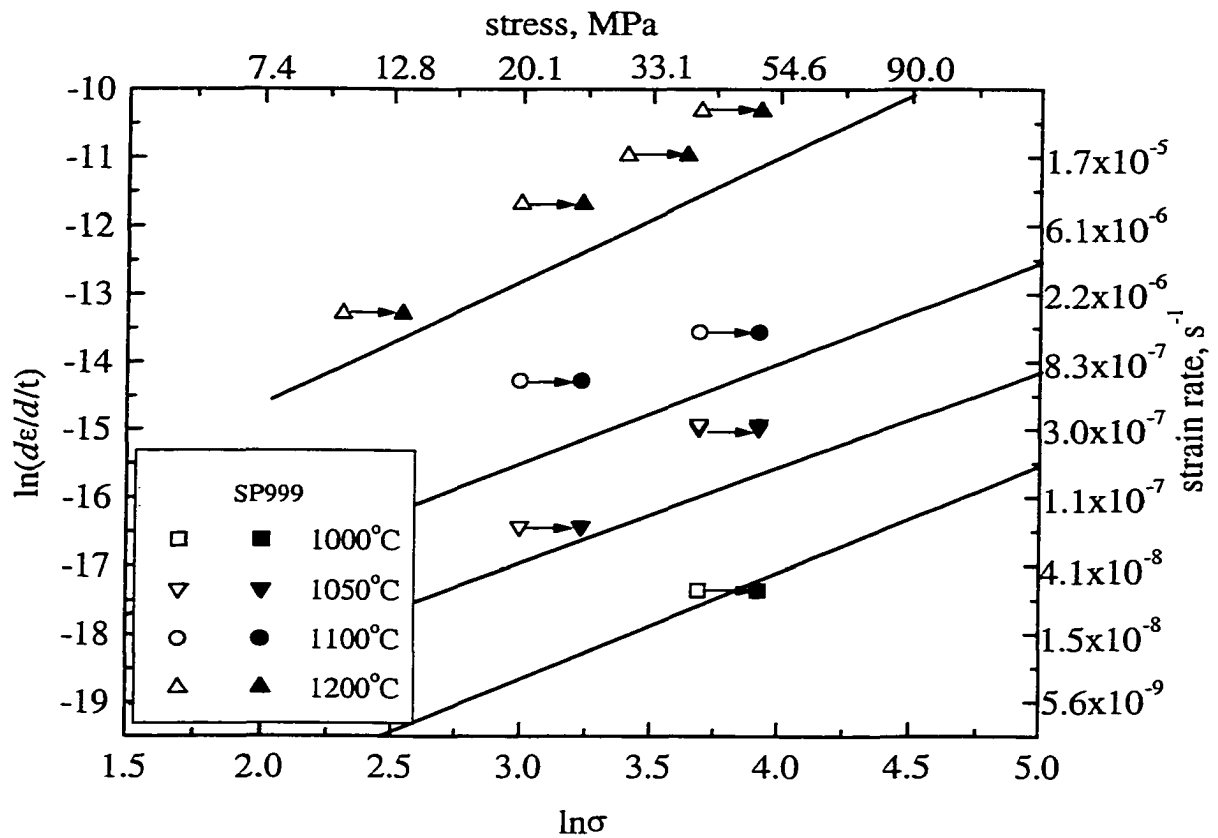
Fig 18. The ln-ln plot of $\dot{\varepsilon}_{min}$ rate vs. σ, for porous sample at various temperatures. Straight lines are those shown in Fig 11 for dense sample. The open symbols represent the results for the applied stress (applied load divided by nominal cross sectional area). The closed symbols are same results corrected for reduction of cross-section due to porosity.
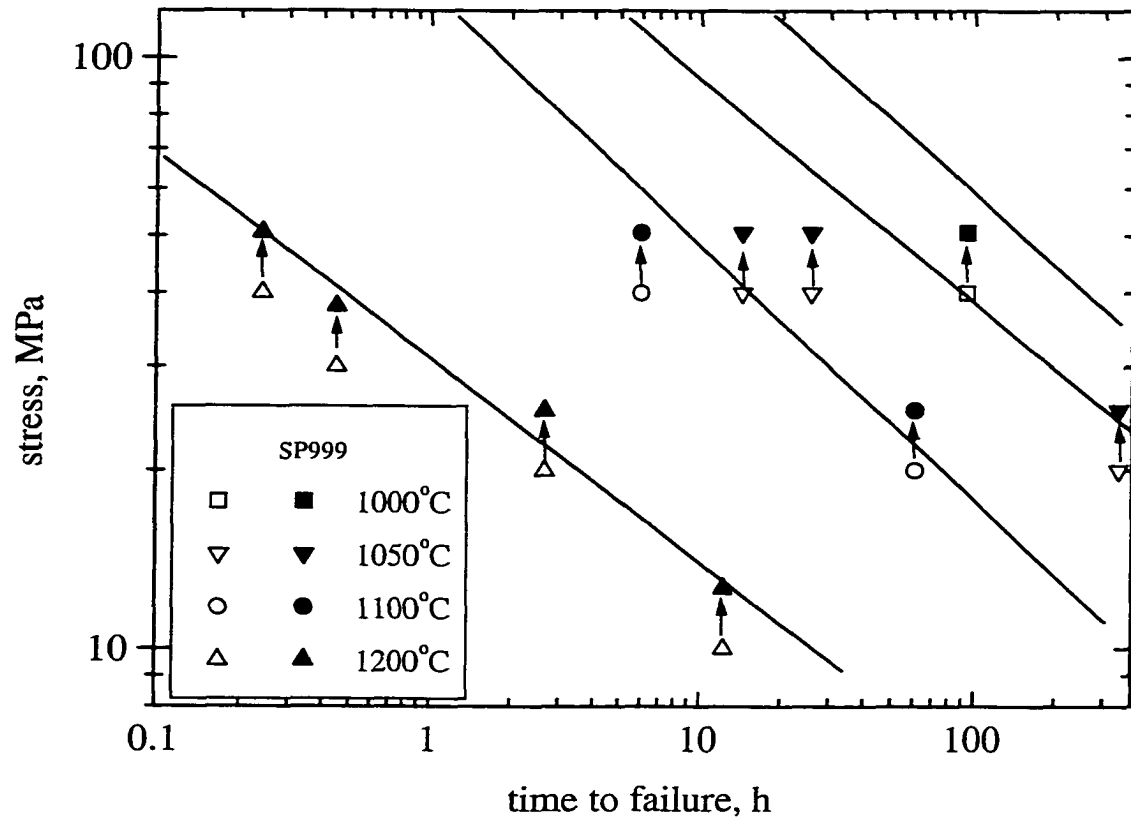
Fig 19. Log-log plot of σ versus time to failure at various temperatures. The open symbols represent the results for the applied stress (applied load divided by nominal cross sectional area) The closed symbols are same results corrected for reduction of cross-section due to porosity. Straight lines are those shown in Fig. 15.

a)

b)

c)
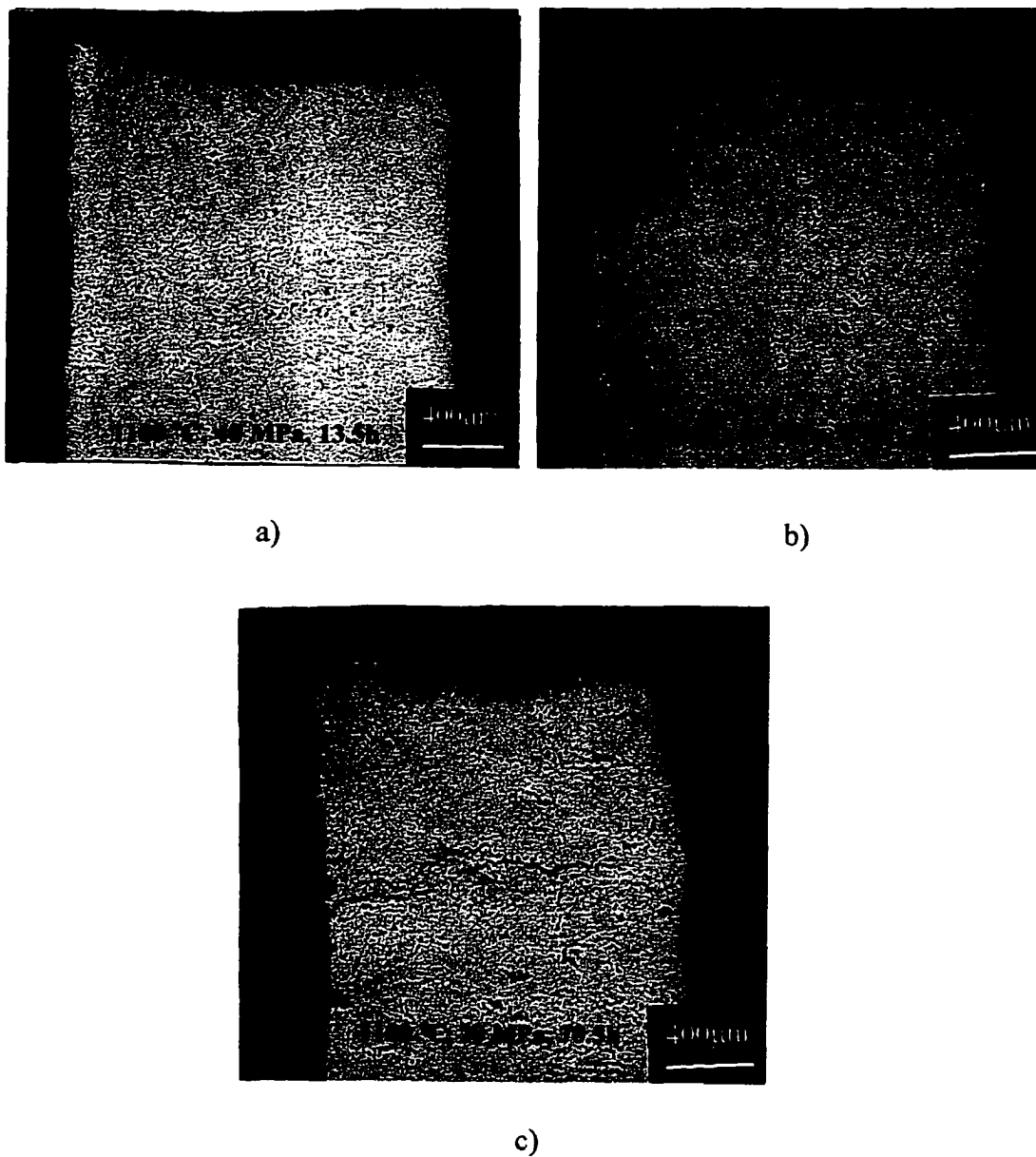
Fig. 20. OM micrographs of polished surfaces that were parallel to vertically applied load. Fracture surfaces at the top of the picture. Samples tested at: a) 1100°C and 40 MPa; t_f=13.5 h. b) 1200 °C and 40 MPa; t_f= 0.7 h. c) 1100 °C and 20 MPa; t_f = 70.5 h. Darker layers on both sides of the specimens are oxide layers
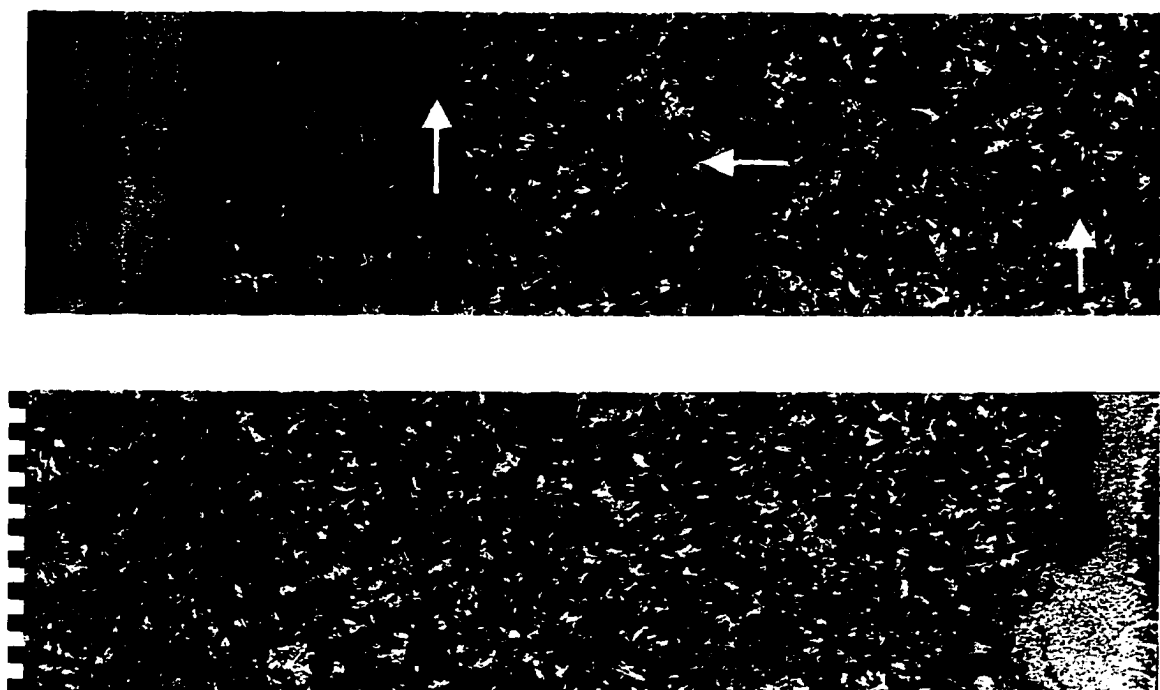
Fig. 21. OM of polished and etched gage surfaces that were parallel to the vertically applied load. Branched microcracks (arrows) spread from one side of gauge to the other. Specimen was tested at 1000 °C and 40 MPa. Time to failure 375 h.
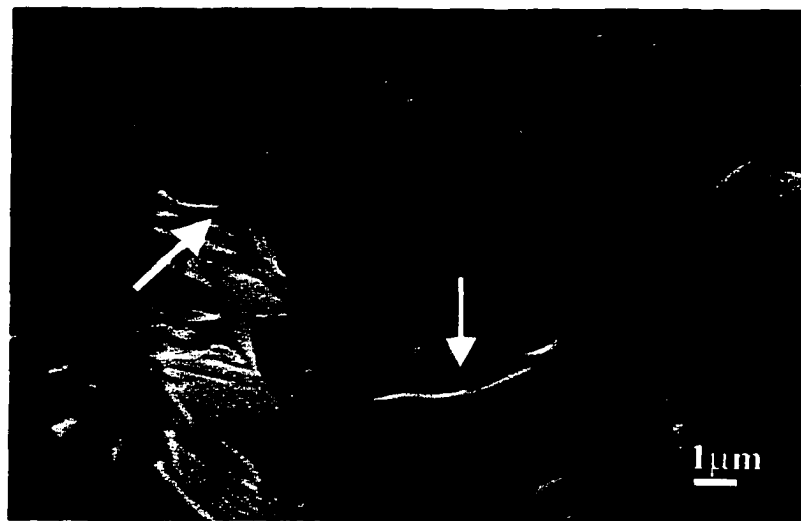
a)
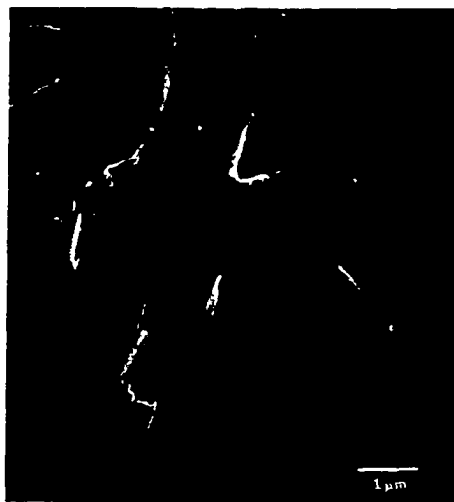
b)

Fig. 22. SEM of gauge area. (a) bent grains (arrows). Specimen tested at 60 MPa and 1000 °C, t_f = 81 h, (strain to failure 1.7%); (b) Triple point cavities and star-like microcracks at triple point. Specimen tested at 1200 °C and 20 MPa for 5.16 hours (strain to failure 6.8 %). Applied load is in vertical direction.
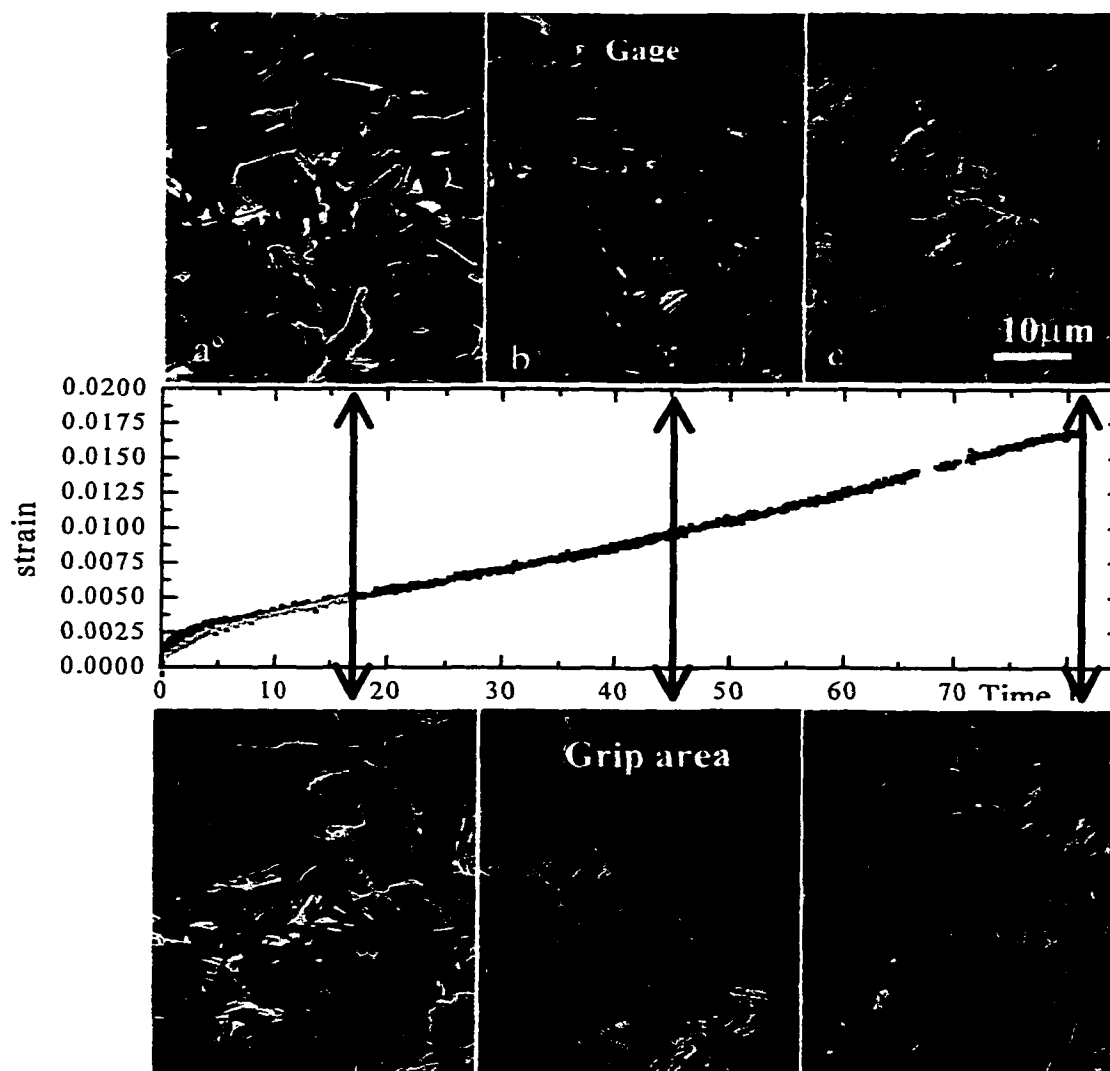
Fig. 23. Sequences of damage formation during the creep tests, for specimens tested at 60 MPa and 1000 °C. SEM micrographs of specimens' gage are shown in the upper row, corresponding micrographs of grip area are presented in the bottom row. (a) and (d), test stopped after 17 h; (b) and (e) test stopped after 45 h; (c) and (f) specimen broken after 81.3 h.
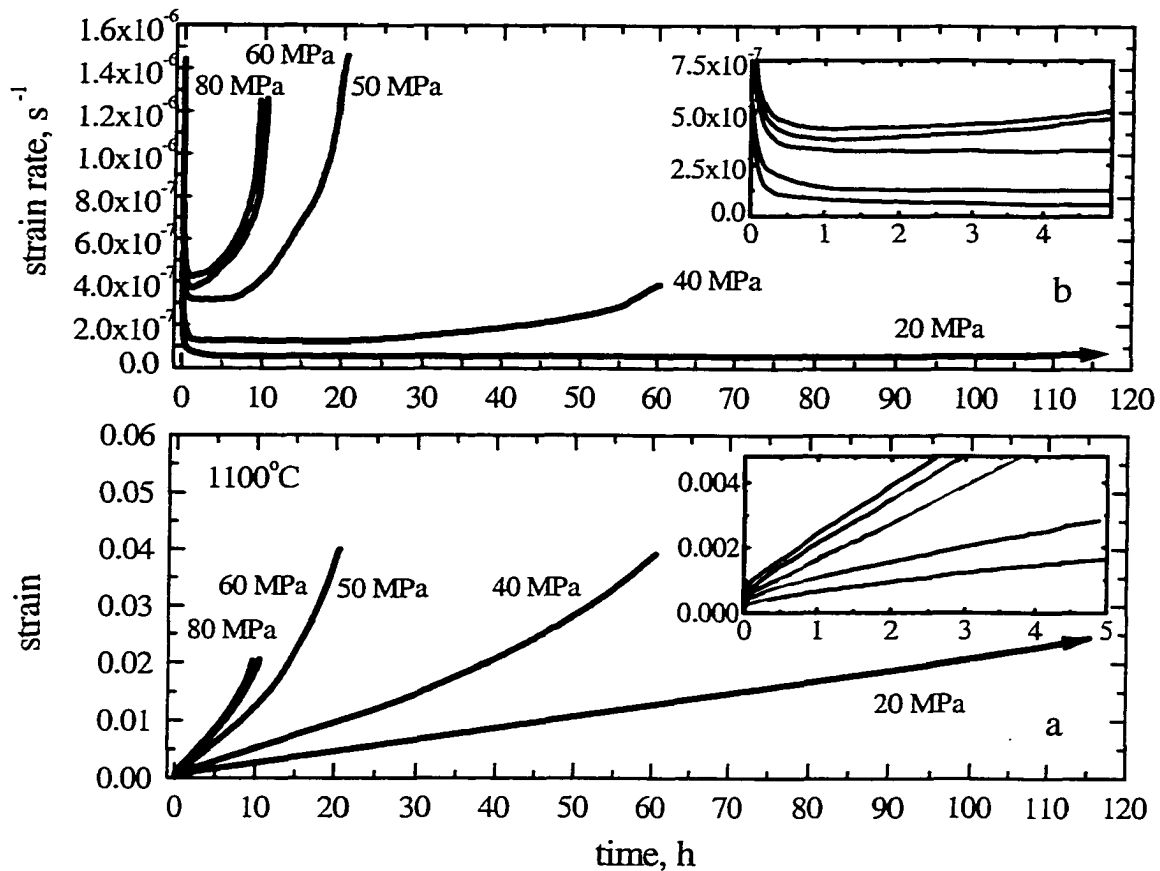
Fig. 24. Time and stress dependencies of, a) tensile strain and, b) strain rate of CG samples tested at 1100 °C. Plot (b) is obtained by differentiation of strain-time curves (a). Inserts are enlargements of the initial parts of plots shown in a and b.
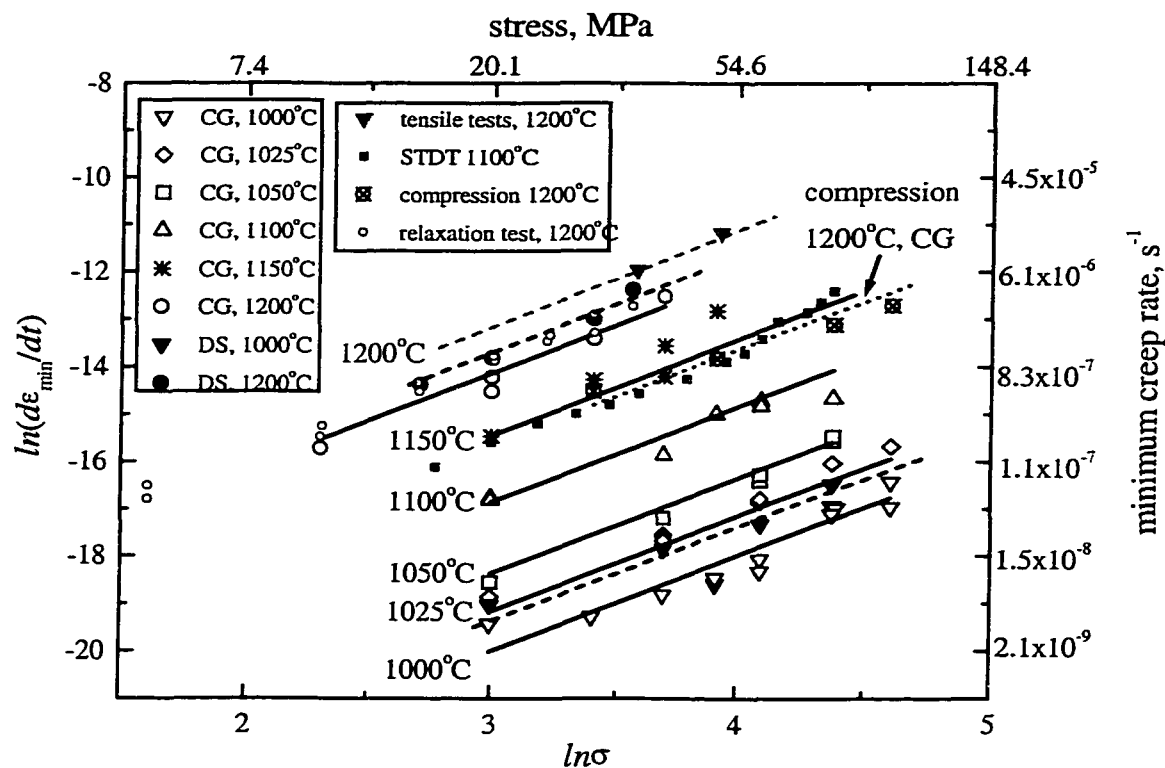
Fig. 25. Ln-ln plot of $\dot{\varepsilon}_{min}$ vs. σ as a function of T, microstructure and testing technique. Solid black lines are results of a bilinear regression for CG microstructure. The dashed black lines are results for DS. The results of tensile tests at 1200 °C (gray down triangles), STD tests at 1150 °C (small closed square), compression (hatched squares) and relaxation tests at 1200 °C (small open circles) are also shown.
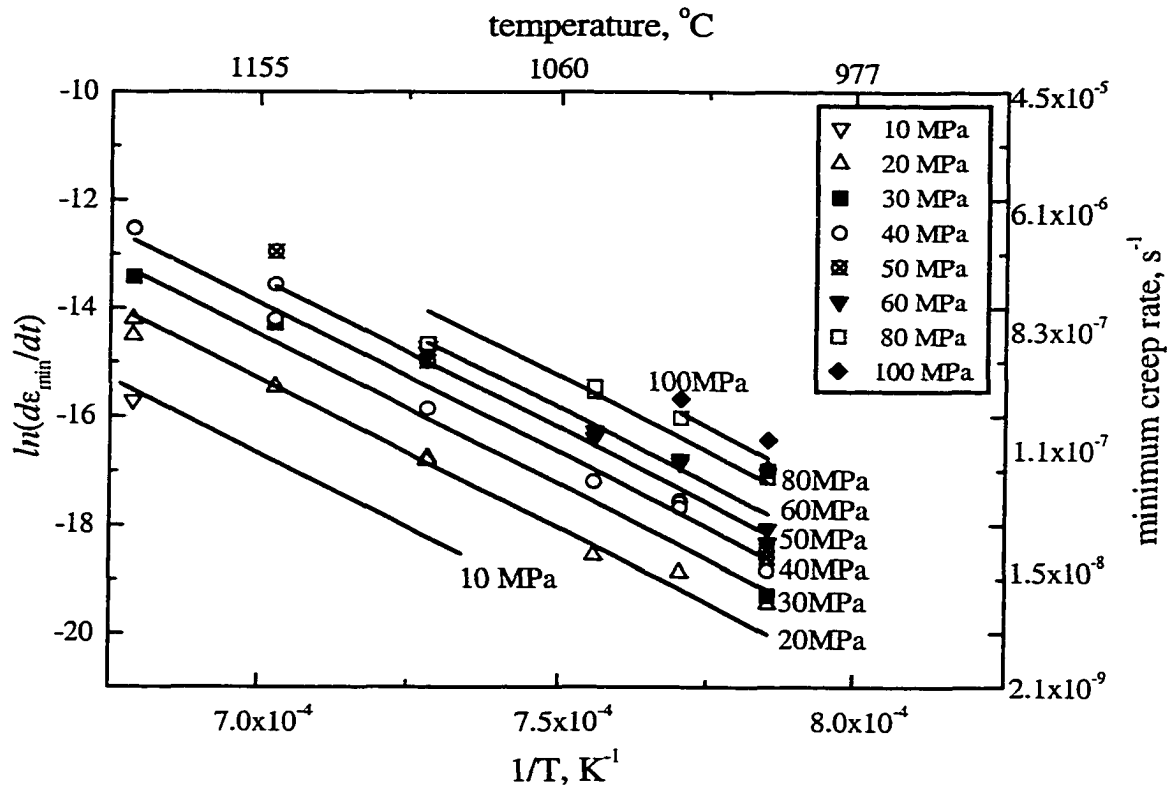
Fig. 26. Arrhenius plot of $\dot{\varepsilon}_{min}$ at various stresses. Solid black lines are results of a bilinear regression for CG microstructure.
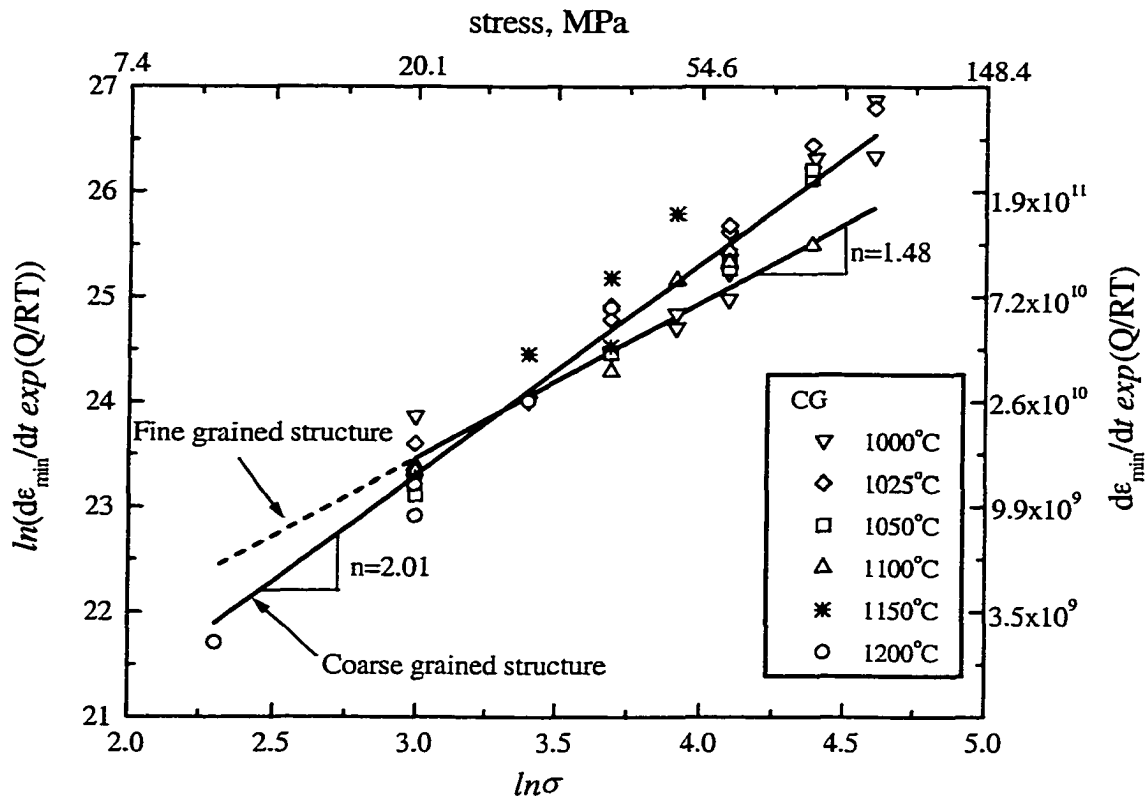
Fig. 27. Ln-ln plot of $\dot{\varepsilon}_{min}$ vs. σ for CG and FG [2] microstructures. (b) $\dot{\varepsilon}_{min}$ vs. reciprocal temperature, assuming $n=2.0$ for CG and $n=1.5$ for FG [1] microstructures.
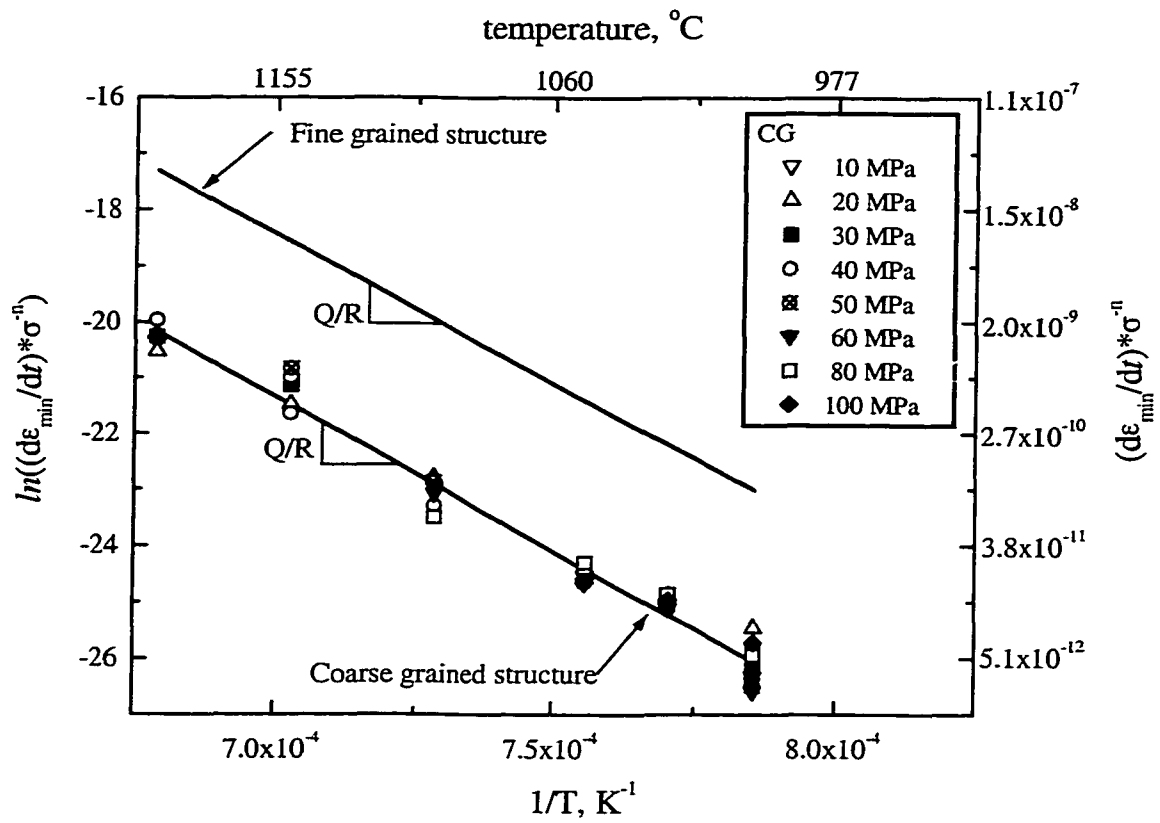
Fig. 28. Ln-ln plot $\dot{\varepsilon}_{min}$ vs. reciprocal temperature, assuming n=2.0 for CG and n=1.5 for FG [2] microstructures.
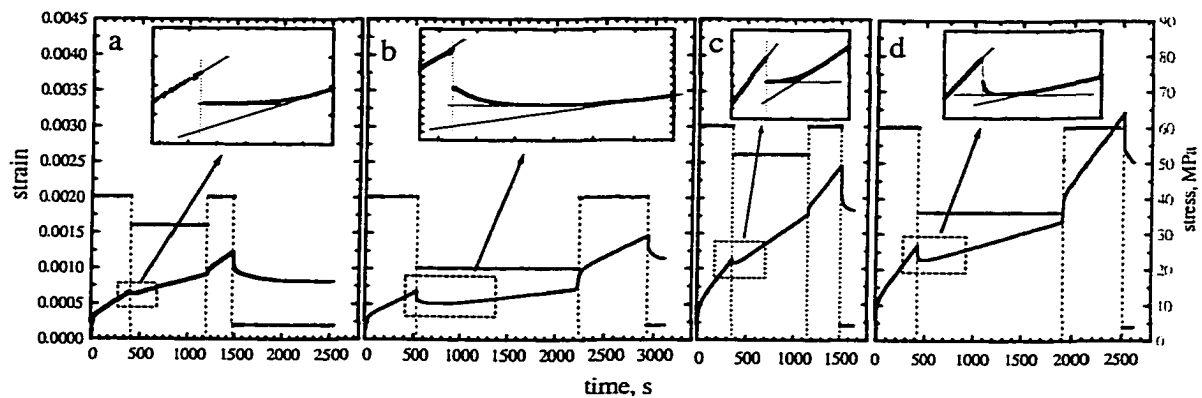
Fig. 29. Results of STD tests at 1150 °C. Black lines denote strain (left-hand side axes), while gray lines are stress (right-hand side axes). In all tests initial stress σ was reduced by $\Delta\sigma$ and then increased again up to σ. At the end of all tests samples were unloaded down to 4 MPa. (a) σ=40 MPa, $\Delta\sigma$= 8 MPa; (b) σ=40 MPa, $\Delta\sigma$= 20 MPa; (c) σ=60 MPa, $\Delta\sigma$= 8 MPa; (d) σ=60 MPa, $\Delta\sigma$= 24 MPa.
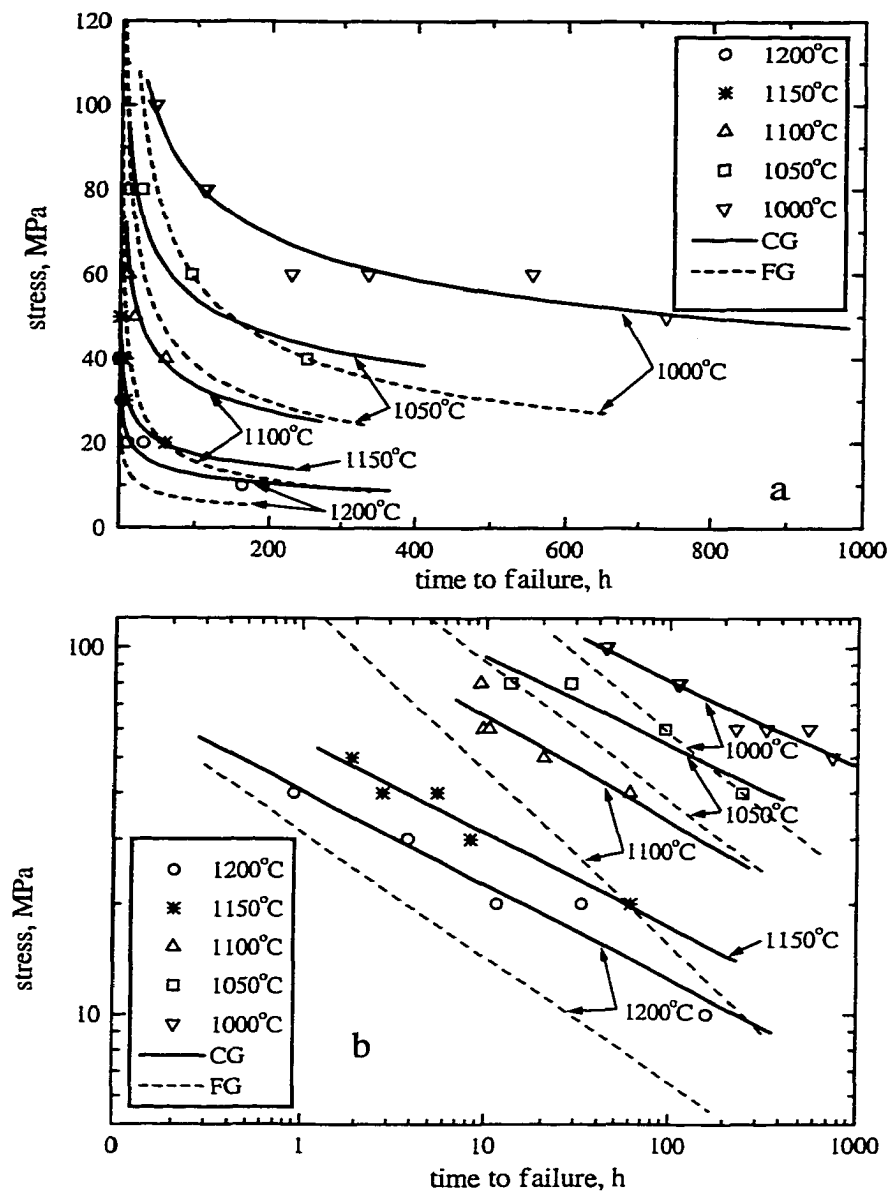
Fig. 30. Functional dependence of the time to failure, t_f, on σ and temperature, T. (a) linear plot shows dramatic decrease in t_f on T and σ. (b) log-log plot of same data in a. Solid line are obtained by least squares fitting of the results for coarse grained structure. Dashed lines are obtained by least squares fitting of the results for fine-grained structure [2].
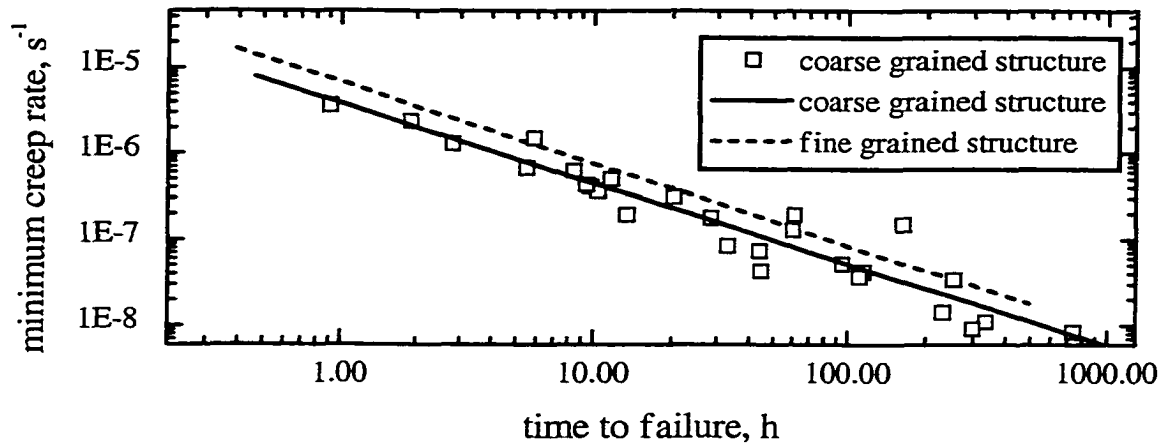
Fig. 31. Log-log plot of $\dot{\varepsilon}_{min}$ versus t_f. Solid and dashed lines were obtained by least squares fitting of CG and FG [2] microstructures.
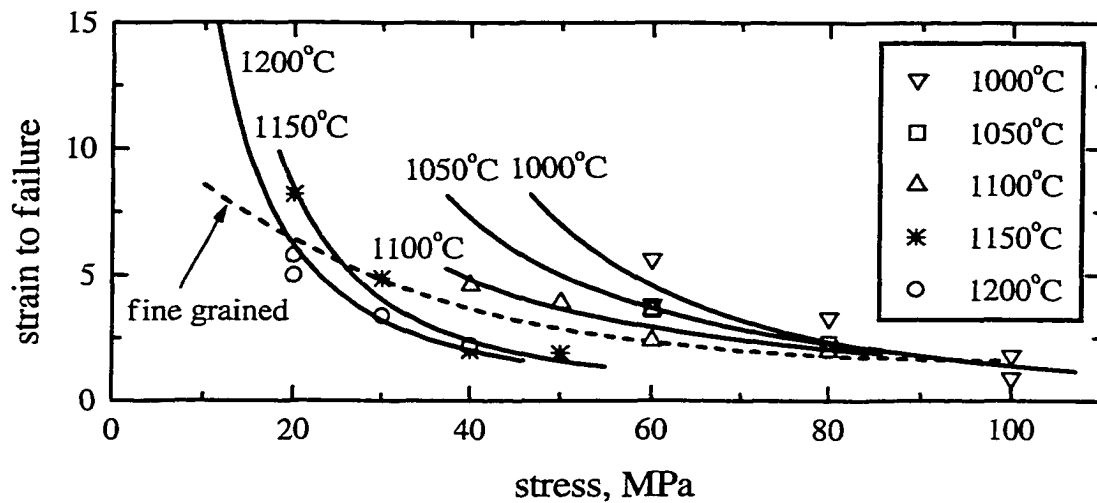
Fig. 32. Strain to failure vs. stress as a function of temperatures. Solid lines are guides to the eyes for the CG results; dotted ones for FG [2].
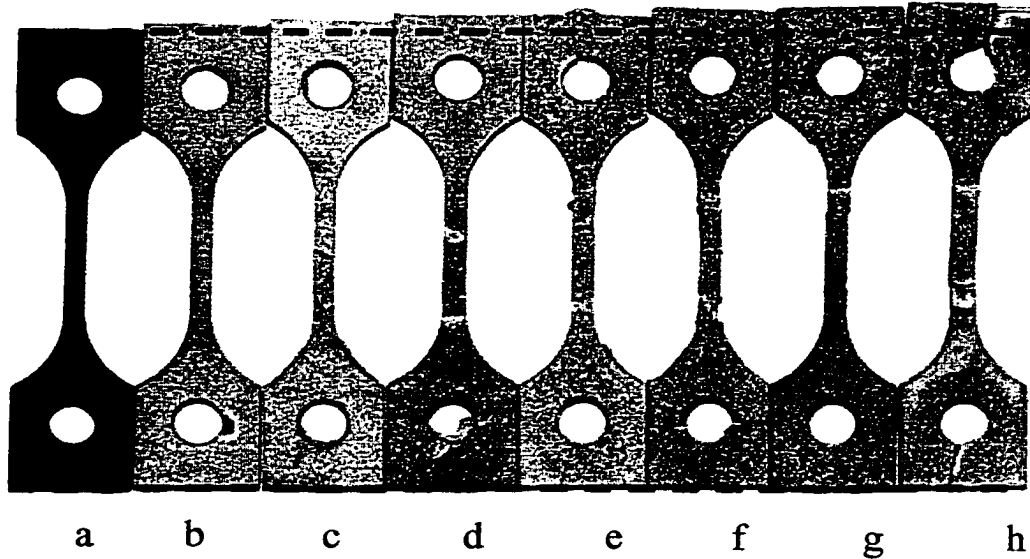
Fig. 33. Photographs of, (a) initial samples, and samples tested at, b) 1050 °C, 60

MPa, aborted after 50 h; (c) 1200 °C, 60 MPa, t_f = 3.86 h; (d) 1050 °C, 40

MPa, t_f = 252 h; (e) 1000 °C, 60 MPa, t_f = 230 h; (f) 1200 °C, 20 MPa, t_f =

32 h; (g) 1200 °C and 60 MPa, t_f = 3.86 h; (h) 1000°C, 40 MPa, aborted

after 830 h.
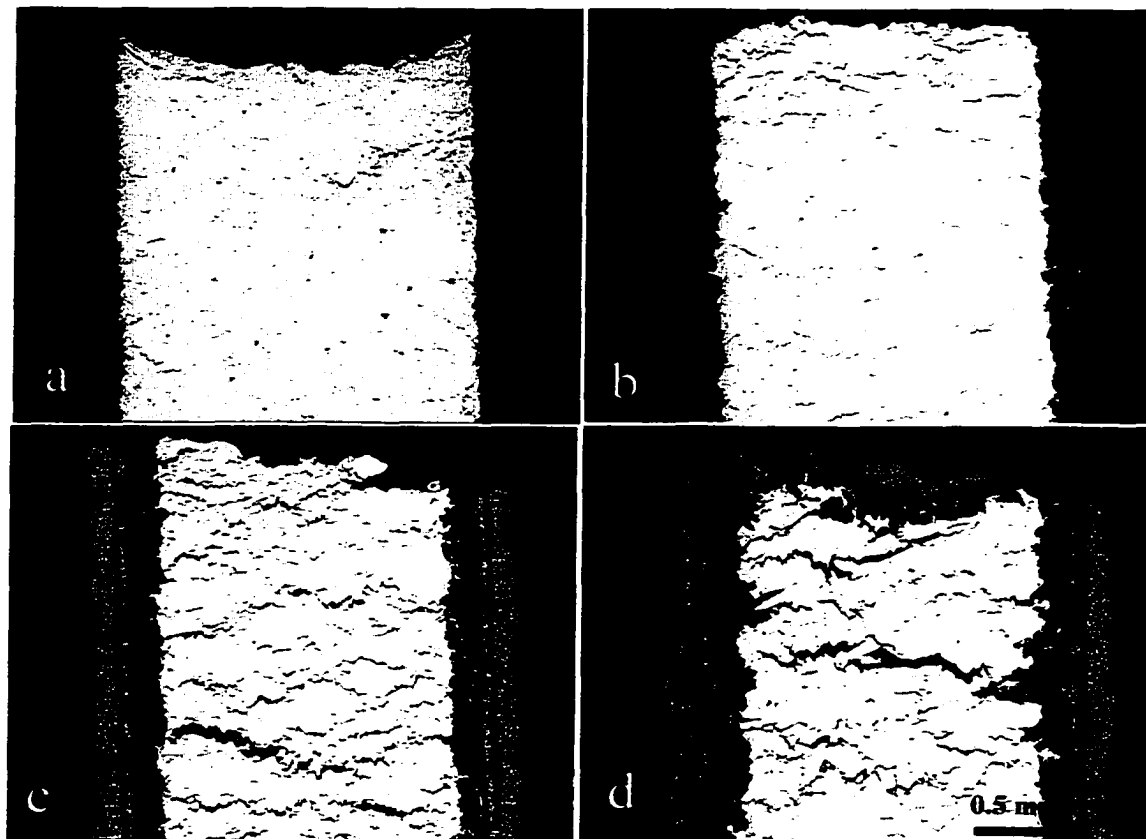
Fig. 34. OM micrographs of surfaces that were parallel to vertically applied load. Fracture surfaces at top of micrograph. Samples tested at: (a) 1000°C, 80 MPa; t_f=114 h. (b) 1100 °C, 40 MPa; t_f= 60 h. (c) 1150 °C, 20 MPa; t_f= 61 h. (d) 1200 °C, 20 MPa; t_f= 11.6 h. Dark layers on both sides of specimens are oxide layers.
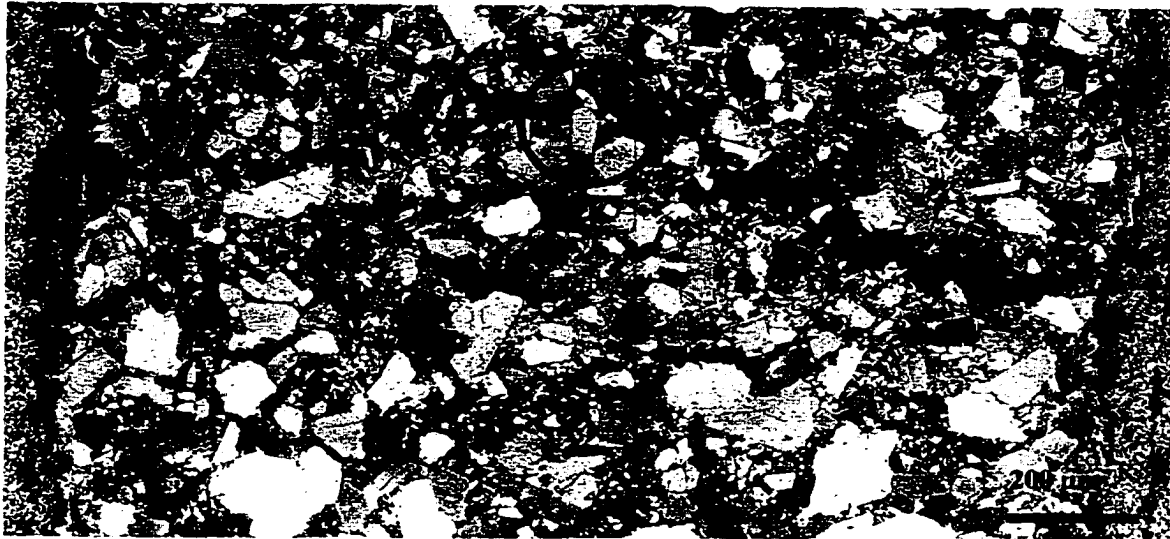
Fig. 35. Composite OM of polished and etched gage surface that was parallel to the vertically applied load. Branched microcracks spread from one side to the other. Encircled detail shows crack bridging. Test details: 1150 °C, 40 MPa, $t_f = 61$ h, $\varepsilon_f = 8$ %.

Direction of basal planes
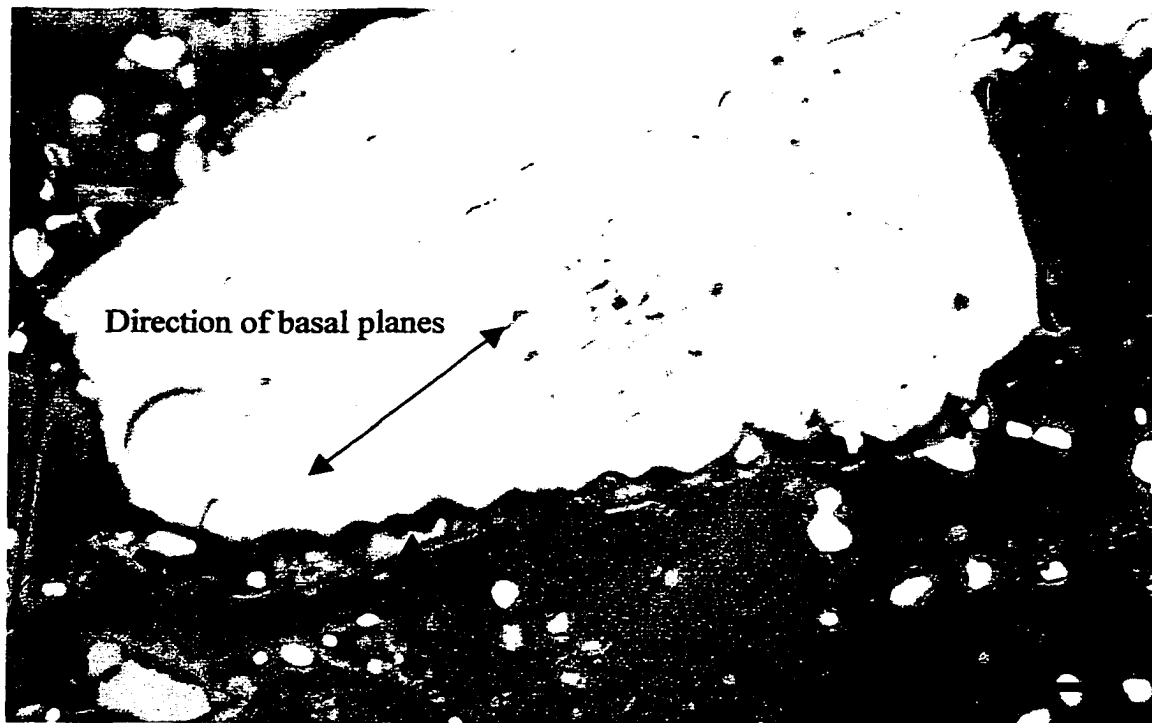
Fig. 36. OM of polished and etched gage surfaces that were parallel to the vertically applied load. Specimen with the duplex structure was tested at 1000 °C and 40 MPa. Decohesion of grain boundary is denoted by vertical arrow. Steps at grain boundary presumably formed by slip along the basal plane whose direction is indicated on figure.
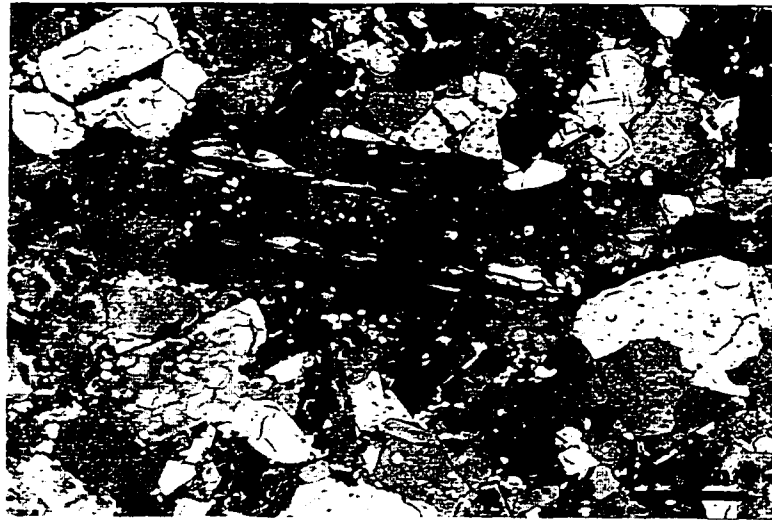
Fig. 37. OM micrographs of polished and etched gage surface that was parallel to vertically applied load showing. Delamination denoted by arrows; part of the grain between delamination cracks is slightly bent; 1000 °C and 80 MPa.

Fig. 38. OM micrographs of polished and etched gage surface that was parallel to vertically applied load showing. Bent lamella, denoted by arrow, serves as a crack bridge; 1100 °C and 40 MPa.
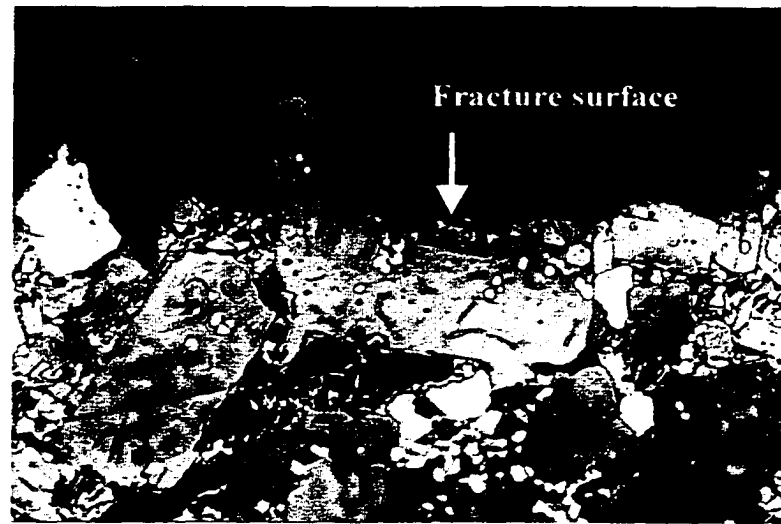
Fig. 39. OM micrographs of polished and etched gage surface that was parallel to vertically applied load showing. Fractured lamella which served as a crack bridge across the fracture surface denoted by arrow; 1150 °C and 20 MPa.
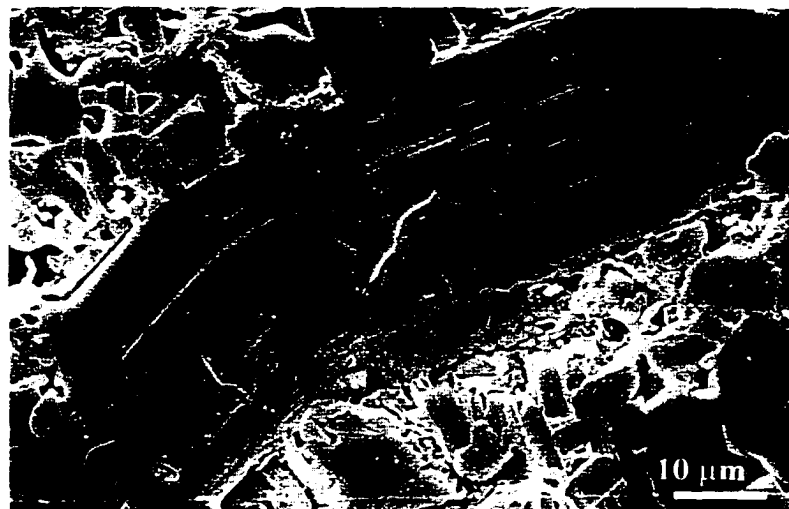
Fig. 40. SEM micrograph of polished and etched gage surface that was parallel to vertically applied load showing bent grain; 1150 °C and 20 MPa.
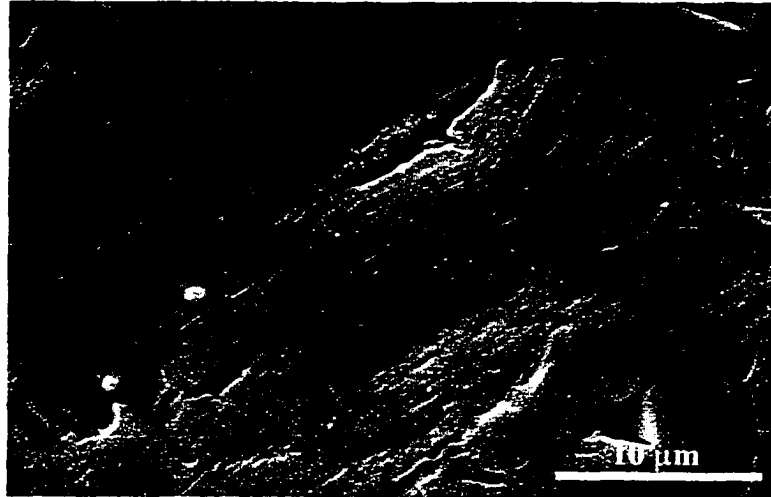
Fig. 41. SEM micrograph of polished and etched gage surface that was parallel to vertically applied load showing delamination and kinking of a grain;1050 °C and 40 MPa.

Fig. 42. SEM micrograph of polished and etched gage surface that was parallel to vertically applied load showing crack bridge; 1150 °C and 20 MPa.

Fig. 43. SEM of fracture surface. Kinked lamina sticking out from fracture; 1000 °C and 100 MPa.
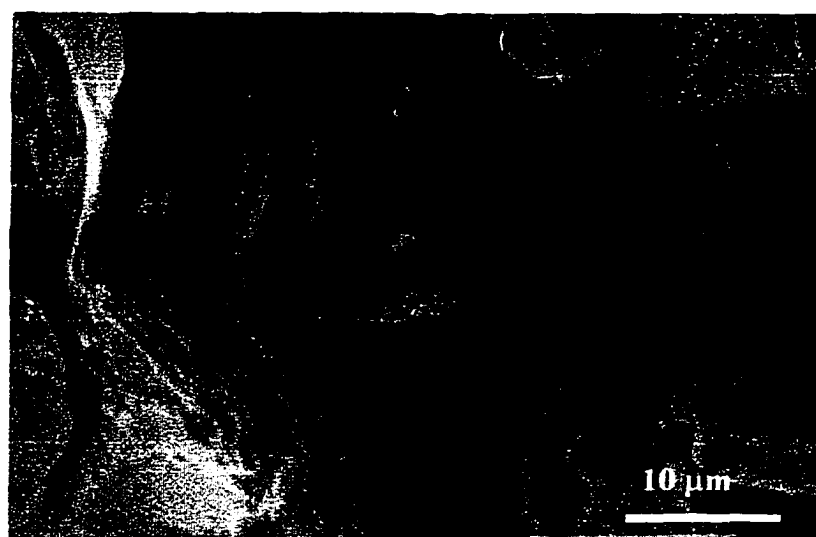
Fig. 44. SEM of fracture surface. Transgranular fracture (left) and intergranular fracture (right); 1100 °C and 100 MPa.
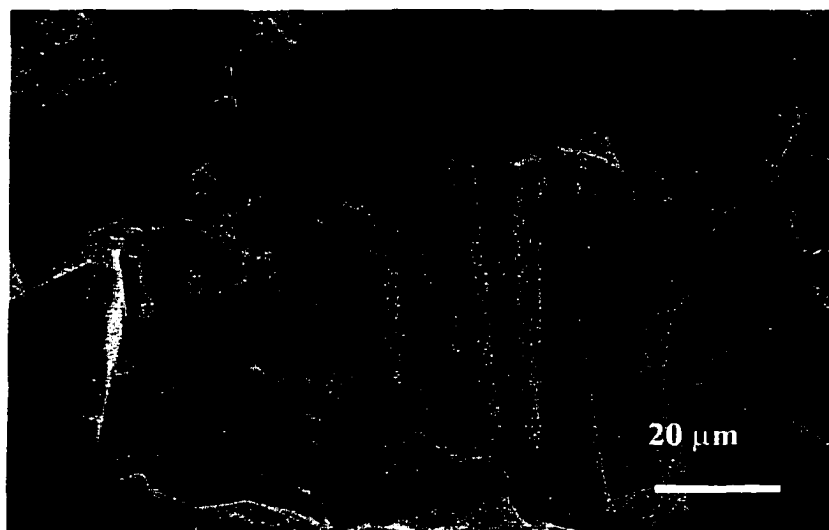
Fig. 45. SEM of fracture surface. Broken grain sticking out from the fracture surface; 1100 °C and 100 MPa.
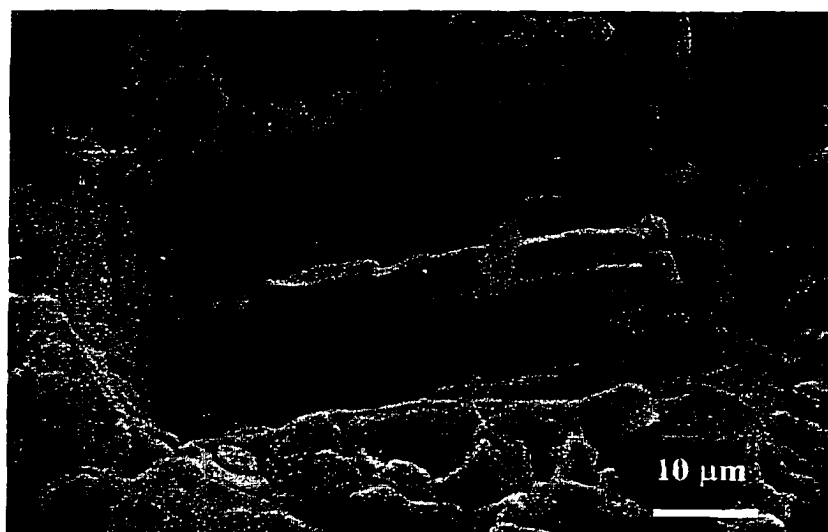
Fig. 46. SEM of fracture surface. Pullout of grain that also served as a crack bridge; 1050 °C and 80 MPa.
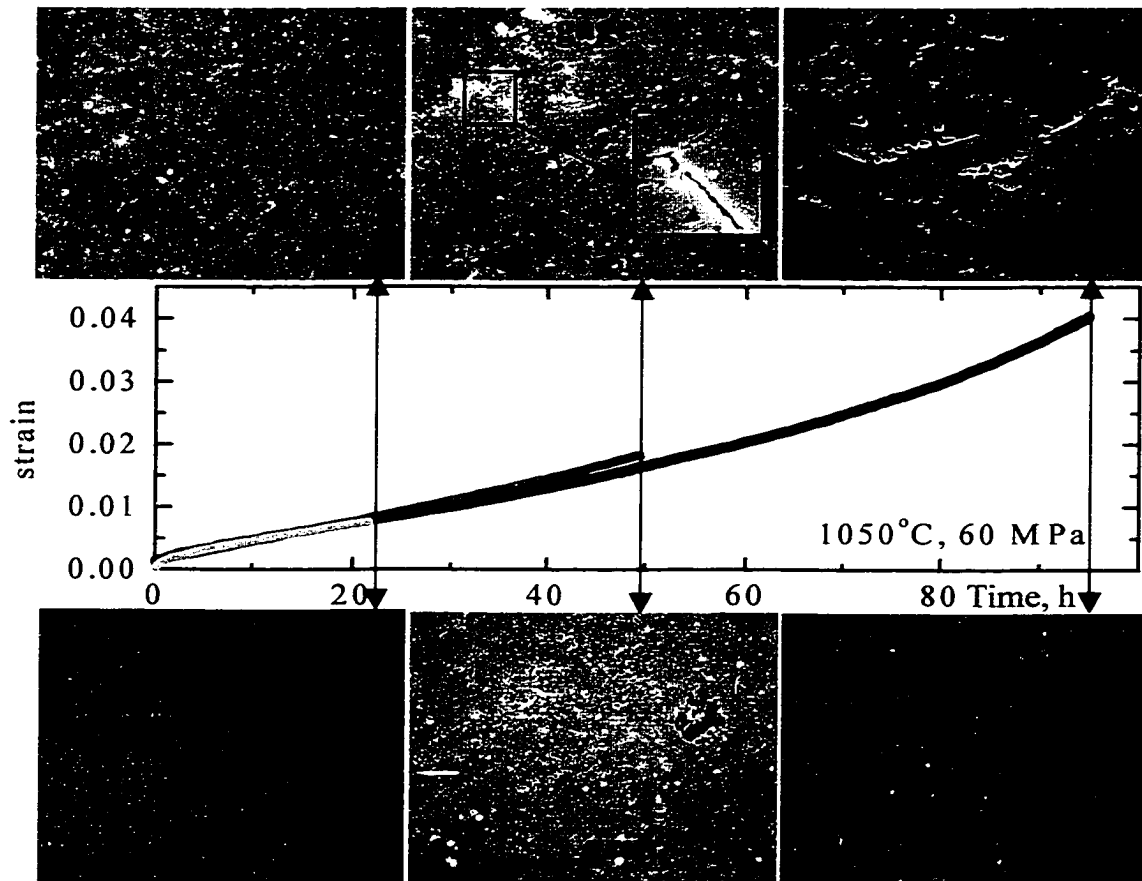
Fig. 47. Sequences of damage formation during creep tests, for specimens tested at 60 MPa and 1050 °C. Creep results are shown in middle panel. SEM micrographs of specimens' gage are shown in the upper rows, corresponding micrographs of grip area are in the bottom rows. (a) and (d), test stopped after 21 h; (b) and (e) test stopped after $\approx$ 50 h; (c) and (f) specimen failed after $\approx$ 95 h. Applied load is in vertical direction.
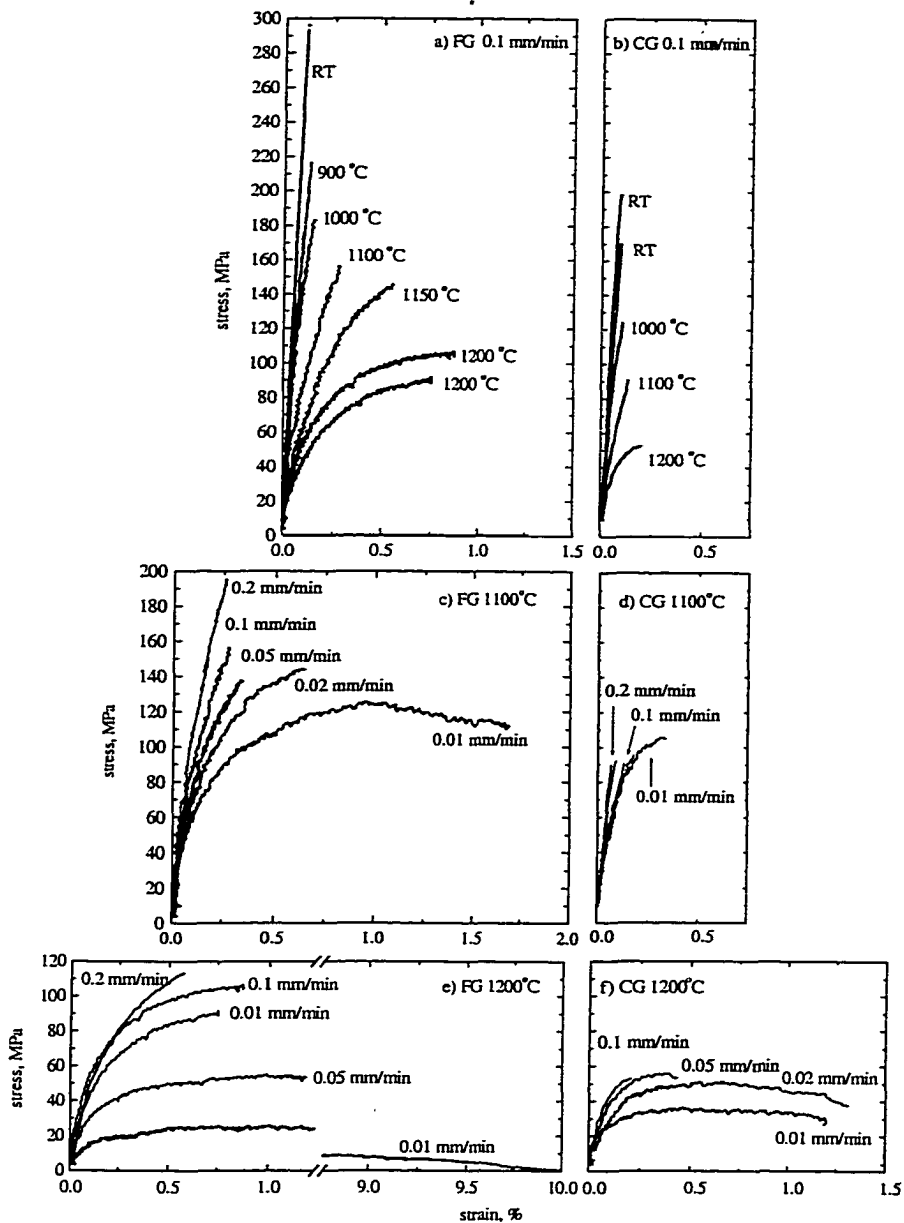
Fig. 48. Engineering stress vs. strain plots obtained from tensile tests at constant CHD, (a) FG as a function of T, CHD of 0.1mm/min; (b) CG as a function of T, CHD of 0.1 mm/min; (c) FG at 1100 °C as a function of CHD rate; (d) CG at 1100 °C as a function of CHD rate; (e) FG structure at 1200 °C as a function of CHD rate; (f) CG structure at 1200 °C as a function of CHD rate.
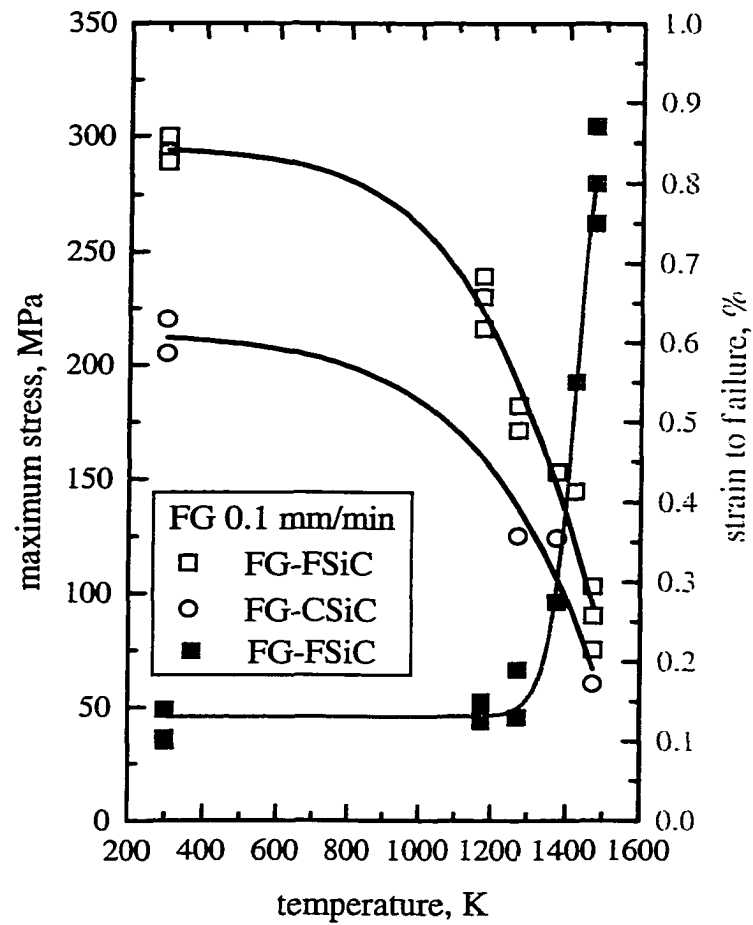
Fig. 49. Maximum stress (black) and strain-to-failure (gray) for FG as a function of temperature and microstructure (see text for details). Results were obtained from tensile tests at CHD rate of 0.1 mm/min.
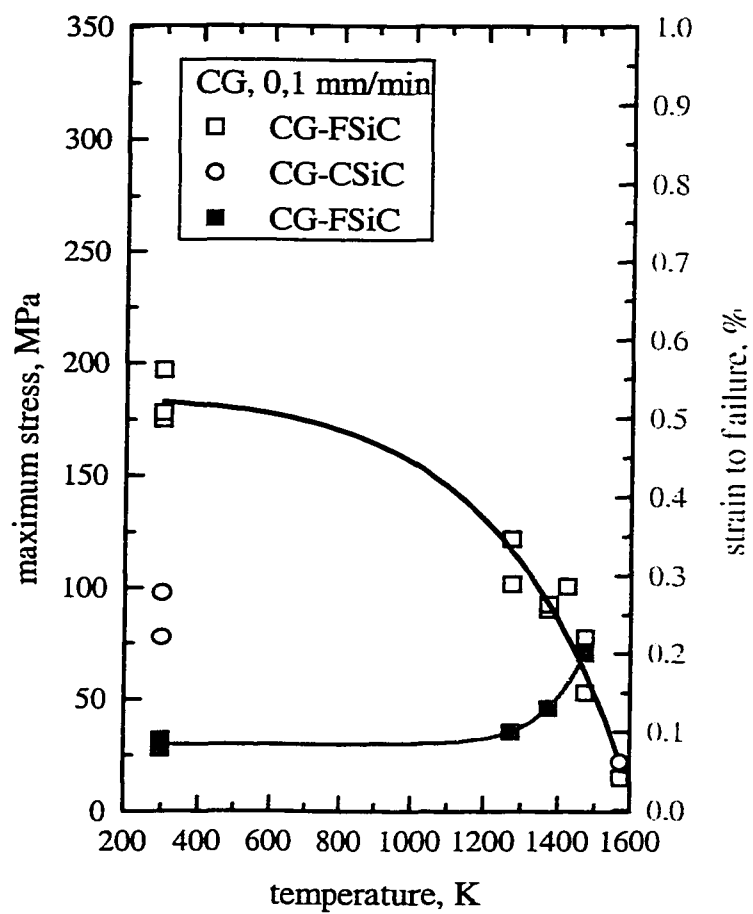
Fig. 50. Maximum stress (black) and strain-to-failure (gray) for CG as a function of temperature and microstructure (see text for details). Results were obtained from tensile tests at CHD rate of 0.1 mm/min.
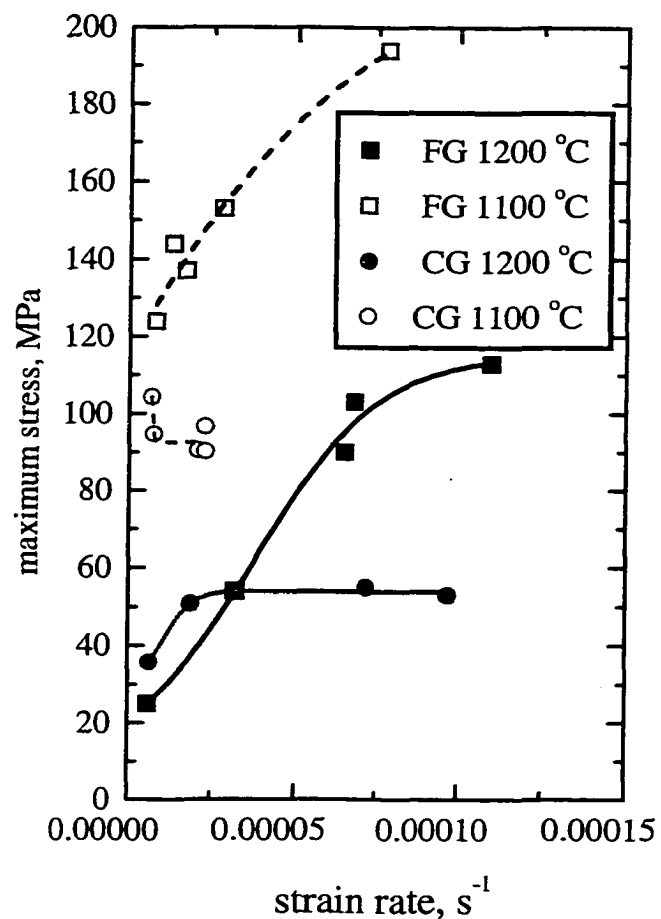
Fig. 51. The maximum stress as a function of strain rate. Results are obtained from tensile tests carried out at 1100 °C (gray) and 1200 °C (black) and different CHD rate. The strain rate was calculated from the slopes of the strain-time curves measured by the extensometer. Dashed (CG) and solid (FG) lines are guide to the eyes.
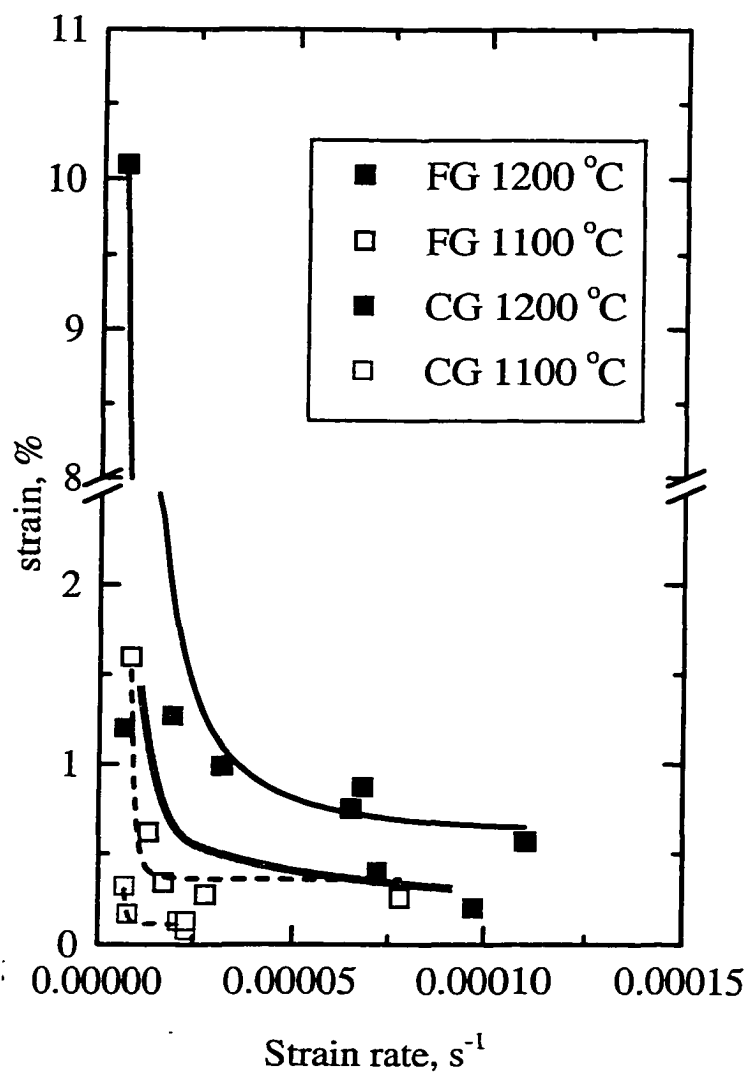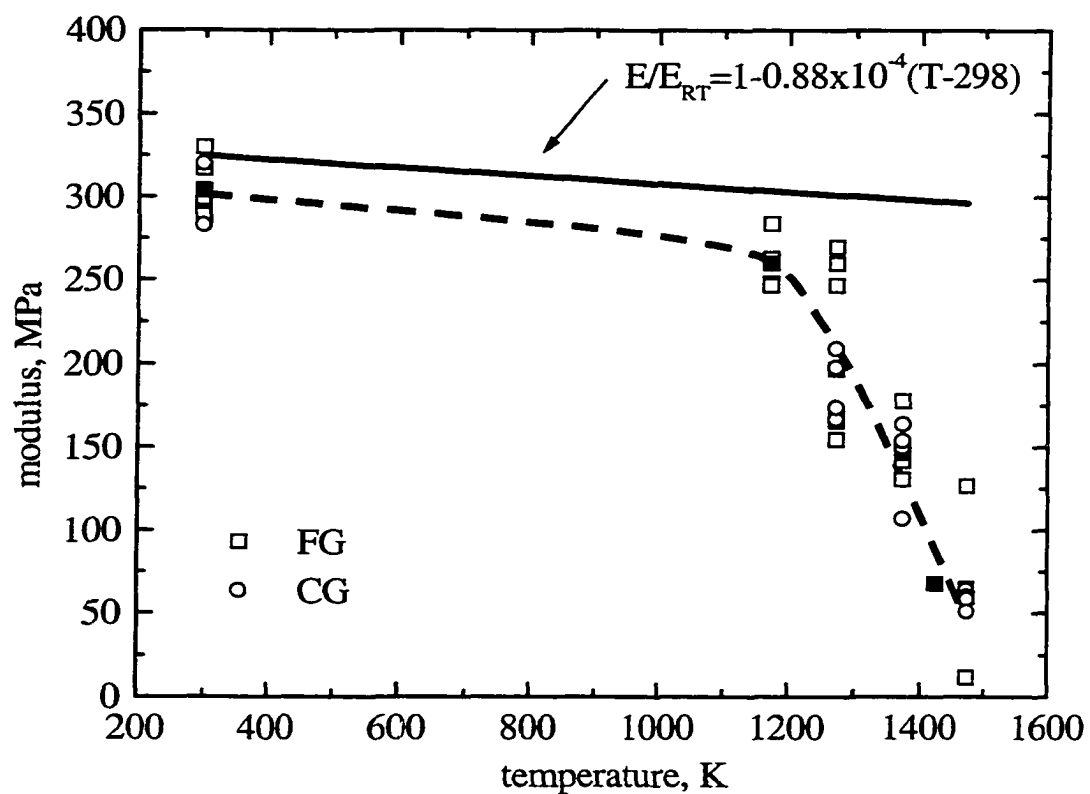
Fig. 52. The strain to failure as a function of strain rate. Results are obtained from tensile tests carried out at 1100 °C (gray) and 1200 °C (black) and different CHD rate. The strain rate was calculated from the slopes of the strain-time curves measured by the extensometer. Dashed (CG) and solid (FG) lines are guide to the eyes.

$$E/E_{RT}=1-0.88 \times 10^{-4}(T-298)$$

Fig. 53. Modulus measured as slope of the initial part of the engineering stress-strain curves (Fig. 48) plotted as a function of temperature. Open squares represent data for FG samples, while open circles represents data for CG ones. Dashed line is guide to the eyes. Solid line represents estimated changes in modulus with temperature from sound velocity measurement [56].
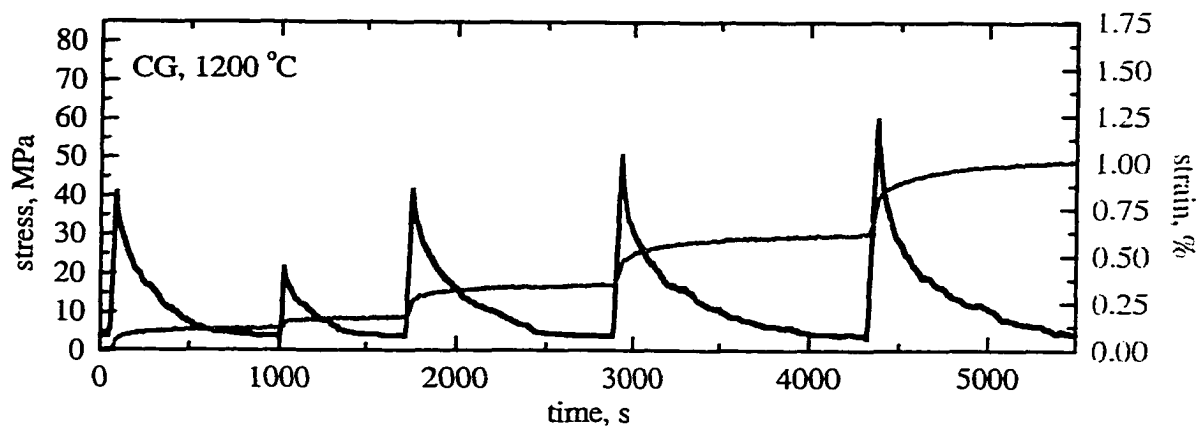
Fig. 54. Time dependence of stresses (black lines) and strains (gray curves) obtained form stress relaxation tests at 1200 °C for CG samples. Strain was measured by extensometer.
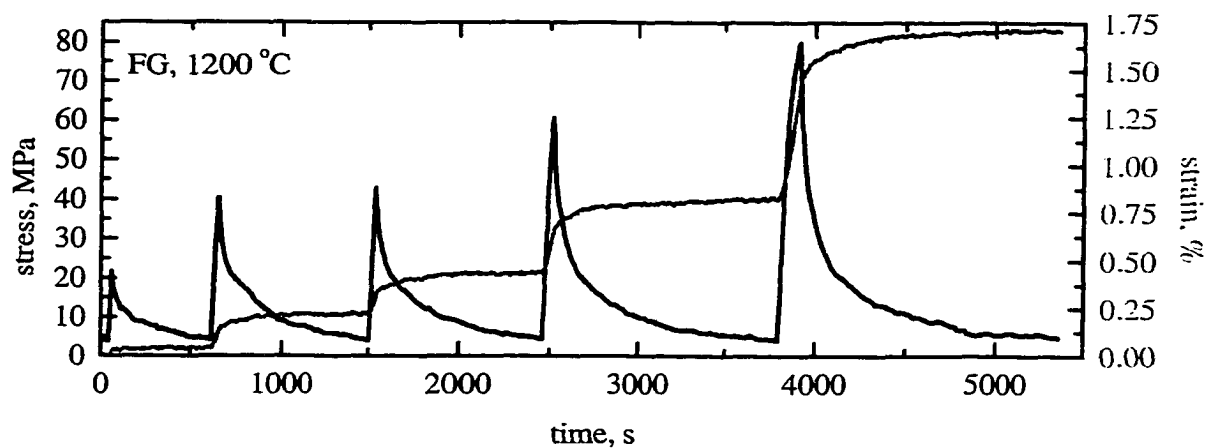

Fig. 55. Time dependence of stresses (black lines) and strains (gray curves) obtained form stress relaxation tests at 1200 °C for FG samples. Strain was measured by extensometer.
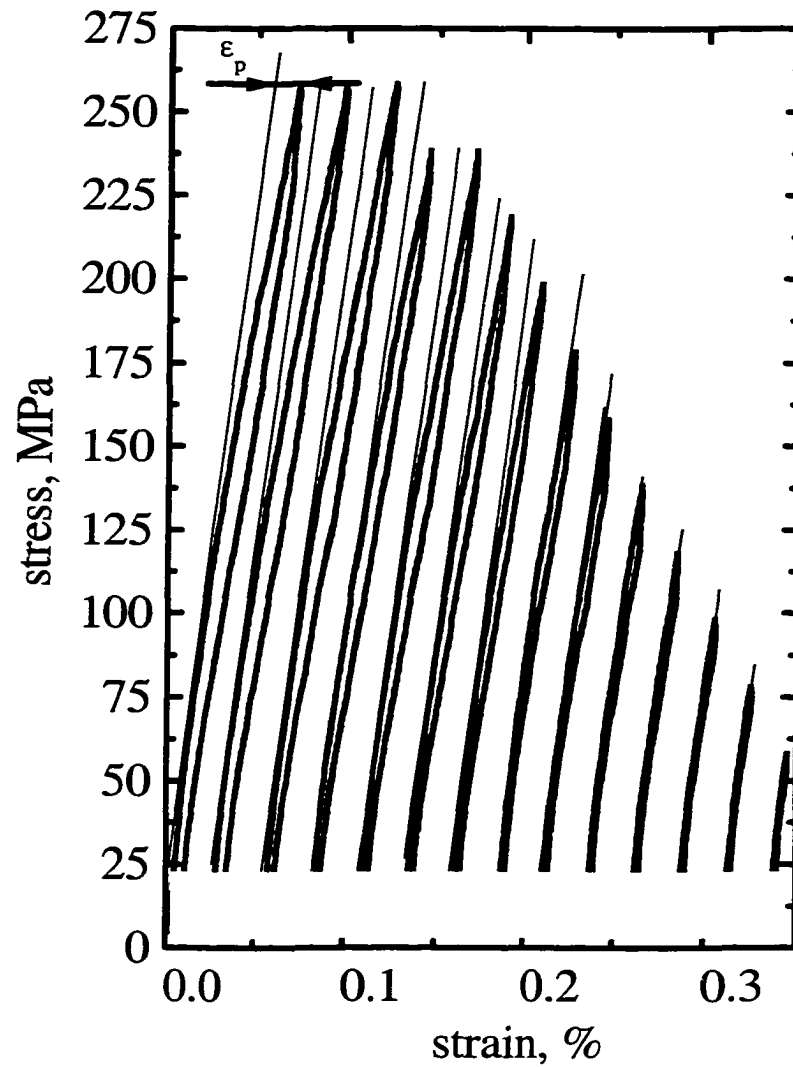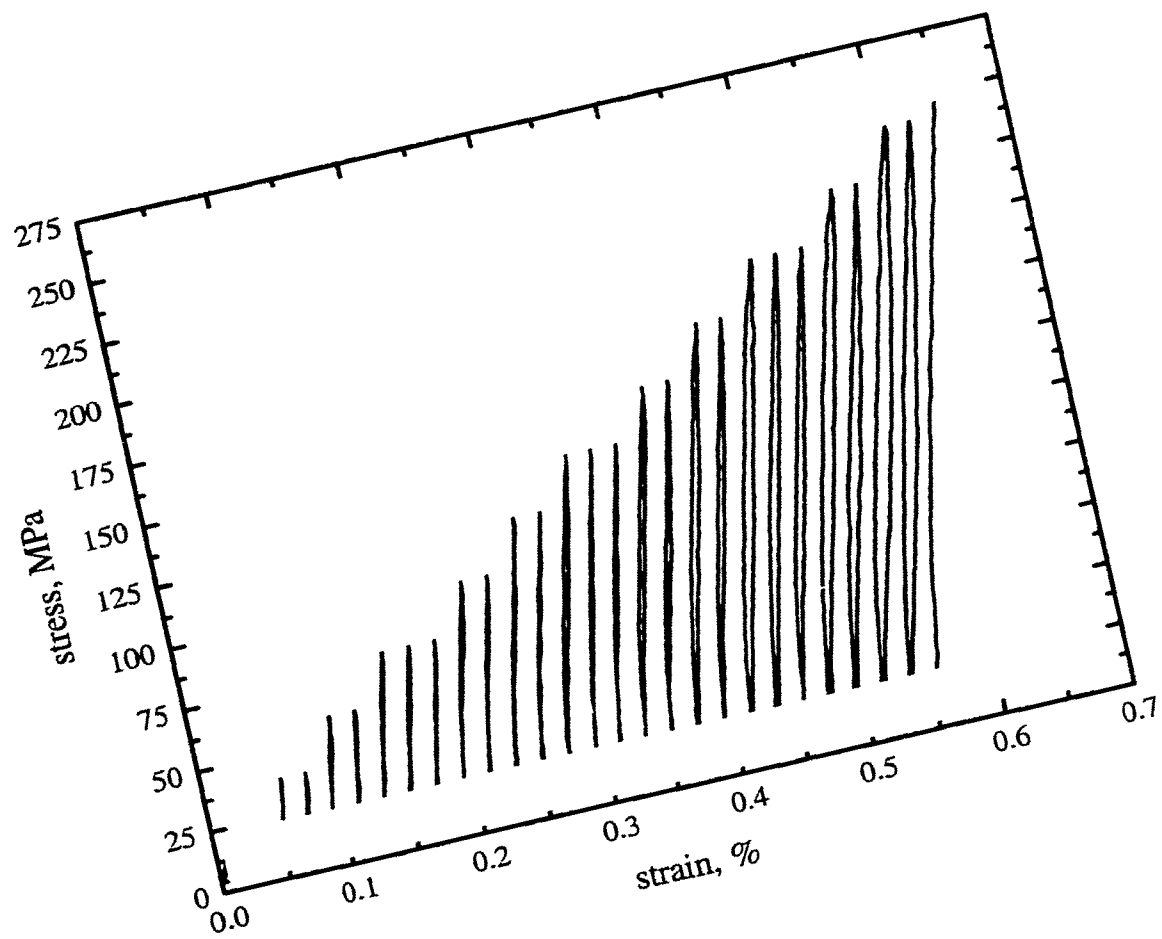
Fig. 56. Room temperature stress-strain curves obtained from cyclic loading-unloading tests for FG microstructure at a constant rate of 0.67 MPa/s for decreasing stress amplitudes. ε_p represents deviation from the linear elastic strain at maximum cycle stress – i.e. anelastic strain.

Fig. 57. Room temperature stress-strain curves obtained from cyclic loading-unloading tests for FG microstructure at a constant rate of 0.67 MPa/s for increasing stress amplitude.
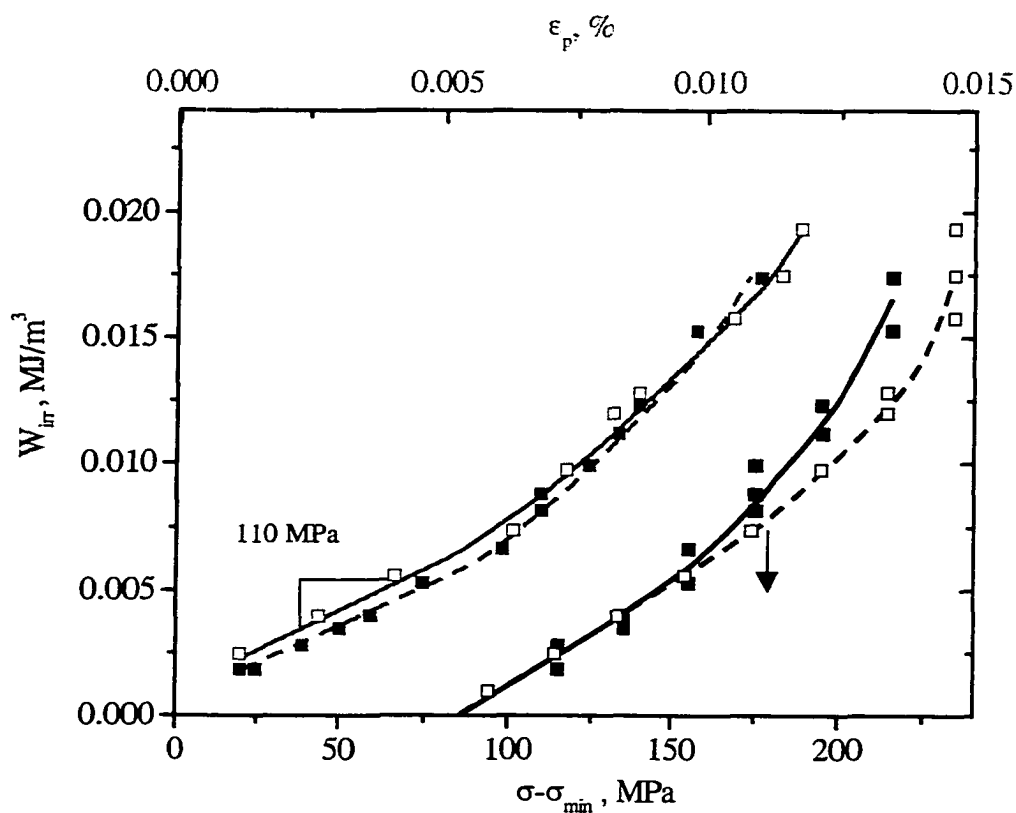
Fig. 58. Irreversible work, W_{irr}, as a function of maximum cycle stresses (black) and ε_p (gray) for FG samples estimated from Figs. 56 and 57. Open symbols represent results from tests with decreasing stress amplitudes, while closed symbol represent results from tests with increasing stress amplitudes.
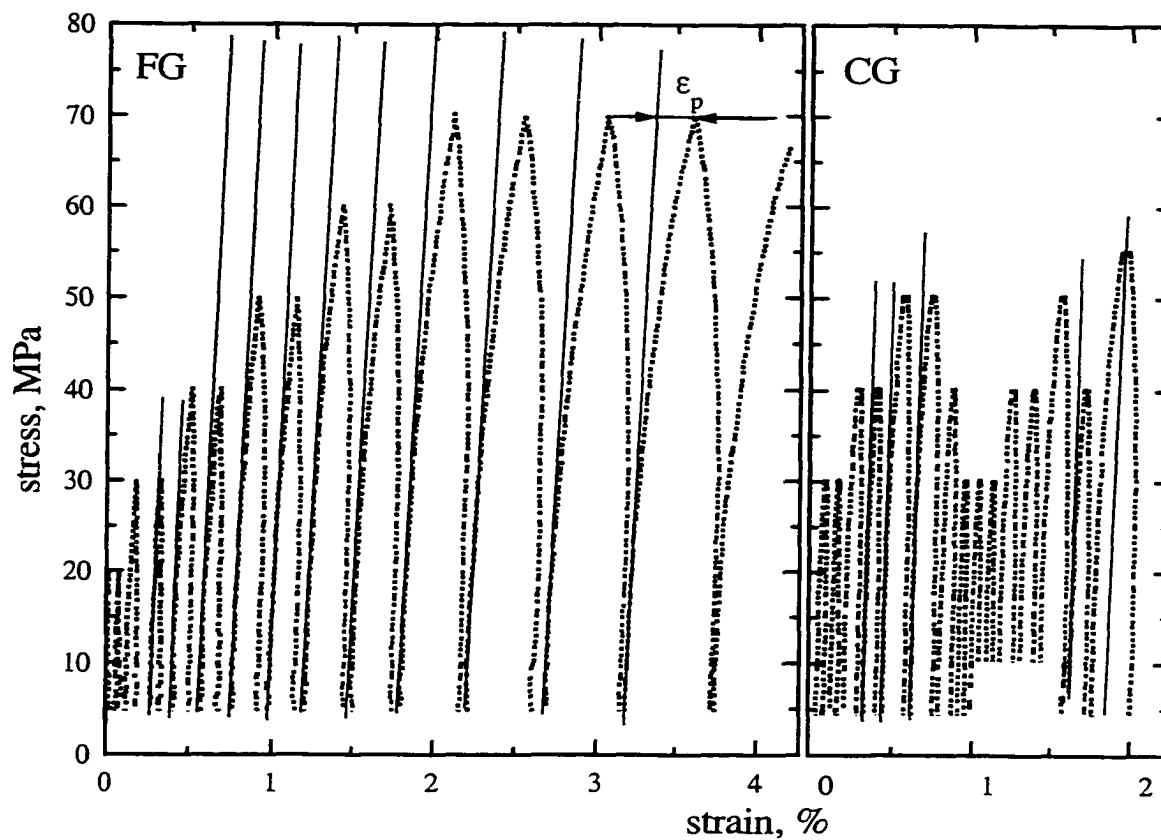
Fig. 59. Stress-strain curves obtained from cyclic loading-unloading tests for, (a) FG and (b) CG samples at 1200 °C and constant loading and unloading rates of 0.67 MPa/s. ε_p represents deviation from the linear elastic strain at the maximum cycle stress.
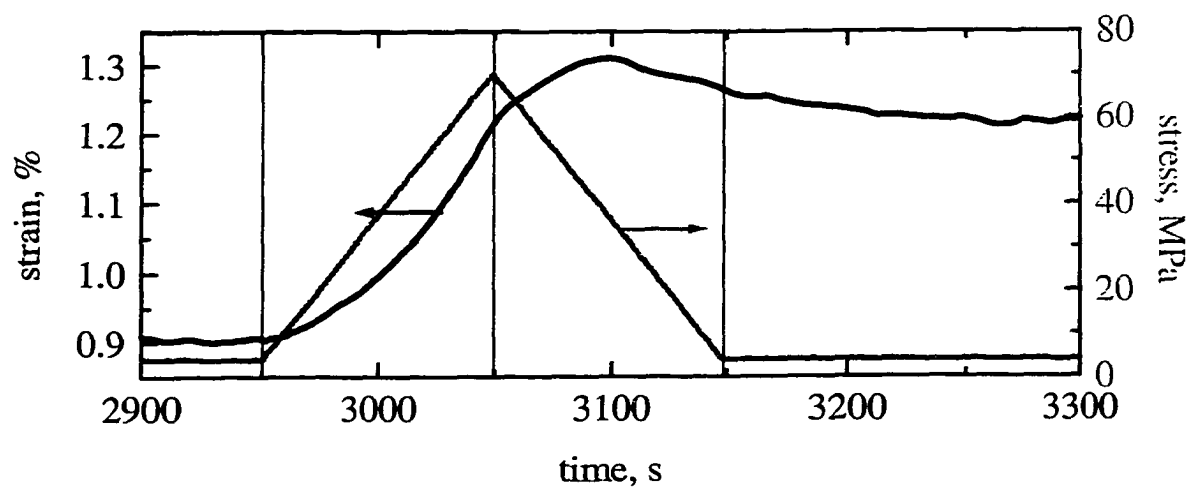
Fig. 60. Select stress (gray) and strain (black) changes with time during a typical loading-unloading test at 1200 °C (Fig. 59).
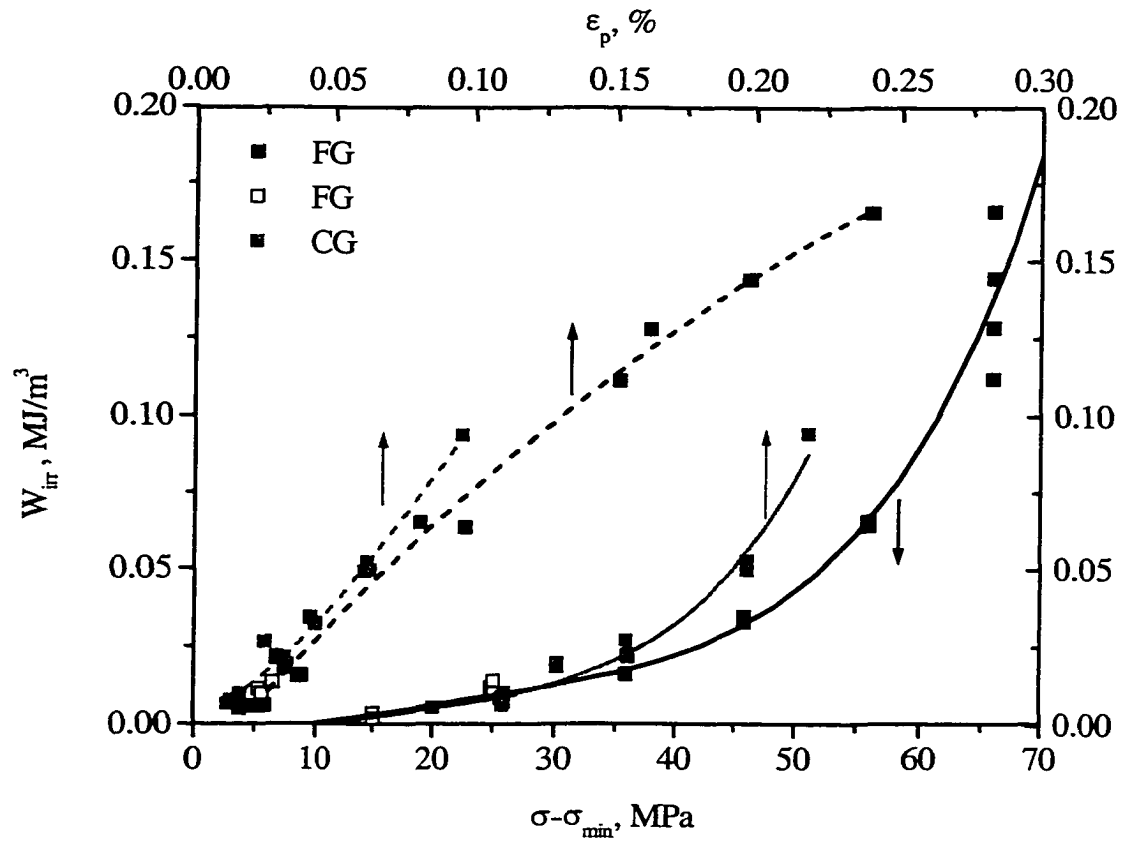
Fig. 61. Irreversible work at 1200 °C, W_{irr}, as a function of maximum cycle stress (solid lines), and ε_p (dashed lines, top axis) estimated from Fig. 59. Gary symbols - CG and black symbols - FG microstructure.
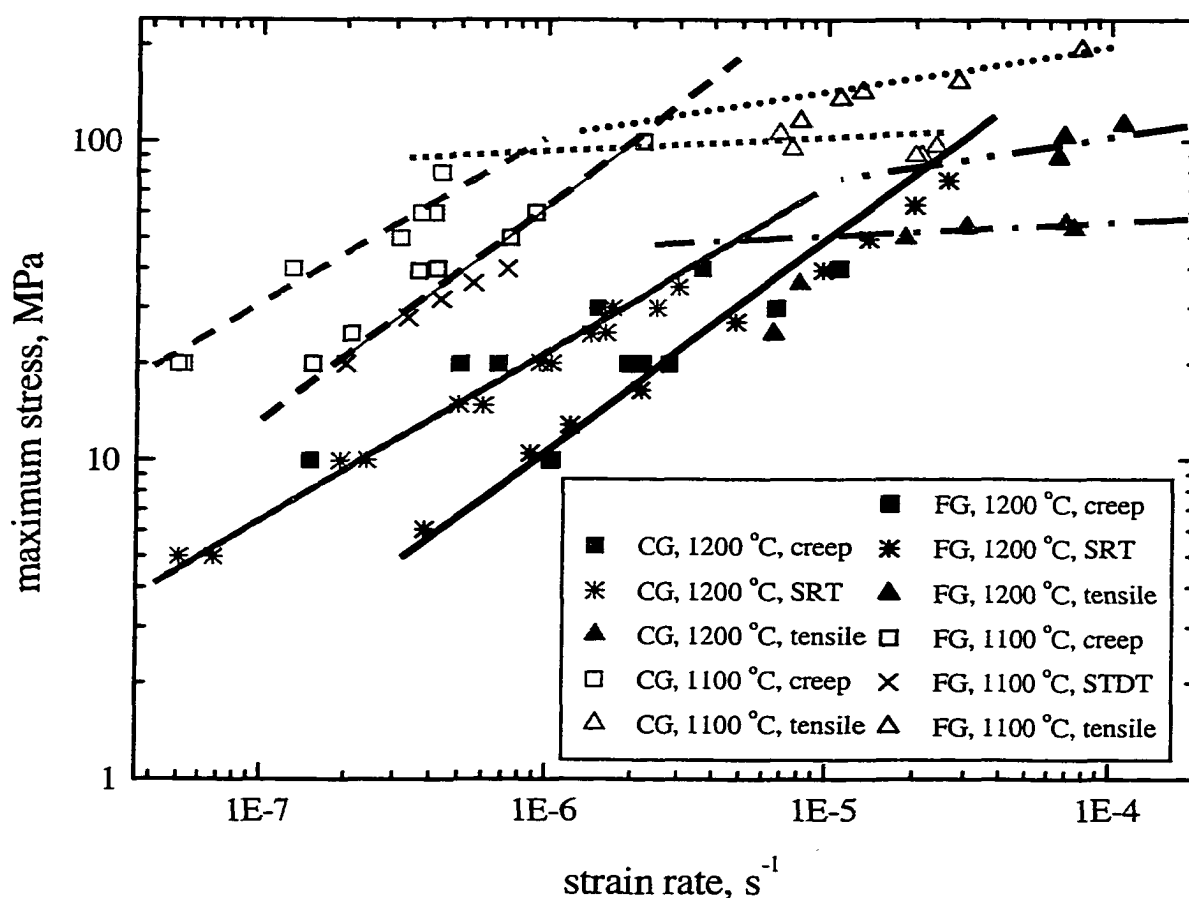
Fig. 62 Log-log plot of stress vs. strain rate. Results are obtained from tensile tests at constant CHD rate, stress relaxation tests, creep tests [2, 3] and strain transient dip tests [2, 3]. Plotted lines are only guides for the eyes. Gray symbols CG structure, black symbols FG structure. Open symbols represents results at 1100 °C, and closed symbols represent results at 1200 °C. Solid and dashed lines are related to the plastic deformation mode. Dotted and dotted-dashed lines are related to the brittle deformation mode.

Vita

MILADIN RADOVIC

DOB: 07/02/1966
Citizenship: Yugoslavia

Education

Ph.D. in Material Engineering, Drexel University, Philadelphia, PA, June 2001.
M.Sc. in Mechanical Engineering, major in Materials Engineering, Belgrade University, Yugoslavia, September 1997.
B.Sc. in Mechanical engineering, Belgrade University, Yugoslavia, July, 1992.

Experience

Research Assistant, Dept. of Materials Engineering Drexel University, Philadelphia, PA, September 1998- present.
Guest Researcher, National Institute of Standards and Technology, Gaithersburg, MD, December 1998-present.
Teaching Assistant, College of Mechanical Engineering, Belgrade University, September 1997-1998.
Research Assistant, College of Mechanical Engineering, Belgrade University, September 1992-1997.

Awards

- Drexel University Chapter of Sigma Xi, May 2000
- One year fellowship for young scientists awarded by the Ministry of Science and Technology of Republic of Serbia, 1993

Publications

Ten journal papers and twenty eight conference presentations.